

# PHASE CONTROL IN ELECTRICAL COUPLED OSCILLATOR: THEORY AND APPLICATIONS

A Dissertation

Presented to the Faculty of the Graduate School

of Cornell University

in Partial Fulfillment of the Requirements for the Degree of

Doctor of Philosophy

by

Vahnood Pourahmad

August 2018

© 2018 Vahnood Pourahmad  
ALL RIGHTS RESERVED

PHASE CONTROL IN ELECTRICAL COUPLED OSCILLATOR: THEORY  
AND APPLICATIONS

Vahnood Pourahmad, Ph.D.

Cornell University 2018

Controlling the relative phase shift of coupled oscillators becomes important in various applications. Examples include quadrature phase generation in image reject receivers, high data rate sampling circuits, clock distribution networks, novel associative memory paradigms and phased array systems for beam scanning.

In this work, we study the nonlinear dynamics of coupled oscillators from the perspective of both an applied mathematician who would prefer general and abstract models, and also that of an RF circuit designer who would appreciate comprehensive models that capture more subtle details of such systems. We then explain how the nonlinear phase dynamics of a ring of unidirectionally coupled oscillators may be used for mode switching and frequency tuning and present experimental verification of our analysis with a 65nm CMOS prototype chip. We also present a novel way of controlling relative phases of coupled oscillators by using the naturally occurring phases within oscillator cores to generate arbitrary phase shifts between them. Measurement results for a prototype chip fabricated in a standard 130nm CMOS technology verifies the theory and paves the way for employing it in the various applications mentioned before and in particular, beamforming at mm-wave frequencies. We also study the pattern recognition applications of coupled oscillator networks and propose a new alternative that avoids the impractical all to all coupling between the oscillators. The compact layout and simplicity of our proposed structure makes it readily implementable in any standard CMOS tech-

nology to realize a physical pattern classification system with ultra fast processing speed.

## **BIOGRAPHICAL SKETCH**

Vahnood Pourahmad was born in Tehran, Iran. He attended Sharif University of Technology from 2004 to 2008 where he received his B.Sc degree in Civil & Environmental Engineering. He then obtained two M.Sc degrees from Cornell University in the fields of Theoretical & Applied Mechanics and Electrical & Computer Engineering in 2012 and 2016 respectively and continued to get his PhD degree in Electrical & Computer Engineering in 2018.

To my beautiful family  
for their love and support

## ACKNOWLEDGEMENTS

There are many people whom I should thank here. First and foremost, I would like to thank my wonderful wife Mina, for being nothing but kind and supportive during my years as a PhD student. She brings hope, joy and happiness to the lives of everyone around her and I am certain that without her constant encouragement, I wouldn't have been able to finish this work.

Secondly, I would like to thank my PhD committee chair, Prof. Ehsan Afshari who not only has been my academic adviser, but also one of my best friends during all these years. So thank you Ehsan, for believing in me and for always being so supportive, professionally and otherwise.

I am also grateful to the members of my graduate committee, professors Alyosha Molnar and Steven Strogatz for their valuable technical advice during my graduate study years. I first got introduced to the wonderful world of nonlinear dynamics when I took the "Nonlinear Dynamics and Chaos" course offered by Steve at Cornell and I enjoyed every second of it and that is how I ended up writing my PhD thesis on the dynamics of electrical coupled oscillators.

I should also thank my former committee members, professors Timothy Healey, Brian Kirby and Amit Lal who served on my committee during my years as a graduate student in the field of Theoretical and Applied Mechanics (TAM). I took "Applied Mathematics II" with Tim while at Cornell and I think he is perhaps the best teacher I have ever had in my life. The level of clarity and rigor in his lectures never ceased to amaze me.

Next, I would like to thank my fellow group members. I should particularly thank Prof. Yahya Tousi for introducing me to the applications of nonlinear dynamics in high frequency circuit design. Much of what I did during my PhD years has been inspired by his ground breaking work in this area. I am also grateful to

Dr. Chen Jiang and Dr. Ali Mostajeran for being constant sources of technical help whenever I needed it. I should also thank Prof. Omeed Momeni, Prof. Ruonan Han, Dr. Mohammad Adnan, Dr. Wooram Lee, Dr. Guansheng Li and Dr. Hamidreza Aghasi for being such wonderful colleagues.

I had the privilege of getting to know many amazing individuals during my years at Cornell. Their exemplary kindness and friendship helped me feel at home even though I was a thousand miles away from home and at times was missing it dearly. Thank you Hadi Zadeh and Baran Alipanahi, Amir Sattarzadeh and Elham Bandehzadeh, Amirahmad Tarkeshdouz and Tina Sorbi, Mohammad and Leila Soltani, Abolhasan Vaezi and Mahya Mehrmohammadi, Mohammad Mahmoody, Hossein Hojjat, Hossein Jarrahi, Amirmasoud Ohadi, Sina Lashgari, Peyman Taherkhani, Sepehr Saroukhani, and Naser Nikandish for being such amazing friends.

Last but certainly not least, I should acknowledge my family for everything they have done for me. I thank my parents, Aliakbar and Monireh for their never ending, unconditional love and the many sacrifices they made in raising me. I thank my brothers, Vahraz and Vahbod for always being my role models. I owe much of my life long passion for mathematics, science and culture to them. I thank my relatives-in-law, Mohammadreza and Forough, Fatemeh, Shadi, Maryam and Mahdi for being such amazing people and for making my life more beautiful.

## TABLE OF CONTENTS

Biographical Sketch . . . . .	iii
Dedication . . . . .	iv
Acknowledgements . . . . .	v
Table of Contents . . . . .	vii
<b>1 Introduction</b>	<b>1</b>
1.1 Prelude . . . . .	2
1.2 Coupled Oscillator VCO's . . . . .	3
1.3 Coupled Oscillator Phased Arrays . . . . .	5
1.4 Associative Memory Properties of Coupled Oscillator Networks . . . . .	10
<b>2 Phase Reduced Model of General Oscillators: Kuramoto's Equation</b>	<b>14</b>
2.1 Introduction . . . . .	15
2.2 Definition of phase and the concept of isochron . . . . .	15
2.3 Phase-sensitivity function . . . . .	18
2.4 Properties of the phase function and its gradient . . . . .	18
2.5 Phase model of the externally perturbed oscillator . . . . .	20
2.6 Phase model of mutually coupled oscillators . . . . .	21
<b>3 Modelling Electrical LC Coupled Oscillators: Adler's Equation</b>	<b>25</b>
3.1 Introduction . . . . .	26
3.2 General model of coupled LC oscillators . . . . .	26
3.3 Injection locking and generalized Adler's equations . . . . .	31
3.4 Transconductive coupling and the quadrature oscillator . . . . .	36
3.5 General analysis of two identical, unidirectionally coupled oscillators	41
<b>4 Frequency Tuning with Coupled Oscillators</b>	<b>45</b>
4.1 Introduction . . . . .	46
4.2 Nonlinear dynamic model and analysis . . . . .	46
4.3 Mode switching and frequency tuning effects . . . . .	55
4.4 Experimental verifications . . . . .	58
<b>5 Arbitrary Phase Oscillator: A Generalization of Quadrature Oscillators</b>	<b>60</b>
5.1 Introduction . . . . .	61
5.2 Overview of the APO Structure . . . . .	62
5.2.1 System Level Description of the APO . . . . .	62
5.2.2 Intuition Behind APO Operation . . . . .	63
5.3 Circuit Design Considerations . . . . .	66
5.3.1 Preventing Dual Mode Oscillations . . . . .	66
5.3.2 Coupler Design . . . . .	68
5.4 Mathematical Model and Analysis . . . . .	70

5.4.1	APO Dynamic Model . . . . .	70
5.4.2	APO Dynamic Analysis . . . . .	77
5.4.3	APO Dynamic Analysis Verification . . . . .	80
5.5	Prototype Implementation . . . . .	81
<b>6</b>	<b>Associative Memory and Pattern Recognition in Coupled Oscillator Networks</b>	<b>86</b>
6.1	Introduction . . . . .	87
6.2	Associative memory properties of coupled oscillator networks . . . . .	88
6.2.1	Network training and the Hebbian learning rule . . . . .	89
6.3	An alternative to associative memory networks: The discriminant function approach . . . . .	91
6.4	Dynamics of symmetrically coupled oscillators . . . . .	94
6.4.1	The mathematical model . . . . .	94
6.4.2	Circuit implementation . . . . .	97
6.5	Pattern recognition with coupled oscillator chains . . . . .	100
6.5.1	System Description . . . . .	100
6.5.2	An example: Classification of alphabet letters . . . . .	102
6.5.3	Reducing chance of false/ambiguous classifications . . . . .	105
6.5.4	Storage capacity . . . . .	107
6.6	Appendix . . . . .	109
6.6.1	Analysis of the Kuramoto model for coupled oscillator chains	109
6.6.2	Determining input coupler Strengths from 2D input images .	111
6.6.3	Details of the training algorithm . . . . .	113
6.6.4	The MATLAB codes . . . . .	115
	<b>Bibliography</b>	<b>121</b>

CHAPTER 1  
INTRODUCTION

## 1.1 Prelude

Controlling the relative phase shift between electrical coupled oscillators becomes critical in a number of important applications. A classic example is the quadrature LC oscillator first introduced in [1] whereby two stand alone, cross-coupled oscillators are coupled anti-symmetrically to maintain a quadrature phase difference. This direct quadrature signal generation is now widely used in modern image rejection demodulators in wireless transceivers.

Coupled oscillator systems are also particularly useful for designing low noise, high output power signal sources. It is well known that coupling  $N$  oscillators ideally reduces their phase noise by a factor of  $1/N$  at the expense of burning  $N$  times more power and as such provide a reliable way of trading better phase noise performance with higher power consumption. [2] Furthermore, provided that frequency coherence and proper phase shifts are maintained between individual oscillators, their output signals could be constructively combined to realize output power levels beyond the reach of any single solid state source. This is why cost-effective, CMOS based coupled oscillator systems have the potential to beat compound semiconductor devices for signal generation at mm-wave and terahertz frequencies. [3, 4, 5, 6]

Among the many applications of coupled oscillator systems, we focus on three interesting areas in this work:

1. Coupled Oscillator VCO's
2. Coupled Oscillator Phased Arrays
3. Associative Memory Properties of Coupled Oscillator Networks

In what follows, we briefly describe each of these topics and explain their importance before presenting more detailed treatments in the bulk of this manuscript.

## 1.2 Coupled Oscillator VCO's

In conventional LC based, voltage control oscillators (VCO), varactors are incorporated inside the oscillator's tank to tune its resonance frequency and hence frequency of oscillation. While this approach works reasonably well at RF frequencies, it is usually not sufficient for designing high power VCO's that operate close to the cut-off frequency ( $f_{max}$ ), of the CMOS transistors. The poor quality factor of the varactors at such frequencies, enforces a severe trade off between the achievable output power and tuning range of CMOS oscillators operating above 100 GHz: Using varactors to tune the frequency brings additional loss in the resonator which consumes the scarce and precious power generated by the transistors, resulting in low output power and on the other hand, avoiding varactors results in having no control over the frequency of oscillation. This problem is further exacerbated for signal generation at terahertz frequencies ( $\approx 300$  GHz) since it is then necessary to employ some harmonic generation mechanism to reach such frequencies which further degrades the efficiency and output power of the oscillator.

As previously mentioned, using CMOS coupled oscillator systems is one of the most effective solutions to generate high output power at terahertz frequencies. The low cost, high scalability and ease of integration in CMOS technology makes it possible to combine output power from many coupled CMOS oscillators and reach power levels even beyond what compound semiconductor device with much higher  $f_{max}$  can generate. In order to efficiently combine and extract power from

a network of coupled oscillators, it is necessary to have control over the relative phase shifts between core oscillators. For example, to efficiently combine and extract third harmonic power from a simple ring of three coupled oscillators, it is best to enforce a phase shift of  $\pm 2\pi/3$  between the adjacent cores so that only multiples of the third harmonics would add constructively at a combining node in the center of the ring. The synchronous operation (same frequency and zero phase shift) of the ring is not optimal in this case because in addition to the third harmonics, the fundamental and second harmonic signals also add constructively at the center and therefore reduce the system's efficiency. Similar reasoning shows that for fourth harmonic generation in a ring of four coupled oscillators, a phase shift of  $\pm \pi/2$  is optimal rather than a zero phase shift. Interestingly, it turns out that in trying to control the phase shifts between coupled oscillators, one also gets the ability to control the common frequency to which the oscillators get locked in steady state. This allows for a novel frequency tuning mechanism that is specific to coupled oscillator systems and avoids using varactors inside the core resonators. [4, 5] Therefore the merits of using coupled oscillators for high power signal generation at high frequencies lies not only in the power combining effect that was expected from the beginning, but also in efficient extraction of the harmonic powers from the core oscillators because of the optimal phase shifts between the cores and also in generating more power in each oscillator without sacrificing their frequency tuning range. In Chapter 4, we study the nonlinear dynamics of unidirectionally coupled oscillator rings in detail and identify their steady state solutions and stability along with the corresponding frequency tuning effects. Measurement results for two terahertz, coupled oscillator sources fabricated in standard CMOS technology [4, 5] are then presented to verify the analysis.

### 1.3 Coupled Oscillator Phased Arrays

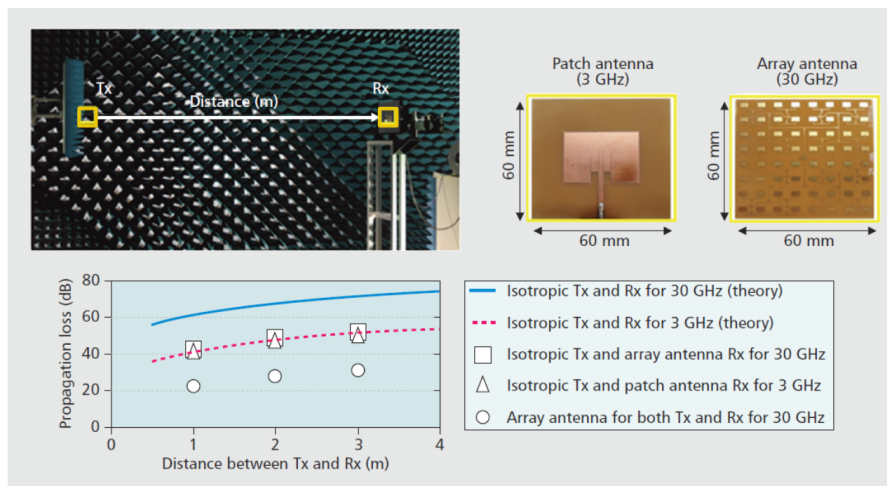
Another area of application which is becoming more important today is to use coupled oscillator arrays for beamforming in mm-wave (30 GHz - 300 GHz) frequencies. Millimeter wave communication has been widely accepted as the viable solution to accommodate the multi gigabit per second data rates required for 5G cellular systems. [7] It is clear that, as compared to the traditional RF systems, larger channel bandwidths could be allocated to each user which directly translates to higher data rates for mobile communications. Two frequency bands, 28 - 38 GHz and 70 - 100 GHz, are particularly promising because of the relatively low atmospheric attenuations at these bands. [8, 9] Historically mm-wave frequencies were ruled out for long range communications because of the concern for their higher propagation loss and their use had been limited to short range, indoor applications. More specifically, according to the Friis equation for wave propagation in free space, we have:

$$P_R = P_T \frac{G_T G_R c^2}{(4\pi r f)^2} \quad (1.1)$$

where  $P_R$  is the received power,  $P_T$  is the transmitted power,  $r$  is the distance between transmitter and receiver,  $f$  is the carrier frequency,  $c$  is speed of light and  $G_R$  and  $G_T$  are the receiver and transmitter antenna gains respectively. For ideal, isotropic transmitter and receiver, we have  $G_T = G_R = 1$  and clearly the received power is inversely proportional to the carrier frequency squared which suggests there would be around 20 dB reduction in the received power in going from RF frequencies ( $\approx 3$  GHz) to mm-wave frequencies ( $\approx 30$  GHz) for wireless communications. However it is certainly possible to realize higher than unity antenna gains on both the transmitter and receiver sides by employing highly directional phased arrays. The small wavelengths of mm-wave frequencies allow for integrating a

large number of antennas on a single chip to realize such beam forming techniques. Figure 1.1 shows an experimental verification of this observation whereby a patch antenna at 3 GHz is compared to a phased array antenna of the same physical size at 30 GHz. Interestingly, if the array antenna is used at both Tx and Rx sides, the measured propagation loss for the 30 GHz link would be 20 dB less than that of the 3 GHz link. [8] Extensive measurements in urban environments have also verified that once antenna arrays are employed for beamforming, path loss exponents similar to traditional cellular bands are observed for mid-range (200 m) transmission links in the millimeter wave band. [7, 8] Considering that today’s cell sizes for RF communications in urban environments are on the same order of 200 to 300 meters [7], this shows that cellular mm-wave communication is certainly feasible without adding much overhead in infrastructure.

As a key enabling technology, designing low cost, compact and scalable phased arrays would play a significant role in realizing mm-wave mobile communications. Conventional phased array architectures typically employ a “feed” network to distribute a high frequency signal generated by a central source to the radiation nodes



Copyright © 2014, IEEE

Figure 1.1: Measurement results for comparing propagation loss in free space at 3 and 30 GHz. Adopted with permission from [8].

of the array. Designated phase shifter blocks then add the necessary phase shifts to the incoming signal in order to steer the beam in desired directions. Figure 1.2 (a) shows a typical parallel feed architecture which uses a symmetric H-tree network for distributing the signal and separate phase shifters before each antenna element. It is clear that realizing such symmetric routing, without introducing unwanted mismatch and coupling between different signal paths, is a challenge for large arrays at mm-wave frequencies. Moreover, for large arrays, it becomes difficult to generate the required output power with good spectral purity from a single solid state source at mm-wave frequencies and this problem is further exacerbated by large losses in the feed network. Finally, designing wideband phase shifters with the full tuning range of  $360^\circ$  for every antenna element is challenging and significantly increases the overall cost and complexity of the system.

Figure 1.2 (b) shows a series feed architecture that alleviates the complexity of the distribution network as well as the number and phase tuning range required of the phase shifters. However, the series feed structure achieves this at the expense

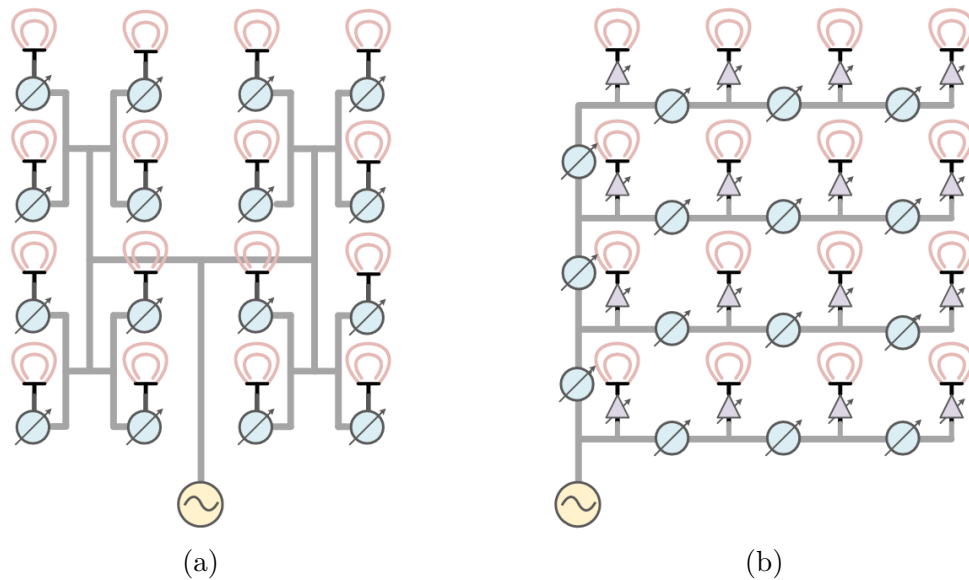


Figure 1.2: Conventional phased array structures:  
(a) Parallel feed (b) Series feed

of introducing asymmetric insertion loss and propagation delays in the received signal at the antennae. Therefore, it is necessary to add variable gain amplifiers (VGA) in a series feed architecture to compensate for the non-uniform insertion loss along each feeding line. The system also suffers from beam squint problem due to variation of phase shifts with frequency modulations.

The cost and complexity of phase shifters determines, to the large extent, the cost and complexity of the overall phased array system. In fact, it is not unusual for the cost of phase shifters to amount for roughly half the total cost of a typical phased array. [10] In order to eliminate the expensive phase shifter blocks, injection locked coupled oscillator arrays [11] have been proposed as an alternative to the more common feed based structures for beamforming. As shown in Figure 1.3(a), the basic principle behind this approach is to enforce the desired phase progressions by tuning the free running frequency of local oscillators relative to that of a reference injection source. According to Adler's equation [12, 13] for injection

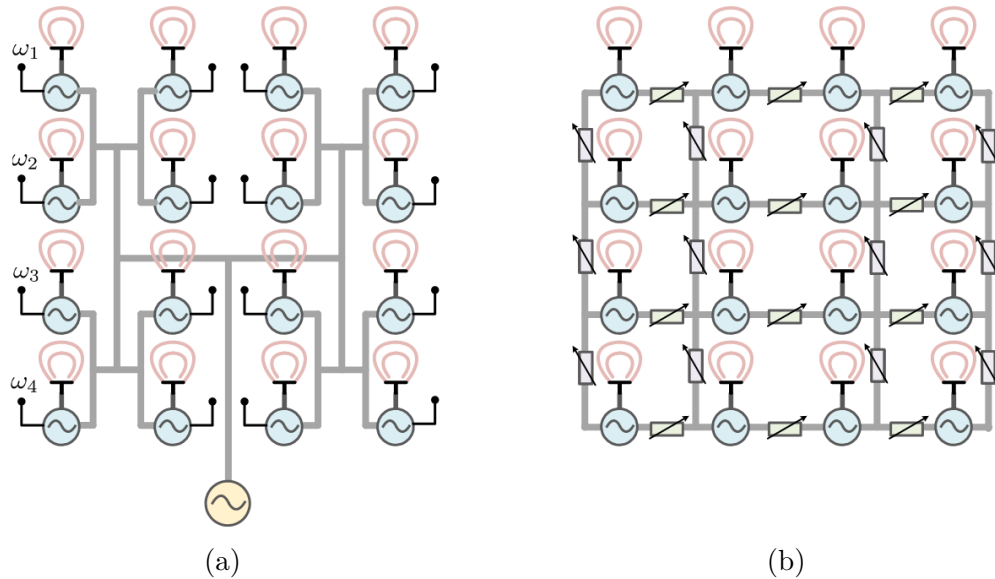


Figure 1.3: Alternative phased array structures: (a) Injection locked array (b) Coupled oscillator array

locking, we have:

$$\Delta\phi = \sin^{-1} \left( \frac{\omega_{inj} - \omega_i}{\Delta\omega_{max}} \right) \quad (1.2)$$

where  $\Delta\phi$  is the phase difference between the local oscillator and the injection signal,  $\omega_i$  is the free running frequency of the  $i^{th}$  local oscillator, and  $\Delta\omega_{max}$  is the frequency locking range. Therefore, desired phase shifts can be set by appropriately tuning the value of  $\omega_i$  for each oscillator with respect to  $\omega_{inj}$ . However, it is clear that this approach suffers from an undesired inter-dependence between frequency and direction of the radiated beam. Furthermore,  $\Delta\omega_{max}$  is inversely proportional to the quality factor ( $Q$ ) of the oscillators and as such, there is a direct trade off between the bandwidth and phase noise performance of these systems.

Coupled oscillator phased arrays [6], offer an attractive alternative to the architectures described above. As shown in Figure 1.3(b), in these structures, each antenna is derived by a designated local oscillator and hence the complex and lossy feed networks are eliminated. Frequency locking as well as desired phase shift patterns between the nodes are maintained through tunable coupling channels between adjacent oscillators and the symmetric, bidirectional coupling between oscillators would guarantee on-resonance operation of the core oscillators for best phase noise performance. The coupled oscillator array obviates the need for explicit phase shifter elements, achieves output power and phase noise levels beyond the reach of any single, solid state mm-wave source and is readily scalable to larger arrays.

To fully exploit the benefits of using coupled oscillator arrays for beamforming, it is necessary to design coupler blocks that are simple and do not incorporate any explicit phase shifters and yet are able to enforce arbitrary phase shifts between the coupled oscillators. In this work, we present a novel coupled oscillator system that makes this a reality. In what we call an ‘‘Arbitrary Phase Oscillator’’ or APO

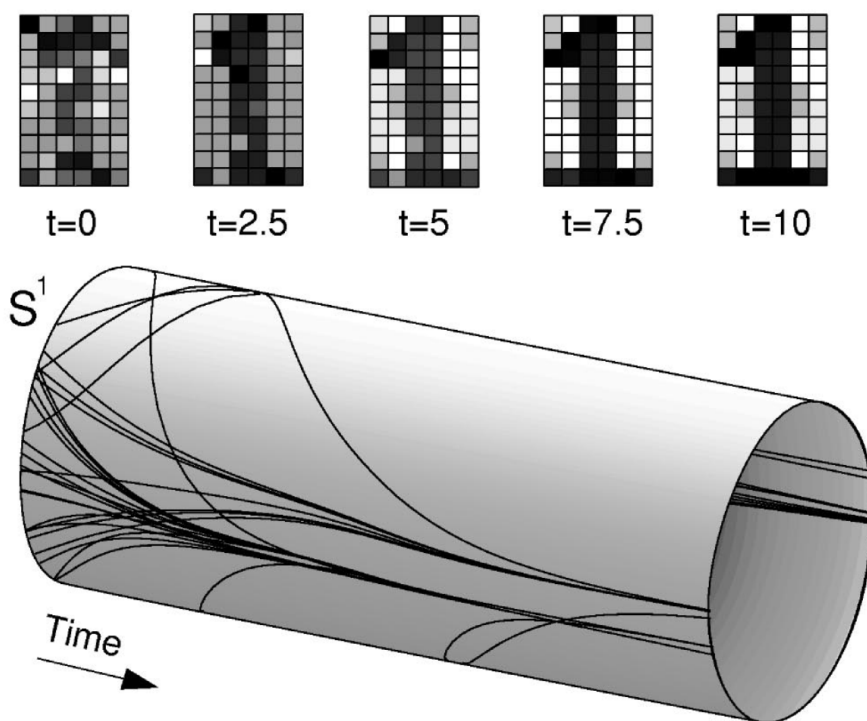
for short, the naturally occurring phase shifts between different stages of LC ring oscillators are employed to construct any desired phase from  $0^\circ$  to  $360^\circ$  between oscillators through analog control voltages that control the relative strengths of different coupling channels.

## 1.4 Associative Memory Properties of Coupled Oscillator Networks

There is mounting evidence that synchronized rhythms in firing rates of neurons plays a fundamental role in information processing in the brain. [14, 15, 16, 17] These experimental observations in the field of neuroscience have resulted in a rise of interest in using networks of coupled oscillators to implement neuromorphic computation paradigms. [18, 19, 20, 21, 22, 23, 24] The interest in neuromorphic computing is understandably due to the realization that, even though conventional computers are much better than the human brain in executing precise, sequential algorithms to do calculations at unimaginable speeds, they are surprisingly weak at doing holistic pattern recognition or classification tasks that are natural to human intelligence.

In the neuromorphic coupled oscillator systems proposed so far [18, 19, 20, 21, 22], information is typically encoded in the relative phase shifts that exist between coupled oscillators in steady state. It has been shown that coupled oscillator systems have regenerative associative memory capabilities similar to Hopfield [25] networks and as such could be used for detection and recreation of stored patterns in input data that has been subject to noise and distortion. The idea is that by modifying the underlying coupling parameters, it is possible to make predefined

phase shift patterns correspond to stable, steady state solutions of a coupled oscillator network such that if the system is initially released from close proximity of one of the stored patterns, it automatically converges to that particular stored pattern in steady state. (See Figure 1.4) In Chapter 6, we study the nonlinear dynamics of bidirectionally coupled oscillator networks and show how such networks could be trained, by properly tuning the coupling characteristics, to store a number of predefined patterns as their steady states. As explained in Chapter 6, the existing training methods for the coupled oscillator networks suffer from two important drawbacks. The first problem is concerned with the physical implementation of these networks which requires adaptive connections between each pair of oscillators. This practically limits the size and complexity of the arrays that can be



Copyright © 1999, APS

Figure 1.4: Regeneration of a stored pattern from its distorted image in a network of coupled oscillators. Reprinted with permission from [18].

realized. The second problem is more fundamental and happens even for the ideal, fully connected networks. In trying to store the desired set of predefined patterns in a coupled oscillator network, a number of spurious patterns also become stable steady state solutions of the system. The number of spurious patterns grow increasingly fast with the number of desired patterns and prevents the system from correct regeneration of the stored patterns.

In order to avoid the aforementioned problems in using fully connected coupled oscillator networks for pattern recognition, we propose an alternative paradigm [24] in which a simple coupled oscillator array with only local coupling can be trained to act as a “discriminant” engine and classify patterns into separate groups. In our proposed paradigm, chance of false classification is minimized by running multiple tests on an input data set and therefore it does not suffer from the debilitating spurious pattern storage problem of Hopfield networks. The simplicity of the coupling structure between the core oscillators and the compact layout of the ring oscillators makes our design readily scalable and easy to implement on any standard CMOS technology.

The rest of this dissertation is organized as follows: In Chapter 2, we review the “phase reduction” method as the most general and abstract formulation of coupled oscillator problems and show how the celebrated Kuramoto model [26] can be used to study the nonlinear dynamics of coupled oscillator systems. In Chapter 3, we look at the more particular case of injection locking in resonator based, electrical oscillator, derive a generalized form of Adler’s equation [12, 27] which captures the dynamics of both amplitude and phase of such oscillators and also study the dynamics of quadrature LC oscillators. In Chapter 4, we study the frequency tuning effects in a unidirectionally coupled ring of oscillators and in

Chapter 5 we present a novel mechanism for generation of arbitrary phase shifts between coupled oscillators which can be readily used in making scalable coupled oscillator phased arrays at RF and mm-wave frequencies. Finally, in Chapter 6 we study networks of coupled oscillators for using in associative memory and pattern recognition applications.

CHAPTER 2  
PHASE REDUCED MODEL OF GENERAL OSCILLATORS:  
KURAMOTO'S EQUATION

## 2.1 Introduction

In this chapter, we review a powerful and general mathematical framework for studying weakly coupled oscillators. The generality and strength of this method stems from the fact that it does not make any particular assumption on the physical mechanism of oscillations and as such can be applied to study coupled oscillators in a wide range of practical applications from Biology and Neuroscience to Mechanical and Electrical Engineering.

Arguably, the most abstract and general mathematical framework that has been developed for studying the dynamics of coupled oscillators is the “**phase reduced**” model of Kuramoto and Malkin. [28, 29] In this approach, instead of trying to solve complicated, multidimensional differential equations to get accurate oscillator waveforms, the dynamics of each oscillator is captured by a single **phase** variable and the focus is efficiently placed on finding the relative phase shifts between individual oscillators. A beautiful and mathematically rigorous treatment of this subject can be found in excellent books written by leading scientists in the field of mathematical neuroscience. [28, 29] Our objective here is to only give a brief and self-contained review of the subject so that the interested reader could get started on tackling general coupled oscillator problems similar to the ones studied in the subsequent chapters of this work.

## 2.2 Definition of phase and the concept of isochron

Presence of oscillation in a dynamical system :

$$\dot{\mathbf{x}} = \mathbf{f}(\mathbf{x}) \quad \mathbf{x} \in \mathbb{R}^m \quad (2.1)$$

corresponds to existence of a *stable limit cycle*,  $\Gamma$ , in the phase plane. Moreover  $\Gamma$  has its *basin of attraction*,  $\Omega_\Gamma$ , which is the set of all the points  $\mathbf{y}_0$  in the phase plane that get attracted to  $\Gamma$  by the dynamic flow :

$$\Omega_\Gamma = \{\mathbf{y}_0 \in \mathbb{R}^m \mid \mathbf{y}(0) = \mathbf{y}_0 \Rightarrow \mathbf{y}(t) \rightarrow \Gamma \text{ as } t \rightarrow \infty\}$$

The procedure to rigorously define phase variable for oscillators consists of two steps:

1. The phase variable is first defined for all points on  $\Gamma$
2. The definition is then extended to all points lying within  $\Omega_\Gamma$

In order to define phase variable on the limit cycle, one starts with an arbitrary parametrization of  $\Gamma$ . This gives a periodic function of time,  $\hat{\mathbf{x}}(t)$ , whose period is equal to the period of oscillation,  $T$  and arbitrarily satisfies  $\hat{\mathbf{x}}(0) = \mathbf{x}_0$  for some  $\mathbf{x}_0 \in \Gamma$ . Starting from the reference point  $\mathbf{x}_0$  on the limit cycle, the phase variable on this point is defined to be zero so that  $\vartheta(\mathbf{x}_0) = 0$ . For any other point,  $\mathbf{x} \in \Gamma$ , it is necessarily true that:

$$\exists \tau \quad , \quad 0 < \tau < T \quad : \quad \hat{\mathbf{x}}(\tau) = \mathbf{x}$$

The phase of this point is then simply defined as:

$$\vartheta(\mathbf{x}) := \frac{2\pi}{T}\tau = \omega_0\tau$$

where  $\omega_0$  is the free-running frequency of the oscillator.

In order to extend the definition of phase variable to all points in the oscillator's basin of attraction, consider a trajectory,  $\mathbf{y}(t)$ , in the phase plane starting from point  $\mathbf{y}_0 \in \Omega_\Gamma$ . Since  $\mathbf{y}_0$  lies inside the basin of attraction of  $\Gamma$ , it will be attracted

to the limit cycle and in fact it is possible to find a dual trajectory,  $\tilde{\mathbf{x}}(t)$ , starting from some point,  $\tilde{\mathbf{x}}_0$ , on the limit cycle that ultimately converges to  $\mathbf{y}(t)$ :

$$\tilde{\mathbf{x}}(t) \rightarrow \mathbf{y}(t) \quad \text{as } t \rightarrow +\infty$$

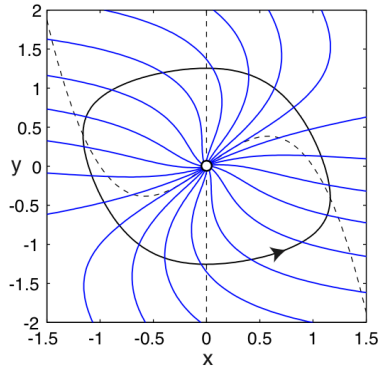
$$\tilde{\mathbf{x}}(0) = \tilde{\mathbf{x}}_0 \in \Gamma$$

$$\mathbf{y}(0) = \mathbf{y}_0 \in \Omega_\Gamma$$

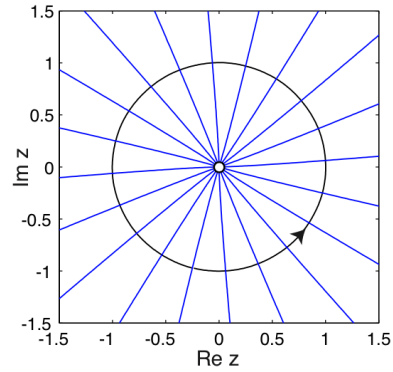
The phase variable for point  $\mathbf{y}_0$  is now defined to be the same as that of  $\tilde{\mathbf{x}}_0$ :

$$\vartheta(\mathbf{y}_0) := \vartheta(\tilde{\mathbf{x}}_0)$$

Moreover, the set of all points in  $\Omega_\Gamma$  whose phases are identical to that of point  $\tilde{\mathbf{x}}_0$ , is called the **isochron** of  $\tilde{\mathbf{x}}_0$ .



Van der pol Oscillator :  
 $\dot{x} = y$  ,  $\dot{y} = -x + (1 - x^2)y$



Andronov-Hopf Oscillator :  
 $\dot{z} = (1 + i)z - z|z|^2$

Figure 2.1: Isochrons of Van der Pol and Andronov-Hopf oscillators. Reprinted with permission from [28].

## 2.3 Phase-sensitivity function

The general definition of phase and the concept of isochrons provide a powerful tool for visualizing the effect of external perturbations on the phase of oscillators. For example, a quick examination of Figure 2.1, reveals that depending on its strength and direction in the phase plane, an external perturbation can move the oscillator from one isochron to another and hence change its phase. This also shows that the oscillator phase is particularly vulnerable to external stimulations or noise wherever the isochrons are closer together. This is reminiscent of the relationship between electric equipotential surfaces and electric fields where electric fields are stronger where the equipotential curves are closer together. This analogy also motivates defining the “**phase-sensitivity**” function,  $\mathbf{Z}(\theta)$ , as the gradient of the phase function evaluated at the point on the limit cycle with phase of  $\theta$ :

$$\mathbf{Z}(\theta) := \nabla \vartheta(\mathbf{x}) \quad \text{where } \mathbf{x} \in \Gamma, \vartheta(\mathbf{x}) = \theta \quad (2.2)$$

where for future reference, we note that if  $\vartheta(\mathbf{x}) = \theta$  for  $\mathbf{x} \in \Gamma$ , then we necessarily have  $\mathbf{x} = \hat{\mathbf{x}}(\omega_0^{-1}\theta)$ . Figure 2.2 shows the phase sensitivity function for two important oscillatory dynamic systems. It is also worth mentioning that a similar concept has been previously introduced to the RF circuit design literature under the name of “impulse sensitivity function”, or **ISF** for short, to model **phase noise** of electrical oscillators. [30]

## 2.4 Properties of the phase function and its gradient

For an oscillator with an *exponentially* stable limit cycle, the phase function has two important properties, which we state here without proof: [28]

- Continuity : The function  $\vartheta(\mathbf{x})$  is continuous
- Invariance :  $\vartheta(\mathbf{x}(0)) = \vartheta(\mathbf{y}(0)) \Rightarrow \vartheta(\mathbf{x}(t)) = \vartheta(\mathbf{y}(t)) \quad \forall t > 0$

By using the above properties, an important identity for the phase sensitivity function can be deduced for such dynamic systems. This result is of great importance in the derivation of the final phase-reduced equations for weakly coupled oscillators.

Consider an arbitrary trajectory  $\mathbf{y}(t)$  contained in  $\Omega_{\mathbf{r}}$  and its dual trajectory  $\tilde{\mathbf{x}}(t)$  on the limit cycle. Let us assume that  $\vartheta(\mathbf{y}(0)) = \theta_0$  and use uniqueness property of the dynamic system described by (2.1), to conclude that  $\tilde{\mathbf{x}}(t)$  should simply be:

$$\tilde{\mathbf{x}}(t) = \hat{\mathbf{x}}(\tau + t) \quad \text{where} \quad \tau = \omega_0^{-1}\theta_0$$

On the other hand, by the invariance property of the phase function we have:

$$\vartheta(\mathbf{y}(t)) = \vartheta(\tilde{\mathbf{x}}(t)) = \omega_0(t + \tau)$$

Upon differentiating the last identity we get:

$$\frac{d}{dt}\vartheta(\mathbf{y}) = \nabla\vartheta(\mathbf{y}) \cdot \frac{d\mathbf{y}}{dt} = \omega_0$$

(2.1)  
 $\Rightarrow$

$$\nabla\vartheta(\mathbf{y}) \cdot \mathbf{f}(\mathbf{y}) = \omega_0$$

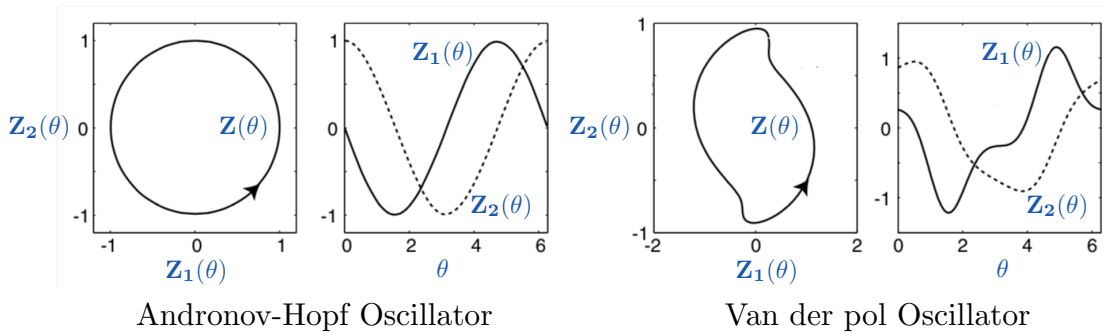


Figure 2.2: Phase-sensitivity function for two famous oscillators. Reprinted with permission from [28].

The above result obviously holds for any point on the limit cycle or within the basin of attraction and therefore in general we have :

$$\nabla\vartheta(\mathbf{x}) \cdot \mathbf{f}(\mathbf{x}) = \omega_0 \quad \forall \mathbf{x} \in \Gamma \cup \Omega_\Gamma \quad (2.3)$$

## 2.5 Phase model of the externally perturbed oscillator

Before dealing with coupled oscillator systems, it is better to study the behavior of a single oscillator which is under weak external excitations. Mathematically, this system can be described as :

$$\dot{\mathbf{x}} = \mathbf{f}(\mathbf{x}) + \epsilon \mathbf{p}(t) \quad (\epsilon \ll 1) \quad (2.4)$$

where  $\mathbf{p}(t)$  represents the external perturbation and  $\epsilon$  shows the overall strength of the perturbing signal which is assumed to be *weak* as suggested by the  $\epsilon \ll 1$  condition. Differentiating the phase variable with respect to time gives :

$$\frac{d}{dt}\vartheta(\mathbf{x}) = \nabla\vartheta(\mathbf{x}) \cdot \left( \mathbf{f}(\mathbf{x}) + \epsilon \mathbf{p}(t) \right)$$

which upon using (2.3) simplifies to :

$$\frac{d}{dt}\vartheta(\mathbf{x}) = \omega_0 + \epsilon \nabla\vartheta(\mathbf{x}) \cdot \mathbf{p}(t) \quad (2.5)$$

So far there has been no approximation in our derivations and equation (2.5) is exact. However in its current form, equation (2.5) is not particularly useful because the  $\mathbf{x}(t)$  term still remains on the right hand side. It is here, in getting to a *phase reduced* model of the system which gives an ordinary differential equation in terms of  $\vartheta(\mathbf{x})$ , that the assumption of weak coupling is crucial. This important simplification happens because under weak external disturbance, the solution to (2.4) remains in close proximity of the limit cycle for the unperturbed system and

so the phase function and its gradient can be approximated by their corresponding values on  $\Gamma$ .

More formally, define a new variable  $\theta(t) = \vartheta(\mathbf{x}(t))$ . Since the perturbation is weak and the system remains in close proximity of the original limit cycle, we may use the approximation:

$$\mathbf{x}(t) \approx \hat{\mathbf{x}}(\omega_0^{-1}\theta)$$

We may now use this approximation in equation (2.5) and get :

$$\begin{aligned} \dot{\theta} &= \omega_0 + \epsilon \nabla \vartheta(\mathbf{x}(t)) \cdot \mathbf{p}(t) \\ &\stackrel{\epsilon \ll 1}{\approx} \\ \dot{\theta} &\approx \omega_0 + \epsilon \nabla \vartheta(\hat{\mathbf{x}}(\omega_0^{-1}\theta)) \cdot \mathbf{p}(t) \\ &\stackrel{(2.2)}{\approx} \\ \dot{\theta} &\approx \omega_0 + \epsilon \mathbf{Z}(\theta) \cdot \mathbf{p}(t) \end{aligned}$$

The differential equation that governs the evolution of an oscillator's phase under weak external perturbations is therefore :

$$\dot{\theta} = \omega_0 + \epsilon \mathbf{Z}(\theta) \cdot \mathbf{p}(t) \tag{2.6}$$

This is an extremely useful result as it has transformed a multidimensional differential equation into a single ODE in terms of the phase variable.

## 2.6 Phase model of mutually coupled oscillators

In this section, we get to our main objective which is to have a phase model for analyzing networks of identical, weakly coupled oscillators. A network of  $n$  coupled

oscillators is a dynamical system in the form of :

$$\dot{\mathbf{x}}_i = \mathbf{f}(\mathbf{x}_i) + \epsilon \sum_{j=1}^n \mathbf{g}_{ij}(\mathbf{x}_i, \mathbf{x}_j) \quad (\mathbf{x}_i \in \mathbb{R}^m) \quad (2.7)$$

where the  $\mathbf{g}_{ij}(\mathbf{x}_i, \mathbf{x}_j)$  term shows the coupling effect of the  $j^{\text{th}}$  oscillator on the  $i^{\text{th}}$  one. In the above equation,  $\sum_{j=1}^n \mathbf{g}_{ij}(\mathbf{x}_i, \mathbf{x}_j)$ , can be replaced by  $\mathbf{p}_i(t)$  so as to get to the form studied in the last section. Therefore the phase model of the whole system can be described as :

$$\dot{\theta}_i = \omega_0 + \epsilon \mathbf{Z}(\theta_i) \cdot \sum_{j=1}^n \mathbf{g}_{ij}(\hat{\mathbf{x}}(\omega_0^{-1}\theta_i), \hat{\mathbf{x}}(\omega_0^{-1}\theta_j)) \quad \forall i \in \{1 \dots n\}$$

where the weak coupling assumption has been used to replace  $\mathbf{x}_i$  and  $\mathbf{x}_j$  in the argument of the  $\mathbf{g}_{ij}$  function with  $\hat{\mathbf{x}}(\omega_0^{-1}\theta_i)$  and  $\hat{\mathbf{x}}(\omega_0^{-1}\theta_j)$  respectively. If we introduce a simple change of variable  $\theta_i = \omega_0 t + \varphi_i$ , we get:

$$\dot{\varphi}_i = \epsilon \mathbf{Z}(\omega_0 t + \varphi_i) \cdot \sum_{j=1}^n \mathbf{g}_{ij}(\hat{\mathbf{x}}(t + \omega_0^{-1}\varphi_i), \hat{\mathbf{x}}(t + \omega_0^{-1}\varphi_j)) \quad (2.8)$$

We now use the weak coupling assumption once again to make the above equation even simpler. In what follows, we employ the classical “**method of averaging**” which is typically used to transform non-autonomous dynamical systems into simpler, autonomous systems.

Discarding the delicate formalities which the interested reader can find in [31], the averaging theorem essentially states that if we have a dynamic system described by:

$$\dot{\mathbf{x}} = \epsilon \mathbf{f}(\mathbf{x}, t) \quad 0 \leq \epsilon \ll 1 \quad (2.9)$$

where  $f$  is periodic in  $t$  with a period of  $T$ , then there is an associated, *autonomous averaged system* given by:

$$\begin{aligned} \dot{\mathbf{y}} &= \epsilon \tilde{\mathbf{f}}(\mathbf{y}) \\ \tilde{\mathbf{f}}(\mathbf{y}) &:= \frac{1}{T} \int_0^T \mathbf{f}(\mathbf{y}, t) dt \end{aligned} \quad (2.10)$$

such that if  $\mathbf{x}(t)$  and  $\mathbf{y}(t)$  are the solutions to the systems described by (2.9) and (2.10) respectively with  $|\mathbf{x}(0) - \mathbf{y}(0)| = \mathcal{O}(\epsilon)$ , then  $|\mathbf{x}(t) - \mathbf{y}(t)| = \mathcal{O}(\epsilon)$  for time scales of  $t \sim 1/\epsilon$ . Moreover if  $\mathbf{y}_0$  is a stable fixed point of the averaged system (2.10), then the original system described by (2.9) has a stable periodic orbit in  $\mathcal{O}(\epsilon)$  proximity of  $\mathbf{y}_0$ .

Next, notice that equation (2.8) has the same form of  $\dot{\mathbf{x}} = \epsilon \mathbf{f}(\mathbf{x}, t)$  with  $\mathbf{f}$  being periodic in  $t$  with a period of  $T$ . The averaged form of (2.8) gives:

$$\dot{\varphi}_i = \sum_{j=1}^n \frac{\epsilon}{T} \underbrace{\int_0^T \mathbf{Z}(\omega_0 t + \varphi_i) \cdot \mathbf{g}_{ij} \left( \hat{\mathbf{x}} \left( \frac{\omega_0 t + \varphi_i}{\omega_0} \right), \hat{\mathbf{x}} \left( \frac{\omega_0 t + \varphi_j}{\omega_0} \right) \right) dt}_{F_{ij}}$$

By introducing the change of variable formula  $\eta = \omega_0 t + \varphi_i$ , we can rewrite the above integrations as:

$$\begin{aligned} F_{ij} &= \frac{\epsilon}{2\pi} \int_{\varphi_i}^{\varphi_i+2\pi} \mathbf{Z}(\eta) \cdot \mathbf{g}_{ij} \left( \hat{\mathbf{x}} \left( \frac{\eta}{\omega_0} \right), \hat{\mathbf{x}} \left( \frac{\eta + \varphi_j - \varphi_i}{\omega_0} \right) \right) d\eta \\ &\Rightarrow \\ F_{ij} &= \frac{\epsilon}{2\pi} \int_0^{2\pi} \mathbf{Z}(\eta) \cdot \mathbf{g}_{ij} \left( \hat{\mathbf{x}} \left( \frac{\eta}{\omega_0} \right), \hat{\mathbf{x}} \left( \frac{\eta + \varphi_j - \varphi_i}{\omega_0} \right) \right) d\eta \end{aligned}$$

In order to make the final form of our equations more elegant, let us define:

$$H_{ij}(\chi) := \frac{\epsilon}{2\pi} \int_0^{2\pi} \mathbf{Z}(\eta) \cdot \mathbf{g}_{ij} \left( \hat{\mathbf{x}} \left( \frac{\eta}{\omega_0} \right), \hat{\mathbf{x}} \left( \frac{\eta + \chi}{\omega_0} \right) \right) d\eta \quad (2.11)$$

so that we can write:

$$\begin{aligned} \dot{\varphi}_i &= \sum_{j=1}^n H_{ij}(\varphi_j - \varphi_i) \quad \Rightarrow \\ \dot{\theta}_i &= \omega_0 + \sum_{j=1}^n H_{ij}(\theta_j - \theta_i) \end{aligned} \quad (2.12)$$

Finally, notice that by definition,  $H_{ij}(\chi)$  is a periodic function with a period of  $2\pi$  and as such could be represented by its Fourier series expansion. In particular,

if we can assume that only the first harmonic terms of the Fourier expansion of  $H_{ij}(\chi)$  are significant, we can write:

$$\dot{\theta}_i = \omega_0 + \sum_{j=1}^n k_{ij} \sin(\theta_j - \theta_i + \psi_{ij}) \quad (2.13)$$

Equation (2.13) is the celebrated **Kuramoto** model of coupled oscillators in which  $k_{ij}$  and  $\psi_{ij}$  can be interpreted as the effective strength and inherent phase shift of the coupling from the  $j^{\text{th}}$  to the  $i^{\text{th}}$  oscillator.

As mentioned in the beginning of this chapter, the phase reduced model of coupled oscillators is very general and can be used to study almost any coupled oscillator problem provided that weak coupling assumption is valid for one's modeling purposes. What needs to be done in each problem is to determine the relevant coupling parameters, i.e.,  $k_{ij}$  and  $\psi_{ij}$  in the Kuramoto model (2.13) or more generally the  $H_{ij}$  functions in (2.12), through evaluating the integral equation in (2.11). This in turn requires determining the phase sensitivity function,  $Z(\theta)$ , which in certain cases (e.g. Andronov Hopf oscillator) can be derived analytically or more practically, will be determined by numerical simulations or even experimental measurements. In the next chapter, we study electrical LC oscillators and present an alternative method of determining the coupling parameters from first principles of circuit theory.

CHAPTER 3  
MODELLING ELECTRICAL LC COUPLED OSCILLATORS:  
ADLER'S EQUATION

### 3.1 Introduction

In the previous chapter, we introduced the general *phase-reduced* model of coupled oscillators which culminated in the derivation of the celebrated Kuramoto equation. While being quite elegant and powerful, the phase reduced model has a couple of slight drawbacks. Firstly, precise determination of the coupling parameters in terms of the physical variables of the system is a rather complicated process which requires finding the phase sensitivity function of the oscillator and evaluating some averaging integrals. Secondly, as its name suggests, the phase reduction technique reduces the original problem to the analysis of oscillator's phase variables without capturing the dynamics of their amplitudes. In this chapter, we present an alternative approach for the particular case of electrical LC oscillators. Starting from the first principles of circuit theory, we derive a similar equation for the dynamics of oscillator phase variables in terms of the familiar circuit parameters and also get a differential equation for the dynamics of the oscillator amplitudes. This approach should look more familiar and easy to follow for our respected reader who is well versed in analog circuit design and he/she probably recognizes the final result as a generalized form of the well known **Adler's equation**. Our work here should be compared to a previous work in [27] which derived similar results through a slightly different approach.

### 3.2 General model of coupled LC oscillators

Adler's classic analysis of injection locking [12] is well known in RF circuit design. Strictly speaking, Adler's analysis applies only to unidirectional injection locking where an LC oscillator gets locked to an external source without having any effect

on the source in return. However, Adler’s model can be slightly modified to capture the dynamics of mutually coupled oscillators as well. It is our aim here to generalize Adler’s analysis and propose a new systematic approach that can be confidently applied to study arbitrary coupled LC oscillators. Our approach is based on using classical “averaging methods” for analysis of nonlinear dynamic systems [31, 32] and should be compared with the previous work in [27, 33] which uses a different approach to get similar results. In what follows, instead of using the mathematical formalism behind averaging techniques, which the mathematically inclined reader may find in [31, 32], we try to give a more physically intuitive treatment of the subject. As a proof of concept, we will apply our model to derive the differential equations that govern the dynamics of injection locked oscillators and show that it agrees with both classical and generalized [27] versions of the Adler’s equation.

Although our method for analysis of coupled LC oscillators is quite general, we

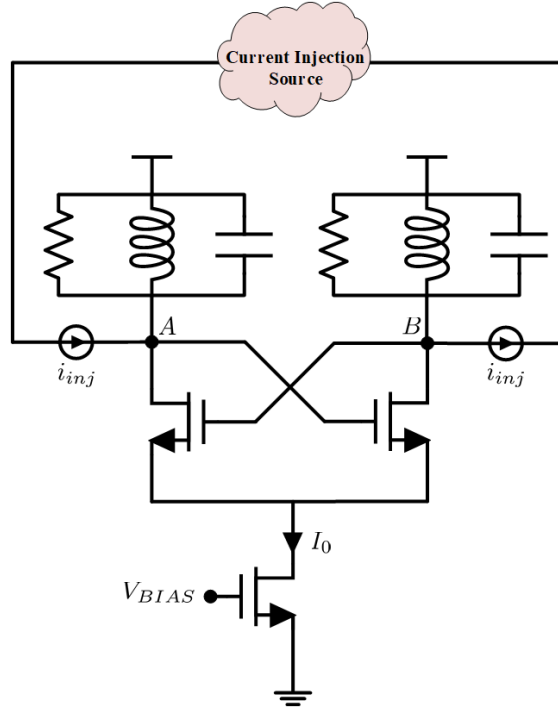


Figure 3.1: Cross coupled LC oscillator under external injection

believe it is best to illustrate the general approach with the aid of a familiar and simple example. We have chosen the cross coupled LC oscillator under injection locking, as shown in Figure 3.1, for this purpose. The external current is shown to be injected differentially in Figure 3.1 so that it does not disturb the differential operation of the oscillator.<sup>1</sup> Therefore, it is enough to only analyze the half circuit diagram shown in Figure 3.2 since dynamics of the other half of the system follows a similar path except for the trivial time delay. Under steady-state conditions,<sup>2</sup>

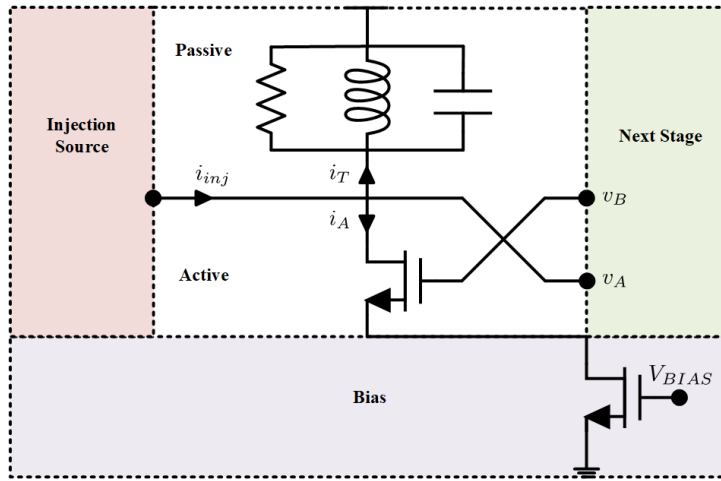


Figure 3.2: Half circuit diagram for the perturbed cross coupled oscillator

the oscillator's signals have well-defined Fourier series expansions of the form:

$$\begin{aligned}
 v_A &= V_{DD} + V_A e^{j\omega t} + c.c \\
 v_B &= V_{DD} + V_B e^{j\omega t} + c.c \\
 i_T &= I_T^0 + I_T e^{j\omega t} + c.c + \dots \\
 i_A &= I_A^0 + I_A e^{j\omega t} + c.c + \dots
 \end{aligned}$$

where  $i_T$  and  $i_A$  are the tank and active device currents,  $\omega = 1/\sqrt{LC}$ , is the resonance frequency of the LC tank, “c.c” abbreviates complex conjugates and

<sup>1</sup>This assumption becomes more critical when the injection current is not small as compared to the oscillator's internal currents.

<sup>2</sup>Strictly speaking, we should say “periodic steady-state (PSS) conditions”.

“...” represent higher order harmonic terms. If the injection current is not too strong,<sup>3</sup> we may assume that a nearly periodic form of the above steady-state solutions exists during the transient phase where we can write:

$$\begin{aligned}
v_A &= V_{DD} + V_A(t) e^{j\omega t} + c.c \\
v_B &= V_{DD} + V_B(t) e^{j\omega t} + c.c \\
i_T &= I_T^0 + I_T(t) e^{j\omega t} + c.c + \dots \\
i_A &= I_A^0 + I_A(t) e^{j\omega t} + c.c + \dots
\end{aligned} \tag{3.1}$$

Here the “complex envelopes” of the signals, that is  $V_A$ ,  $I_T$ ,  $\dots$ , are slowly varying functions of time as compared to the fast background oscillations captured by  $e^{j\omega t}$  terms. Our goal is to derive differential equations that govern the dynamics of the envelope signals so that by a subsequent analysis, we can determine the stability of their possible steady-state values. The transient dynamic model can also be used to investigate other important questions, like locking speed or phase noise performance of the system, but our focus here would be primarily on determining the steady state behavior of the system.

To this end, we use Figure 3.2, which shows the various currents flowing into node A of the oscillator to write:

$$i_T + i_A = i_{inj} \quad \Rightarrow \quad \frac{d}{dt} i_T + \frac{d}{dt} i_A = \frac{d}{dt} i_{inj}$$

where in above, we have differentiated the main KCL equation in order to end up with a second order differential equation, rather than an integro-differential equation, for our system. For convenience, let us introduce the notation  $j_x = \frac{d}{dt} i_x$

---

<sup>3</sup>In the mathematical formalism of averaging methods, the terms “weak” and “strong” injections, have more specific meanings in terms of difference between the results of the exact and the averaged models. In practice, one might rely on predictions of the averaged model as long as they are in good agreement with numerical or experimental observations.

so that the last equation becomes:

$$j_T + j_A = j_{inj} \quad (3.2)$$

We define the corresponding time variant envelopes for  $j_T$  and  $j_A$  signals via:

$$j_T = J_T(t) e^{j\omega t} + c.c + \dots$$

$$j_A = J_A(t) e^{j\omega t} + c.c + \dots$$

and substitute them in (3.2) to get:

$$J_A e^{j\omega t} + J_T e^{j\omega t} + \overline{J_A} e^{-j\omega t} + \overline{J_T} e^{-j\omega t} + \dots = j_{inj}$$

$$\Rightarrow$$

$$J_A + J_T + \overline{J_A} e^{-2j\omega t} + \overline{J_T} e^{-2j\omega t} + \dots = j_{inj} e^{-j\omega t}$$

Next, we average the last equation from  $t$  to  $t + T$  where  $t$  is any arbitrary time and  $T = 2\pi/\omega$  to get:

$$\begin{aligned} & \frac{1}{T} \int_t^{t+T} J_A(\tau) d\tau + \frac{1}{T} \int_t^{t+T} J_T(\tau) d\tau \\ & + \frac{1}{T} \int_t^{t+T} \overline{J_A(\tau)} e^{-2j\omega\tau} d\tau + \frac{1}{T} \int_t^{t+T} \overline{J_T(\tau)} e^{-2j\omega\tau} d\tau \\ & + \frac{1}{T} \int_t^{t+T} \dots = \frac{1}{T} \int_t^{t+T} \frac{dj_{inj}}{d\tau} e^{-j\omega\tau} d\tau \end{aligned}$$

However,  $J_A(\tau)$  and  $J_T(\tau)$  as well as their complex conjugates and the higher order harmonic coefficients are nearly constant during the integration interval and we may write:

$$\begin{aligned} \frac{1}{T} \int_t^{t+T} \overline{J_A(\tau)} e^{-2j\omega\tau} d\tau &\approx 0 \quad , \quad \frac{1}{T} \int_t^{t+T} J_A(\tau) d\tau \approx J_A(t) \\ \frac{1}{T} \int_t^{t+T} \overline{J_T(\tau)} e^{-2j\omega\tau} d\tau &\approx 0 \quad , \quad \frac{1}{T} \int_t^{t+T} J_T(\tau) d\tau \approx J_T(t) \\ \frac{1}{T} \int_t^{t+T} \dots &\approx 0 \end{aligned}$$

With the aid of these approximations, we get to a simple, yet powerful, equation that can be used for analysis of weakly perturbed LC oscillators:

$$\begin{aligned} J_T(t) + J_A(t) &= P(t) \\ P(t) &:= \frac{1}{T} \int_t^{t+T} \frac{di_{inj}}{d\tau} e^{-j\omega\tau} d\tau \end{aligned} \quad (3.3)$$

We call  $P(t)$ , the “average excitation function”.

Equation (3.3) is our starting point for analyzing general coupled oscillators problems. What needs to be done for each specific problem is to:

1. Simplify the expressions for  $J_A(t)$  and  $J_T(t)$  as much as possible.
2. Calculate  $P(t)$  for the particular coupling mechanism in question.

### 3.3 Injection locking and generalized Adler’s equations

We now carry out the above steps for the injection locked, cross coupled LC oscillator in Figure 3.1. The easiest term in (3.3) to calculate, is  $J_T$  thanks to simplicity of the linear equations governing the  $i - v$  characteristics of the LC tank. For notational convenience, we define  $V := V_A$  so that we can write:

$$\begin{aligned} j_T &= C \frac{d^2}{dt^2} (V e^{j\omega t}) + \frac{1}{R} \frac{d}{dt} (V e^{j\omega t}) + \frac{1}{L} V e^{j\omega t} + c.c \quad \Rightarrow \\ j_T &= \left( C\ddot{V} + 2jC\omega\dot{V} + \frac{\dot{V}}{R} + j\frac{\omega V}{R} \right) e^{j\omega t} + c.c \quad \Rightarrow \\ J_T &= C\ddot{V} + 2jC\omega\dot{V} + \frac{\dot{V}}{R} + j\frac{\omega V}{R} \end{aligned}$$

where the dot notation is used to show differentiation with respect to time. In the above expression for  $J_T$ , the second and third terms are similar (linear in  $\dot{V}$ ) but

the ratio of the magnitudes of the former to the latter is proportional to  $Q = \omega RC$ .

Therefore, we may neglect the  $\dot{V}/R$  term in above and get:

$$J_T \approx C\ddot{V} + 2jC\omega\dot{V} + j\frac{\omega V}{R}$$

Next, notice that while the last two terms in above are on the order of  $\omega$ , the first term involves the second derivative of  $V$  which is assumed to be slowly varying as compared to  $e^{j\omega t}$ . Therefore, the sum of the last two terms should dominate the  $C\ddot{V}$  term and we may approximate:

$$J_T \approx 2jC\omega\dot{V} + j\frac{\omega V}{R}$$

Finally, let us introduce the usual amplitude and phase variables such that  $V(t) = A(t) e^{j\theta(t)}$  and get:

$$J_T = \left( 2j\omega C\dot{A} - 2\omega C A\dot{\theta} + j\frac{A\omega}{R} \right) e^{j\theta} \quad (3.4)$$

Next, we find a simple expression for the  $J_A$  term in (3.3). We start by setting up the appropriate notation and writing the (time variant) Fourier expansion of the active current as:

$$i_A(t) = I_A^{(0)} + I_A e^{j\omega t} + c.c + \dots$$

Applying an averaging technique similar to what was done in the derivation of (3.3), reveals that the time variant coefficients (envelopes) may still be calculated by the familiar ‘‘Fourier trick’’:

$$I_A^{(0)} = \frac{1}{T} \int_t^{t+T} i_A(\tau) d\tau$$

$$I_A = \frac{1}{T} \int_t^{t+T} i_A(\tau) e^{-j\omega\tau} d\tau$$

Next, we use a simple current-steering model for calculation of the above coefficients. This is a non-essential but quite helpful simplification as it allows us to

focus on the more important aspects of our technique for the time being. Later in Chapter 5, we will show how to deal with more realistic cases whereby we rely on efficient numerical simulations to approximate these coefficients. As shown in Figure 3.3, we assume that sharp current steering happens in the cross coupled pair such that transistors take turns in drawing the total tail current,  $I_0$ , during each cycle. As a result we can assume that current  $i_A$  in Figure 3.3 is equal to  $I_0$  during the interval  $[t_1, t_2]$  where:

$$\omega t_1 + \theta + \pi \equiv -\pi/2$$

$$\omega t_2 + \theta + \pi \equiv \pi/2$$

It is now easy to calculate the time variant Fourier coefficients:

$$I_A^{(0)} = \frac{1}{T} \int_t^{t+T} I_A(\tau) d\tau = \frac{1}{T} \int_{t_1}^{t_2} I_0 d\tau = \frac{I_0}{2}$$

The calculations for the fundamental coefficient is also straightforward and gives:

$$\begin{aligned} I_A^{(1)} &= \frac{1}{T} \int_t^{t+T} i_A(\tau) e^{-j\omega\tau} d\tau = \frac{I_0}{T} \left( \frac{-1}{j\omega} \right) e^{-j\omega\tau} \Big|_{t_1}^{t_2} \Rightarrow \\ I_A^{(1)} &= \frac{jI_0}{T\omega} e^{j\theta} \left( e^{j\pi/2} - e^{j3\pi/2} \right) \Rightarrow \\ I_A^{(1)} &= -\frac{I_0}{\pi} e^{j\theta} \end{aligned}$$

We now differentiate the expression for  $i_A$  in order to get to  $J_A$  which was our original target:

$$\begin{aligned} i_A &= \frac{I_0}{2} - \frac{I_0}{\pi} e^{j\theta} e^{j\omega t} + c.c + \dots \Rightarrow \\ j_A &= \frac{d}{dt} \left( \frac{-I_0}{\pi} e^{j\theta} e^{j\omega t} \right) + c.c + \dots \Rightarrow \\ j_A &= -\frac{I_0}{\pi} \left\{ \frac{d}{dt} (e^{j\theta}) e^{j\omega t} + e^{j\theta} \frac{d}{dt} (e^{j\omega t}) \right\} + c.c + \dots \Rightarrow \\ J_A &\approx -\frac{j\omega I_0}{\pi} e^{j\theta} \end{aligned} \tag{3.5}$$

where in the last step, we have once again used the fact that  $\theta(t)$  is a slowly varying function of time as compared to  $e^{j\omega t}$  to simplify the final result.

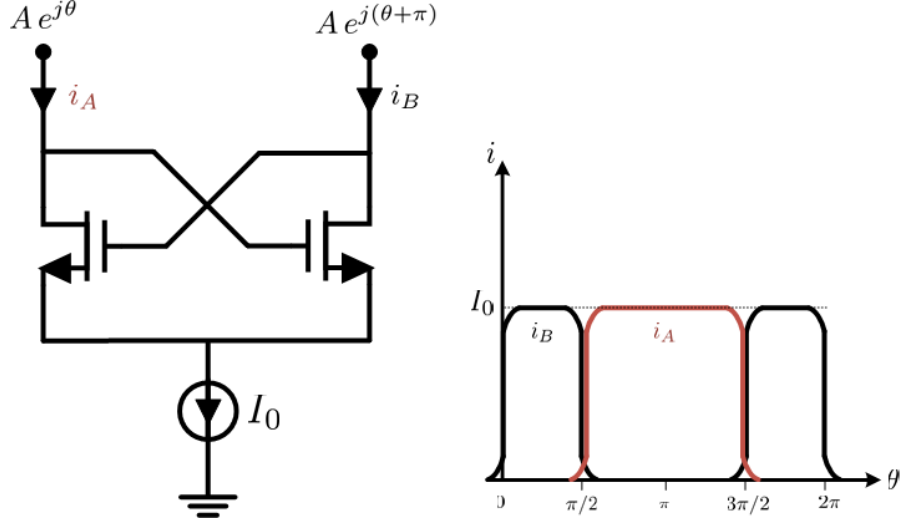


Figure 3.3: The sharp current steering model for the active current generation

Our final step in the formulation of injection locked, cross coupled oscillator is to calculate the “average excitation function” term or  $P(t)$  in (3.3). For this, we assume that the external injection current has the form of:

$$i_{inj} = I_{inj} \cos(\Omega t) = \frac{I_{inj}}{2} e^{j\Omega t} + \frac{I_{inj}}{2} e^{-j\Omega t}$$

where  $\Omega$  is the injection source frequency which is assumed to be different but close to that of the free running oscillator. We have:

$$\frac{d}{dt} i_{inj} = \frac{j}{2} \Omega I_{inj} e^{j\Omega t} - \frac{j}{2} \Omega I_{inj} e^{-j\Omega t}$$

Let us define a frequency offset variable,  $\Delta\omega := \Omega - \omega$ , and use (3.3) to write:

$$P(t) = \frac{j \Omega I_{inj}}{2T} \left( \int_t^{t+T} e^{j\Delta\omega\tau} d\tau - \int_t^{t+T} e^{-2j\omega\tau} e^{-j\Delta\omega\tau} d\tau \right)$$

For close offset frequencies, i.e.  $\Delta\omega \ll \omega$ , the terms  $e^{j\Delta\omega\tau}$  and  $e^{-j\Delta\omega\tau}$  are nearly constant during the integration interval and therefore we have:

$$\begin{aligned} \int_t^{t+T} e^{j\Delta\omega\tau} d\tau &\approx T e^{j\Delta\omega t} \\ \int_t^{t+T} e^{-2j\omega\tau} e^{-j\Delta\omega\tau} d\tau &\approx e^{-j\Delta\omega t} \int_t^{t+T} e^{-2j\omega\tau} d\tau = 0 \end{aligned}$$

and hence our formula for  $P(t)$  is simplified to:

$$P(t) \approx \frac{j \Omega I_{inj}}{2} e^{j \Delta \omega t} \quad (3.6)$$

Putting everything together, we substitute equations (3.4) through (3.6) in (3.3) and get:

$$2j\omega C \dot{A} - 2\omega C A \dot{\theta} + j \frac{A\omega}{R} - \frac{j\omega I_0}{\pi} = \frac{j \Omega I_{inj}}{2} e^{j(\Delta\omega t - \theta)}$$

Separating the real and imaginary parts of the above equation gives a system of two differential equations:

$$\begin{aligned} \dot{A} + \frac{1}{2RC} A - \frac{I_0}{2\pi C} &= \frac{\Omega I_{inj}}{4\omega C} \cos(\Delta\omega t - \theta) \\ A \dot{\theta} &= \frac{\Omega I_{inj}}{4\omega C} \sin(\Delta\omega t - \theta) \end{aligned} \quad (3.7)$$

These last equations define a non-autonomous system of differential equations in terms of dynamic variables  $A$  and  $\theta$ . However, if we define a new “excess phase” variable  $\varphi(t)$  such that  $\theta(t) = \Delta\omega t + \varphi(t)$ , the explicit time dependence can be eliminated and (3.7) is reduced to an “autonomous” system:

$$\begin{aligned} \dot{A} + \frac{1}{2RC} A &= \frac{I_0}{2\pi C} + \frac{\Omega I_{inj}}{4\omega C} \cos \varphi \\ A \dot{\varphi} &= -A \Delta\omega - \frac{\Omega I_{inj}}{4\omega C} \sin \varphi \end{aligned} \quad (3.8)$$

Equation (3.8) can be viewed as a generalization<sup>4</sup> of **Adler’s equation** in that it captures dynamics of the amplitude as well as the phase variable and shows that in fact their dynamics are coupled together.

---

<sup>4</sup>The authors in [33] claim that this result is valid for arbitrary injection levels and is therefore another way in which it generalizes Adler’s analysis. However, we believe the “weak” injection condition should be kept in a more careful statement of this result.

Further simplification is possible in the limit of very weak injection levels where  $I_{inj} \ll I_0$ . In such cases, we may further assume that  $A$  remains close to its unperturbed steady state value, which is to say  $A \approx RI_0/\pi$  and discard the dynamics of the amplitude variable altogether. The differential equation for the phase variable can then be simplified to:

$$\dot{\varphi} = -\Delta\omega - \frac{\pi\Omega}{4Q} \frac{I_{inj}}{I_0} \sin \varphi \quad (3.9)$$

which is the classic Adler's equation.

### 3.4 Transconductive coupling and the quadrature oscillator

As our next example, we analyze the dynamics of LC quadrature oscillators which were first introduced in [1]. As shown in Figure 3.4, the LC quadrature oscillator is in fact a system of two cross coupled oscillators which are themselves coupled in an *anti-symmetric* manner as explained below. The couplers are two identical differential pairs that are biased with the  $V_c$  voltage. The oscillators are assumed to be nominally identical and since the couplers inject currents differentially into the oscillators, the oscillators differential operation are preserved. We have identified the two oscillators by numbers "1" and "2" and their first and second stages by letters "A" and "B" to arrive at the labeling convention used in Figure 3.4. The anti-symmetric nature of coupling is due to the fact that while the current injected into node 1A is controlled by the signal at node 2A, the current injected into node 2A is controlled by the signal at node 1B. Because the differential operation of each oscillator is preserved, it is again enough to only analyze the half circuit diagrams shown in Figure 3.5. It has been observed [34, 33] that an additional phase shift in

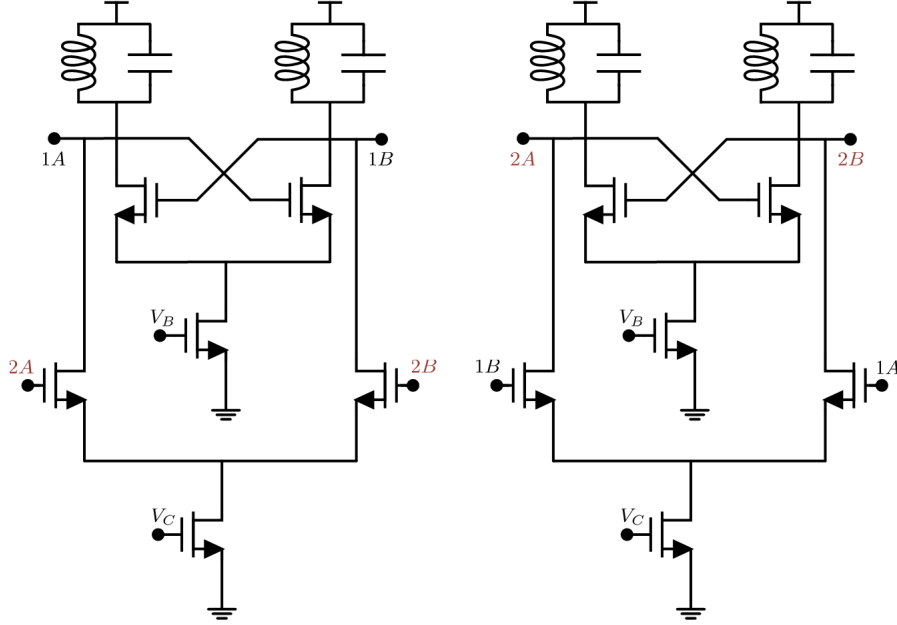


Figure 3.4: Quadrature LC oscillator topology

the coupler paths enhance the quadrature oscillator performance in terms of the quadrature accuracy and phase noise. For this reason and to make our model more general in Figure 3.5, we have included explicit phase shifters in the signal paths that connect the oscillators to the gate of the coupling transistors. The basic KCL equations for the two oscillators in Figure 3.5 are:

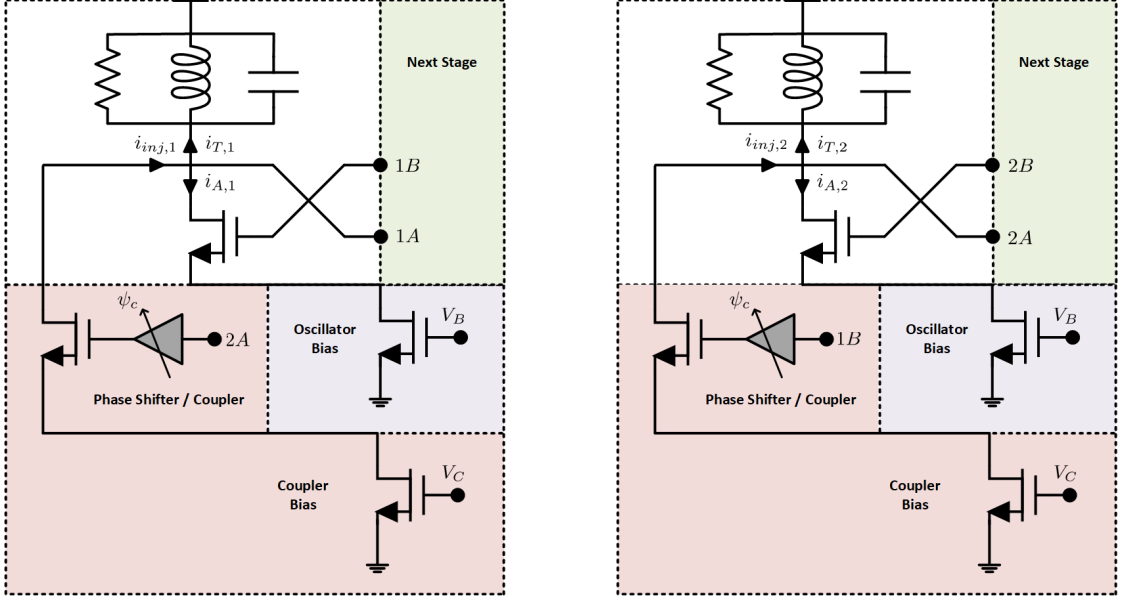
$$i_{T,1} + i_{A,1} = i_{inj,1}$$

$$i_{T,2} + i_{A,2} = i_{inj,2}$$

and therefore similar to the injection locking problem studied before, we can apply averaging methods to the above two equations and get:

$$\begin{aligned} J_{T,1} + J_{A,1} &= P_1 \\ J_{T,2} + J_{A,2} &= P_2 \end{aligned} \tag{3.10}$$

Next, we introduce amplitude and phase variables,  $\{A_1, \theta_1\}$  and  $\{A_2, \theta_2\}$  for the two oscillators where by convention, we associate the phase variables with stage



(a) Oscillator 1

(b) Oscillator 2

Figure 3.5: Half circuit diagrams of quadrature oscillators

“A” in both oscillators. In other words, we have:

$$\begin{aligned}
 v_{1A} &= V_{DD} + A_1 e^{j\theta_1} e^{j\omega t} + c.c & v_{1B} &= V_{DD} - A_1 e^{j\theta_1} e^{j\omega t} + c.c \\
 v_{2A} &= V_{DD} + A_2 e^{j\theta_2} e^{j\omega t} + c.c & v_{2B} &= V_{DD} - A_2 e^{j\theta_2} e^{j\omega t} + c.c
 \end{aligned}$$

The expressions for the  $J_{T,k}$  and  $J_{A,k}$  terms in (3.10) are similar to what were derived for the injection locked oscillator and are simply repeated here for convenience:

$$\begin{aligned}
 J_{T,1} &= \left( 2j\omega C \dot{A}_1 - 2\omega C A_1 \dot{\theta}_1 + j \frac{A_1 \omega}{R} \right) e^{j\theta_1} & J_{A,1} &= -\frac{j\omega I_0}{\pi} e^{j\theta_1} \\
 J_{T,2} &= \left( 2j\omega C \dot{A}_2 - 2\omega C A_2 \dot{\theta}_2 + j \frac{A_2 \omega}{R} \right) e^{j\theta_2} & J_{A,2} &= -\frac{j\omega I_0}{\pi} e^{j\theta_2}
 \end{aligned}$$

What remains to be done is to find formulas for  $P_1$  and  $P_2$ . In order to do this, we use the same sharp current steering model (Figure 3.3) for the coupling devices. With respect to Figure 3.5, this means that the coupling transistor connected to node 1A draws a current equal to  $I_c$  in the time interval  $[t_1, t_2]$  where  $\omega t_1 + \theta_2 + \psi_c \equiv -\pi/2$  and  $\omega t_2 + \theta_2 + \psi_c \equiv \pi/2$  and  $I_c$  is the total biasing current of the coupling

differential pair. Consequently, we have:

$$\begin{aligned} I_{inj,1}^{(1)} &= -\frac{I_c}{T} \int_{t_1}^{t_2} e^{-j\omega t} dt = \frac{I_c}{T} \frac{1}{j\omega} (e^{-j\omega t_2} - e^{-j\omega t_1}) \Rightarrow \\ I_{inj,1}^{(1)} &= -\frac{jI_c}{2\pi} e^{j\theta_2} e^{j\psi_c} (e^{-j\pi/2} - e^{j\pi/2}) = -\frac{I_c}{\pi} e^{j\theta_2} e^{j\psi_c} \end{aligned}$$

Meanwhile, the coupling transistor connected to node 2A, draws the total current  $I_c$  in the interval  $[t_3, t_4]$  where  $\omega t_3 + \theta_1 + \pi + \psi_c \equiv -\pi/2$  and  $\omega t_4 + \theta_1 + \pi + \psi_c \equiv \pi/2$ :

$$\begin{aligned} I_{inj,2}^{(1)} &= -\frac{I_c}{T} \int_{t_3}^{t_4} e^{-j\omega t} dt = \frac{I_c}{T} \frac{1}{j\omega} (e^{-j\omega t_4} - e^{-j\omega t_3}) \Rightarrow \\ I_{inj,2}^{(1)} &= -\frac{jI_c}{2\pi} e^{j\theta_1} e^{j\psi_c} (e^{j\pi/2} - e^{j3\pi/2}) = \frac{I_c}{\pi} e^{j\theta_1} e^{j\psi_c} \end{aligned}$$

Since  $\theta_1, \theta_2$  are assumed to be slowly varying functions of time, we have:

$$\begin{aligned} j_{inj,1} &\approx \frac{-j\omega I_c}{\pi} e^{j\theta_2} e^{j\psi_c} e^{j\omega t} + \frac{j\omega I_c}{\pi} e^{-j\theta_2} e^{-j\psi_c} e^{-j\omega t} + \dots \\ j_{inj,2} &\approx \frac{j\omega I_c}{\pi} e^{j\theta_1} e^{j\psi_c} e^{j\omega t} - \frac{j\omega I_c}{\pi} e^{-j\theta_1} e^{-j\psi_c} e^{-j\omega t} + \dots \end{aligned}$$

where as before  $\dots$  in above is a simplifying notation for the higher order harmonic terms. We can now use our familiar averaging argument to calculate  $P_1, P_2$  terms to be:

$$\begin{aligned} P_1 &:= \frac{1}{T} \int_t^{t+T} \frac{d i_{inj,1}}{d\tau} e^{-j\omega\tau} d\tau = -\frac{j\omega I_c}{\pi} e^{j\theta_2} e^{j\psi_c} \\ P_2 &:= \frac{1}{T} \int_t^{t+T} \frac{d i_{inj,2}}{d\tau} e^{-j\omega\tau} d\tau = +\frac{j\omega I_c}{\pi} e^{j\theta_1} e^{j\psi_c} \end{aligned}$$

Putting everything back together in (3.10), we get:

$$\begin{aligned} \left( 2j\omega C \dot{A}_1 - 2\omega C A_1 \dot{\theta}_1 + j \frac{A_1 \omega}{R} \right) e^{j\theta_1} - \frac{j\omega I_0}{\pi} e^{j\theta_1} &= -\frac{j\omega I_c}{\pi} e^{j\theta_2} e^{j\psi_c} \\ \left( 2j\omega C \dot{A}_2 - 2\omega C A_2 \dot{\theta}_2 + j \frac{A_2 \omega}{R} \right) e^{j\theta_2} - \frac{j\omega I_0}{\pi} e^{j\theta_2} &= +\frac{j\omega I_c}{\pi} e^{j\theta_1} e^{j\psi_c} \end{aligned}$$

Multiplying the first equation by  $e^{-j\theta_1}$  and the second equation by  $e^{-j\theta_2}$ , we get:

$$\begin{aligned} 2j\omega C \dot{A}_1 - 2\omega C A_1 \dot{\theta}_1 + j \frac{A_1 \omega}{R} - \frac{j\omega I_0}{\pi} &= -\frac{j\omega I_c}{\pi} e^{j(\theta_2 - \theta_1 + \psi_c)} \\ 2j\omega C \dot{A}_2 - 2\omega C A_2 \dot{\theta}_2 + j \frac{A_2 \omega}{R} - \frac{j\omega I_0}{\pi} &= +\frac{j\omega I_c}{\pi} e^{j(\theta_1 - \theta_2 + \psi_c)} \end{aligned}$$

Finally, separating the real and imaginary parts of the above, gives us:

$$\begin{aligned}
2\omega C \dot{A}_1 + \frac{A_1 \omega}{R} - \frac{\omega I_0}{\pi} &= -\frac{\omega I_c}{\pi} \cos(\theta_2 - \theta_1 + \psi_c) \\
-2\omega C A_1 \dot{\theta}_1 &= +\frac{\omega I_c}{\pi} \sin(\theta_2 - \theta_1 + \psi_c) \\
2\omega C \dot{A}_2 + \frac{A_2 \omega}{R} - \frac{\omega I_0}{\pi} &= +\frac{\omega I_c}{\pi} \cos(\theta_1 - \theta_2 + \psi_c) \\
-2\omega C A_2 \dot{\theta}_2 &= -\frac{\omega I_c}{\pi} \sin(\theta_1 - \theta_2 + \psi_c)
\end{aligned} \tag{3.11}$$

Similar to the case of injection locked oscillator, significant simplifications are possible if we assume that coupling currents are much smaller than the internal currents in the oscillators, which is to say,  $I_c \ll I_0$ . In such a case, we can again assume that the amplitude variables for both oscillators are equal to their free running value of  $RI_0/\pi$  and focus solely on the phase dynamics equations:

$$\begin{aligned}
\dot{\theta}_1 &= -\frac{1}{2RC} \frac{I_c}{I_0} \sin(\theta_2 - \theta_1 + \psi_c) \\
\dot{\theta}_2 &= +\frac{1}{2RC} \frac{I_c}{I_0} \sin(\theta_1 - \theta_2 + \psi_c)
\end{aligned} \tag{3.12}$$

Before continuing with a detailed analysis of (3.12), it is worthwhile to pause briefly here and notice the importance of the extra phase shift in the coupling paths. In fact we can immediately see from (3.12) that if  $\psi_c \equiv 0$ , then we get the identity:

$$\dot{\varphi} := \dot{\theta}_2 - \dot{\theta}_1 = 0$$

which is to say, our first order phase-reduced model of the quadrature oscillator predicts that the phase shift between the two oscillators,  $\varphi$ , remains constant and is not necessarily equal to  $\pm\pi/2$  as desired ! However, from equation (3.11), we can see that the steady state solutions with  $\varphi = \pm\pi/2$ , both correspond to the case in which the steady state amplitudes of the oscillators are equal and the same

as their free running levels  $A_1 = A_2 = RI_0/\pi$ . A stability analysis of the full dynamic system (3.11) in [33] has concluded that the only *stable* steady states of (3.11) when  $\psi_c = 0$  are in fact the above solutions with  $\varphi = \pm\pi/2$ . However, this means that without including the intentional phase shifts in the coupling paths, the quadrature oscillator suffers from a phase ambiguity problem as both  $\pm 90^\circ$  phase shifts are possible. This quadrature ambiguity problem has in fact been experimentally observed in the early quadrature oscillator designs. [33]

In the next section, we see how the phase ambiguity problem is resolved once there exist a non-zero phase shift in the coupling paths.

### 3.5 General analysis of two identical, unidirectionally coupled oscillators

In the last section, we saw that the analysis of quadrature LC oscillator reduced to a differential equation of the form:

$$\begin{aligned}\dot{\theta}_1 &= \frac{1}{2RC} \frac{I_c}{I_0} \sin(\theta_2 - \theta_1 + \psi_c + \pi) \\ \dot{\theta}_2 &= \frac{1}{2RC} \frac{I_c}{I_0} \sin(\theta_1 - \theta_2 + \psi_c)\end{aligned}$$

The above dynamic system can be considered to be a special case of the more general system schematically shown in Figure 3.6 and described by:

$$\begin{aligned}\dot{\theta}_1 &= k_a \sin(\theta_2 - \theta_1 + \psi_a) \\ \dot{\theta}_2 &= k_b \sin(\theta_1 - \theta_2 + \psi_b)\end{aligned}\tag{3.13}$$

Upon defining the relative phase shift variable,  $\varphi := \theta_2 - \theta_1$ , equation (3.13) gives:

$$\dot{\varphi} = k_b \sin(-\varphi + \psi_b) + k_a \sin(-\varphi - \psi_a)\tag{3.14}$$

Next, we notice that if we can find parameters  $k$  and  $\psi$  such that the following identity holds:

$$k \sin(-\varphi + \psi) = k_b \sin(-\varphi + \psi_b) + k_a \sin(-\varphi - \psi_a) \quad (3.15)$$

then equation (3.14) is reduced to a “*canonical*” dynamic system described by:

$$\dot{\varphi} = k \sin(-\varphi + \psi) \quad (3.16)$$

Therefore, provided that we know the solution to the canonical system given by (3.16) and the mapping from  $\{k_a, \psi_a, k_b, \psi_b\}$  to  $\{k, \psi\}$  such that the identity (3.15) holds, we have succeeded in solving the original coupled oscillator system described by (3.13) in all generality.

In order to satisfy the identity (3.15), we should have:

$$\text{Im} \{k e^{-j\varphi} e^{j\psi}\} = \text{Im} \{e^{-j\varphi} (k_a e^{-j\psi_a} + k_b e^{j\psi_b})\}$$

which always holds if we have:

$$k e^{j\psi} = k_a e^{-j\psi_a} + k_b e^{j\psi_b} \quad (3.17)$$

However, equation (3.17) is nothing but the simple vector superposition shown in Figure 3.7 and the parameters  $k$  and  $\psi$  could then be interpreted as the *effective*

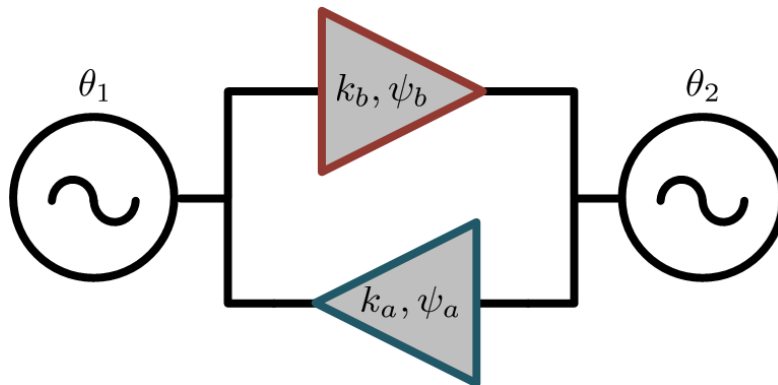


Figure 3.6: General model of two unidirectionally coupled oscillators

coupling strength and phase shifts respectively.

It is also easy to show that the only stable steady state solution of the canonical dynamic system given by (3.16) is  $\varphi_0 = \psi$ . Therefore in calculating the vector superposition in Figure 3.7, we are also finding the final phase shift reached in steady state between the oscillators in Figure 3.6.

The vector superposition method for calculating the effective coupling parameters, offers new insights on why having the additional phase shift in the coupling path of the quadrature oscillator is so beneficial. Notice that in this case we have  $\psi_a = \psi_c + \pi$  and  $\psi_b = \psi_c$  where  $\psi_c$  is the intentional phase shift in the coupling paths. Figure 3.8 shows the resulting vector superposition diagram for the quadrature oscillator system described by equation (3.12). As shown in Figure 3.8, increasing the coupling path phase shift,  $\psi_c$ , brings the superposition vector closer to the imaginary axis and therefore reduces the sensitivity of the effective coupling phase and hence quadrature accuracy to mismatches in the original coupling strength parameters,  $k_a$  and  $k_b$ . Furthermore, for a fixed set of  $k_a$  and  $k_b$ , increasing  $\psi_c$  also has the effect of increasing the effective coupling strength. It is not difficult to check that the effective coupling strength parameter,  $k$ , in the canonical

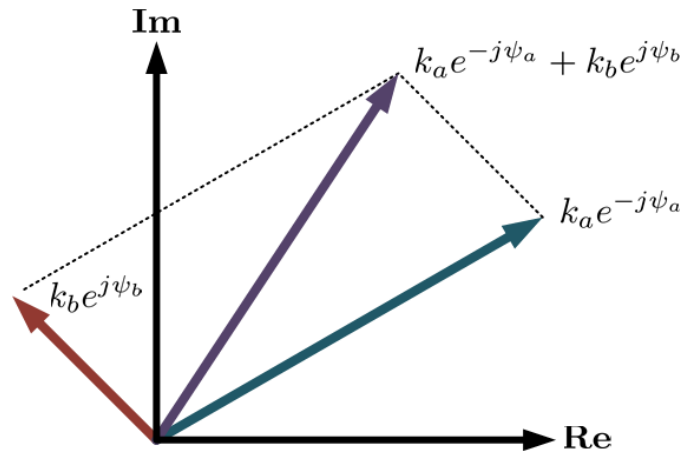


Figure 3.7: Finding effective coupling parameters by vector superposition

model has the effect of reducing the effects of noisy perturbations on the steady state phase shift between the coupled oscillators. In other words, if the phase shift between the oscillators is perturbed for any reason from its equilibrium value, a stronger coupling (larger  $k$ ) quickly restores the phase shift to its equilibrium value. This observation suggests that effects of ambient noise on disturbing the quadrature phase accuracy is greatly reduced when  $\psi_c$  is close to  $\pi/2$ . If as a result of noisy perturbations, phase of one of the oscillators instantaneously lags or leads the other oscillator's phase, the system with greater coupling strength quickly resolves the induced phase error. Therefore, increasing  $\psi_c$  should also have the effect of lowering the phase noise of the oscillators.

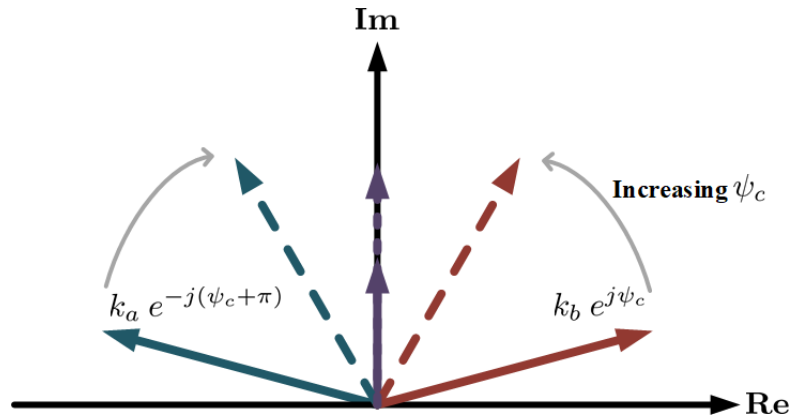


Figure 3.8: Effect of increasing  $\psi_c$  on the effective coupling strength of the quadrature oscillator

CHAPTER 4  
FREQUENCY TUNING WITH COUPLED OSCILLATORS

## 4.1 Introduction

In this chapter, we analyze the nonlinear dynamics of a unidirectionally coupled ring of oscillators with adaptive couplings. We will see that by changing the internal phase shifts of the coupling blocks, the relative phases between the oscillators and their locking frequency could be tuned. This novel frequency tuning mechanism obviates the need for including lossy varactors inside the resonators and makes it possible to realize high power sources even at frequencies close to  $f_{max}$  of transistors.

## 4.2 Nonlinear dynamic model and analysis

Consider the set of  $N \geq 3$  identical oscillators, coupled unidirectionally in the ring structure as shown in Figure 4.1. Using the Kuramoto model, we can write a set of  $N$  differential equations governing the dynamics of the oscillator's phase variables:

$$\dot{\theta}_i = \omega_0 + K \sin(\theta_{i-1} - \theta_i + \psi_c) \quad (4.1)$$

where  $\omega_0$  is the common, free running frequency of the oscillators and  $K$  and  $\psi_c$  represent the strength and inherent phase shifts of the coupler blocks respectively. Also by convention, whenever the subscript  $j$  in  $\theta_j$  is outside the  $\{1, \dots, N\}$  range, we let  $j \rightarrow \text{mod}(j, N)$  so that equation (4.1) makes sense for all integer values of the variable  $i$ . For example, we have  $\theta_0 := \theta_N$ ,  $\theta_{-1} := \theta_{N-1}$  and so for  $i = 1$ , the above equation reads  $\dot{\theta}_1 = \omega_0 + K \sin(\theta_N - \theta_1 + \psi_c)$ .

Next, we define phase-shift variables,  $\varphi_i := \theta_i - \theta_{i-1}$ , for our system so that from (4.1) we can write:

$$\dot{\varphi}_i = K \sin(\psi_c - \varphi_i) - K \sin(\psi_c - \varphi_{i-1}) \quad (4.2)$$

In steady state, the phase shifts between oscillators become constants which implies that the system should satisfy a simple equation of the form:

$$\mathbf{K} \mathbf{x} = \mathbf{0} \quad (4.3)$$

In above,  $\mathbf{x}$  is a vector in  $\mathbb{R}^N$  whose elements are  $\mathbf{x}_i := \sin(\psi_c - \varphi_i^0)$  where  $\varphi_i^0$  is the steady state value of the  $i^{\text{th}}$  phase shift variable and  $\mathbf{K}$  is the matrix in  $\mathbb{R}^N \times \mathbb{R}^N$  given by:

$$\mathbf{K} = \begin{bmatrix} K & 0 & \cdots & 0 & -K \\ -K & K & 0 & \cdots & 0 \\ \vdots & \vdots & \vdots & \ddots & \vdots \\ 0 & \cdots & \cdots & -K & K \end{bmatrix}$$

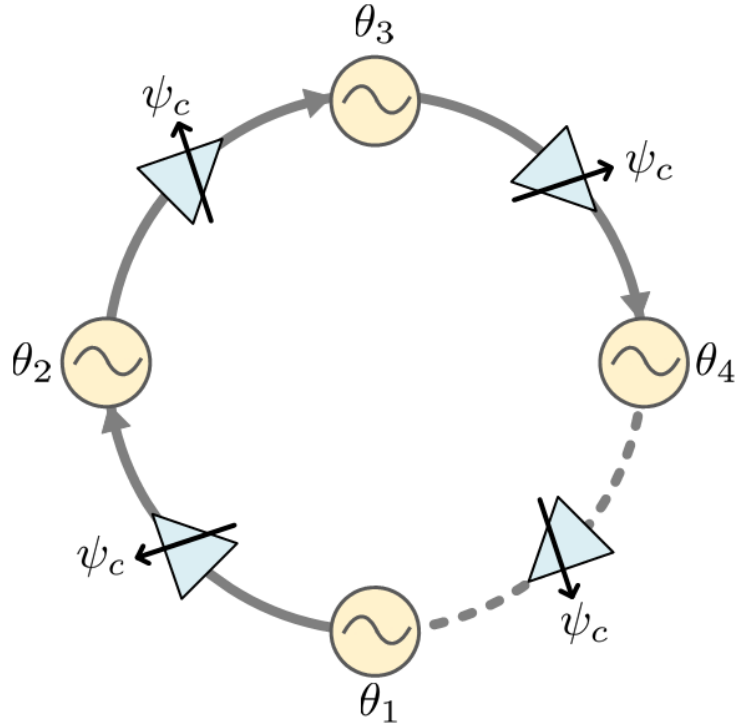


Figure 4.1: The unidirectionally coupled ring of oscillators

It should be noted that any physically relevant solution of our coupled oscillator system should also satisfy the loop consistency condition:

$$\sum_{i=1}^N \varphi_i^0 = 2k\pi \quad (\text{for some integer } k) \quad (4.4)$$

It is not difficult to see that any solution of (4.3) has the form:

$$\mathbf{x} = x \begin{Bmatrix} 1 \\ \vdots \\ 1 \end{Bmatrix}$$

or that in other words, we should have:

$$\sin(\psi_c - \varphi_i^0) = \sin(\psi_c - \varphi_1^0) \quad (1 \leq i \leq N)$$

The last equation shows that there are two possibilities for the  $i^{\text{th}}$  steady state phase shift variable:

$$\varphi_i^0 = \varphi_1^0 \pm 2n\pi \quad (4.5a)$$

$$\varphi_i^0 = 2\psi_c - \pi - \varphi_1^0 \pm 2n\pi \quad (4.5b)$$

This shows that for any given value of  $\varphi_1^0$ , there are  $2^{N-1}$  possible solutions. For each possible solution, the acceptable value of  $\varphi_1^0$  that satisfies the consistency equation (4.4), should then be determined.

Although the  $2^{N-1}$  sets of solutions described above are legitimate, fixed point solutions of the dynamic system described by (4.2), a very small subset of them are actually *stable* steady state solutions and are physically observable. To be more specific, we first classify the above  $2^{N-1}$  solutions into different groups:

**Definition 1.** Consider the dynamic system described by (4.2). We define  $S_m$  to be the set of solutions to (4.3) in which  $m$  of the steady state phase shifts are chosen from equation (4.5b).

Notice that the subscript  $m$  in  $S_m$ , can be any integer from 0 to  $N - 1$ . As shown below, the linear stability analysis reveals that only the  $S_0$  solutions are stable and all the other ones are unstable.

In order to proceed with the stability analysis, let  $\eta_i$  show the perturbation of the  $i^{th}$  phase shift variable from its steady state value of  $\varphi_i^0$ . Linearizing (4.2) around the fixed point, we get:

$$\dot{\boldsymbol{\eta}} = \mathbf{J}_{[\varphi^0]} \boldsymbol{\eta}$$

where  $\mathbf{J}_{[\varphi^0]}$  is the Jacobian matrix evaluated at  $\boldsymbol{\varphi}^0$  and is equal to:

$$\mathbf{J}_{[\varphi^0]} = \begin{bmatrix} -J_1 & 0 & \cdots & 0 & J_N \\ J_1 & -J_2 & 0 & \cdots & 0 \\ \vdots & \vdots & \vdots & \ddots & \vdots \\ 0 & \cdots & \cdots & J_{N-1} & -J_N \end{bmatrix}$$

where  $J_i := K \cos(\psi_c - \varphi_i^0)$ . Moreover, it is not difficult to show that for  $2 \leq i \leq N$ , if  $\varphi_i^0$  is chosen from (4.5a), we have  $J_i = J_1$  and if instead  $\varphi_i^0$  is chosen from (4.5b), we have  $J_i = -J_1$ . In what follows, let us assume that  $J_1 \neq 0$  which is to say  $\varphi_1^0 \neq \psi_c \pm \pi/2$ . Otherwise the Jacobian matrix would become identical to zero and the linear stability analysis would be inconclusive. This does not hurt the generality of our final result because solutions in which  $\varphi_i^0 = \psi_c \pm \pi/2$  dictate precise values for  $\psi_c$  in order to satisfy the loop consistency condition (4.4), which *almost surely* (in the technical sense of the phrase) does not happen in practice.

For a steady state solution to be stable, all the eigenvalues of the associated Jacobian matrix should have negative real parts and lie in the left half of the complex plane. We now recall Gershgorin's theorem that identifies the location of eigenvalues of arbitrary matrices:

**Theorem 1** (Gershgorin Theorem). *Let  $A$  be an  $n \times n$  matrix with entries  $a_{ij}$ . For the  $i^{\text{th}}$  row of  $A$ , let  $R_i = \sum_{j \neq i} |a_{ij}|$  and  $D_i$  be the disk defined by:*

$$D_i = \{z \in \mathbb{C} : |z - a_{ii}| \leq R_i\}$$

*Then every eigenvalue of  $A$  lies within one of the  $D_i$  disks.*

An extension of the Gershgorin theorem found in [35] is particularly useful for our current purpose:

**Theorem 2** (Extended Gershgorin Theorem). *Suppose that the Gershgorin's disks as defined in Theorem 1 can be divided into two sets such that :*

$$(\cup_{i=1}^m D_i) \cap (\cup_{i=m+1}^n D_i) = \{p\}$$

*for some  $p \in \mathbb{C}$ . Then the collection  $\cup_{i=1}^m D_i$  contains at least  $m$  eigenvalues of  $A$  provided that each eigenvalue is counted by its algebraic multiplicity. Similarly, the collection  $\cup_{i=m+1}^n D_i$  contains at least  $n - m$  eigenvalues.*

For our Jacobian matrix,  $\mathbf{J}_{[\varphi^0]}$ , the diagonal elements are either  $J_1$  or  $-J_1$  and the Gershgorin disks have all equal radii of  $|J_1|$ . Therefore, as shown in Figure 4.2 for  $\varphi^0 \in S_m$ , we have  $m$  Gershgorin disk centered at  $J_1$  with a radius of  $|J_1|$  and  $N - m$  Gershgorin disks centered at  $-J_1$  with a radius of  $|J_1|$  and the two sets of circles intersect at the origin.

In order to effectively use Theorem 2, we need to determine the algebraic multiplicity of 0 as the eigenvalue of the Jacobian matrix:

**Theorem 3.** *Either the algebraic multiplicity of 0 as the eigenvalue of  $\mathbf{J}_{[\varphi^0]}$  is equal to 1 or there exists an eigenvalue for  $\mathbf{J}_{[\varphi^0]}$  with a positive real part.*

*Proof.* To show this, we first use the nearly perfect, lower triangular shape of the Jacobian matrix to write down its characteristic polynomial:

$$P(\lambda) = (-1)^N \prod_{i=1}^N (J_i + \lambda) + (-1)^{N-1} \prod_{i=1}^N J_i$$

For notational convenience, let us define  $c = J_1$  so that  $c \neq 0$  and for  $\varphi^0 \in S_m$  we have:

$$P(\lambda) = (-1)^N \underbrace{(\lambda + c) \cdots (\lambda + c)}_{N-m} \underbrace{(\lambda - c) \cdots (\lambda - c)}_m + (-1)^{N+m-1} c^N = \sum_{n=1}^N P_n \lambda^n$$

We notice that  $P(\lambda)$  is an  $N^{\text{th}}$  degree polynomial in  $\lambda$  with real coefficients and therefore its roots are either real or come in complex conjugate pairs. Moreover, it is not difficult to see that:

$$P_0 = 0 \quad , \quad P_1 = (-1)^{N+m}(N - 2m)c^{N-1} \quad , \quad P_{N-1} = (-1)^N(N - 2m)c \quad (4.6)$$

On the other hand, if we show the roots of  $P(\lambda)$ , i.e, eigenvalues of  $\mathbf{J}_{[\varphi^0]}$ , by  $\lambda_1, \dots, \lambda_N$ , we can write:

$$P(\lambda) = (-1)^N (\lambda - \lambda_1) \cdots (\lambda - \lambda_N)$$

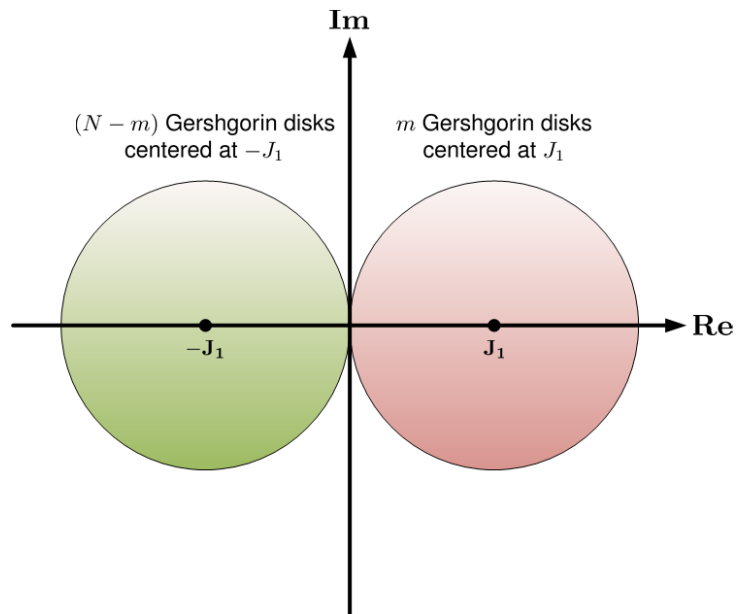


Figure 4.2: The Gershgorin disks for  $\mathbf{J}_{[\varphi^0]}$  when  $\varphi^0 \in S_m$

and therefore we have:

$$P_0 = (-1)^{2N} \prod_{i=1}^N \lambda_i \quad , \quad P_1 = (-1)^{2N-1} \sum_{j=1}^N \prod_{i \neq j} \lambda_i \quad , \quad P_{N-1} = (-1)^{N+1} \sum_{i=1}^N \lambda_i$$

Since  $P(0) = 0$ , we immediately see that  $\lambda = 0$  is an eigenvalue of the Jacobian and so we may choose to let  $\lambda_1 = 0$ . Therefore the above expressions for the characteristic polynomial coefficients become:

$$P_0 = 0 \quad , \quad P_1 = (-1)^{2N-1} \prod_{i=2}^N \lambda_i \quad , \quad P_{N-1} = (-1)^{N+1} \sum_{i=2}^N \lambda_i \quad (4.7)$$

Notice that according to (4.6),  $P_1$  does not vanish unless  $N = 2m$  in which case  $P_{N-1} = 0$  as well. This however implies that  $\sum_{i=2}^N \lambda_i = 0$  which either means that all the eigenvalues are zeros which would contradict the fact that the Jacobian matrix is non-zero or that there will be an eigenvalue with a positive real component in the right half plane. Notice that the eigenvalues can not be on the imaginary axes because that would be outside Gershgorin's disks. ■

Having determined the algebraic multiplicity of 0 as the eigenvalue of  $\mathbf{J}_{[\varphi^0]}$ , we can state the following theorem:

**Theorem 4.** *Let  $\varphi^0 \in S_m$  be a steady state solution of (4.2). If  $2 \leq m \leq N - 2$ , then  $\varphi^0$  is unstable.*

*Proof.* Since  $2 \leq m \leq N - 2$ , at least two Gershgorin disks lie on the right half plane. If  $m = N/2$ , then according to Theorem 3 there is an eigenvalue in the right half plane and we are done. Otherwise, the algebraic multiplicity of 0 is at most 1 according to Theorem 3 again and since at least two eigenvalues should be contained within the Gershgorin disks on the right half plane according to Theorem 2, at least one of them is non-zero and have a positive real part. ■

Next, we show that the remaining cases of  $m = 1$  and  $m = N - 1$  also result in unstable solutions:

**Theorem 5.** *Let  $\varphi^0 \in S_m$  be a steady state solution of (4.2). If  $m = 1$  or  $m = N - 1$ , then  $\varphi^0$  is unstable.*

*Proof.* Suppose  $m = 1$ . Then  $N - 1 \geq 2$  Gershgorin disks are centered at  $z_0 = -J_1 = -c$ . If  $c < 0$ , these  $N - 1$  Gershgorin disks are confined to the right half plane and we would have an eigenvalue with a positive real part which would prove the theorem. Therefore, we can assume  $c > 0$ . Consider the expressions for the  $P_1$  coefficient of the characteristic polynomial given by equations (4.6) and (4.7). We should have:

$$(-1)^{N+1}(N-2)c^{N-1} = (-1)^{2N-1} \prod_{i=2}^N \lambda_i$$

If  $N$  is even, then we should have  $\prod_{i=2}^N \lambda_i > 0$ . This is the product of an odd number of complex numbers which are either real or come in complex conjugate pairs. The complex conjugate pairs give a positive product when multiplied with each other. Therefore the product of the rest of the eigenvalues should also be positive. This is however the product of an odd number of real numbers and therefore not all of them could be negative numbers. This shows that at least one of the real eigenvalues should be a positive real number.

If  $N$  is odd, then we should have  $\prod_{i=2}^N \lambda_i < 0$ . This time, we have a product of an even number of complex numbers which has become negative. An even number of the terms are complex conjugate pairs and give a positive product. The remaining terms are an even number of real numbers. Notice that the number of remaining real numbers could not be zero as otherwise all the eigenvalues would be complex conjugate pairs and would give a positive product which contradicts  $\prod_{i=2}^N \lambda_i < 0$ . Therefore, we have an even number of non-zero, real eigenvalues that should give

a negative product. Therefore not all the real eigenvalues could be negative and we should again have at least one real, positive eigenvalue.

The case of  $m = N - 1$  is actually the dual of the  $m = 1$  case. In other words, we can immediately see that by changing  $\varphi_1^0$  to  $\varphi_2^0$  in equations (4.5a) and (4.5b),  $m$  changes from  $N - 1$  to 1 and the previous argument holds and this would finish the proof. For the sake of greater clarity however, let us give the alternative, longer proof for this case as well:

Suppose  $m = N - 1$ . Then  $N - 1 \geq 2$  Gershgorin disks are centered at  $z_0 = J_1 = c$ . If  $c > 0$ , then these  $N - 1$  Gershgorin disks are confined to the right half plane and we have an eigenvalue with a positive real part which would prove the theorem. Therefore, we can assume  $c < 0$ . Considering the expressions for the  $P_1$  coefficient of the characteristic polynomial given by equations (4.6) and (4.7). We should have:

$$(-1)^{2N-1}(N - 2(N - 1))c^{N-1} = (-1)^{2N-1} \prod_{i=2}^N \lambda_i$$

which shows that if  $N$  is even,  $c^{N-1} < 0$  and we should once again have  $\prod_{i=2}^N \lambda_i > 0$ . Therefore there is an eigenvalue with a positive real part as before. If  $N$  is odd, then  $c^{N-1} > 0$  and therefore we should once again have  $\prod_{i=2}^N \lambda_i < 0$  and the result follows as before. ■

Finally, we could assert which steady state solutions of our system are in fact stable:

**Theorem 6.** *The stable steady state solutions of (4.2) are the ones in which for every  $1 \leq i \leq N$ ,  $\varphi_i^0 = 2k\pi/N$  for some integer  $k$  such that  $\cos(\psi_c - 2k\pi/N) > 0$ .*

*Proof.* Clearly since  $\sin(\psi_c - \varphi_i^0) = \sin(\psi_c - \varphi_1^0)$  for every  $1 \leq i \leq N$ , the steady state condition (4.3) is satisfied. Furthermore, since  $J_i = J_1 > 0$  for  $1 \leq i \leq N$ , all the Gershgorin disks are confined to the left half plane and the steady state solution is stable. The loop consistency equation (4.4) is satisfied since  $\sum_{i=1}^N \varphi_i^0 = 2k\pi$ . ■

### 4.3 Mode switching and frequency tuning effects

Figure 4.3 shows the stability diagram for the coupled oscillator ring with  $N = 4$ . It is noteworthy that for each value of  $\psi_c$ , there are two stable fixed points that result in different phase shifts between adjacent oscillators. In principle, this means that there is an ambiguity in frequency and relative phases of the coupled oscillators as the initial conditions of the system determines exactly which mode would be excited. Nevertheless, it is always possible to reach the desired mode by properly tuning the coupler phase shift parameter as implied by the transition arrows in Figure 4.3. This is so because the transitions that happen at critical values of  $\psi_c$ , for example at  $\psi_c = \pi/2$ , are deterministic and could be relied upon to get to the desired steady state. We can also go a step further and ask what the relative sizes of the attraction basins are for different values of  $\psi_c$ . As an example, one can see from Figure 4.3 that the steady state solution with  $\varphi_i^0 = \pi/2$  is stable and hence physically observable whenever  $0 \leq \psi_c \leq \pi$ . However, as shown in Figure 4.4, numerical simulations reveal that this mode has a low probability of happening when  $\psi_c = 0$  or  $\psi_c = \pi$  and on the other hand almost surely happens when  $\psi_c = \pi/2$ . Similarly, the remaining modes corresponding to  $\varphi_i^0 = 0, \pi, 3\pi/2$  has similar probability distributions around critical values of  $\psi_c = 0, \pi, 3\pi/2$  respectively. From equation(4.1) one can immediately see that the final frequency

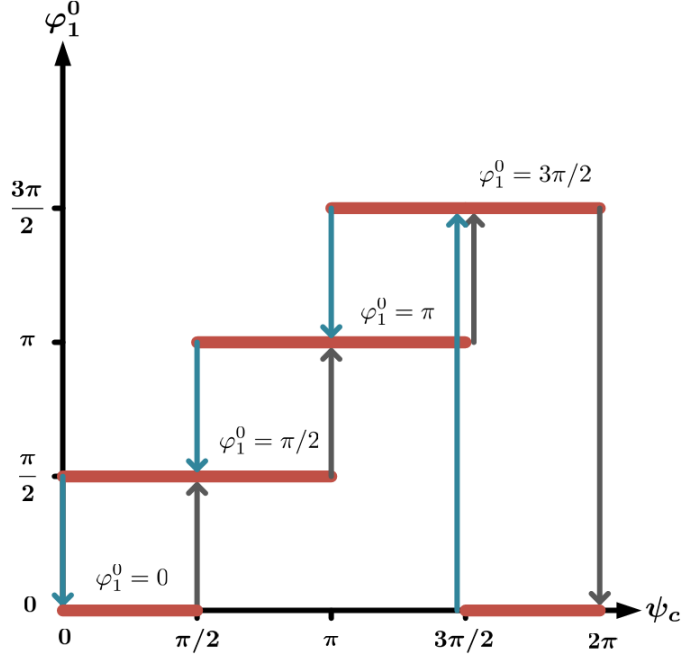


Figure 4.3: The stability diagram for the coupled oscillator ring with  $N = 4$

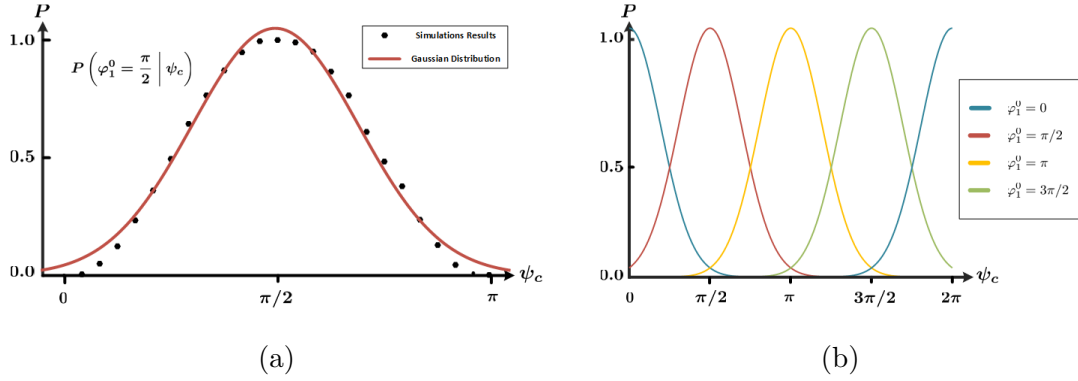


Figure 4.4: Probability of observing different modes for  $N = 4$ : (a) The  $\varphi_i^0 = \pi/2$  mode (b) All possible modes

of the coupled oscillators become equal to:

$$\omega := \dot{\theta}_1 = \omega_0 + K \sin(\psi_c - \varphi_1^0) \quad (4.8)$$

Therefore, the locking frequency depends on the coupler's internal phase shift parameter,  $\psi_c$ , which also determines the steady state value of  $\varphi_1^0$ . Clearly the frequency tuning range depends on the value of the coupler's strength parameter,  $K$  and the larger  $K$  is, the more tuning range is achieved. Figure 4.5 shows

the locking frequency as a function of the coupler's phase parameter,  $\psi_c$  when  $K = 0.1 \omega_0$ . In Figure 4.5, the frequency tuning curves are color coded to show

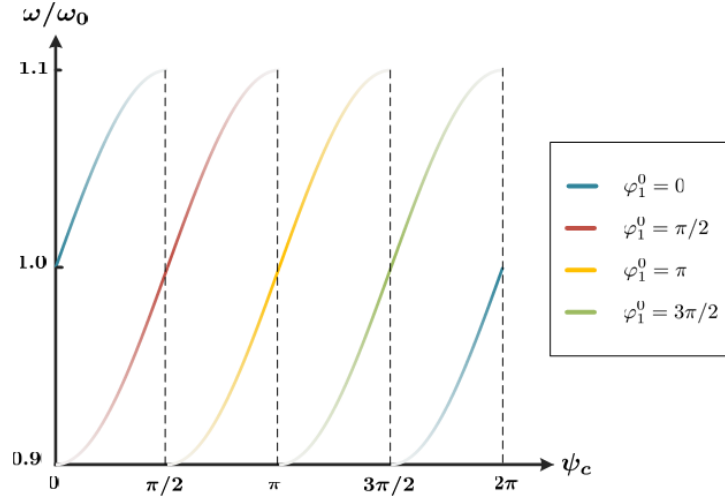


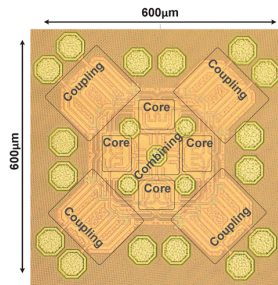
Figure 4.5: Frequency tuning curves for the coupled oscillator ring with  $N = 4$

which mode they correspond to and the intensity of the colors show the probability that each specific operating point, i.e.  $\omega$ ,  $\varphi_1^0$ , is physically observed.

In summary, the nonlinear dynamics of the coupled oscillator ring can be used to tune the oscillator's frequency without using lossy varactors inside the resonators. The steady state solutions corresponding to  $\varphi_1^0 = \pm\pi/2$  are particularly attractive for realizing a high frequency signal source. This is so because by combining the signals from all the oscillators at the center of the ring, the fourth harmonics would add constructively while the first, second and third harmonics all add to zeros. Therefore the system focuses the combined power at the fourth harmonic for efficient extraction when  $\psi_c$  is around  $\pm\pi/2$ .

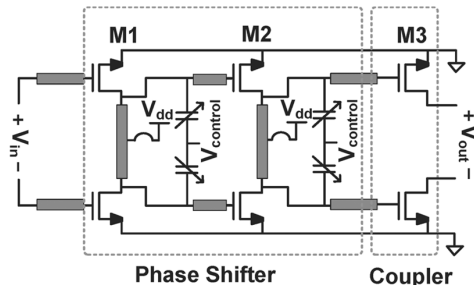
## 4.4 Experimental verifications

Our forgoing analysis has been experimentally verified with two prototype THz sources fabricated in standard 65nm CMOS technology at 0.29 and 0.32 THz center frequencies [4, 5]. Figure 4.6a shows the micrograph of the fabricated chip with the exact same structure as the simplified model previously presented in Figure 4.1 except for the additional power combining network in the middle to extract the fourth harmonic from the fundamental oscillators operating at around 75 GHz. The popular cross coupled topology has been used in implementing the core oscillators and the coupler blocks consist of a differential phase shifter followed by the actual coupler that injects signal to the next core as shown in Figure 4.6(b). The control voltage of the varactors change the phase shift of the injected signal and therefore the oscillator's locking frequency according to (4.8). The advantage of this frequency tuning mechanism is due to the fact that, since the varactors are buffered from the core resonators, they do not add loss and degrade the quality factor of the core resonators as it happens with conventional VCO structures. Figure 4.6(c-d) shows measurement results for variations of the output frequency and power levels with the varactor's control voltage. The measured peak output power is about 0.76 mW which at the time was around 10,000 times more than the power levels reported by conventional tunable sources using similar CMOS technology at such frequencies.[5]



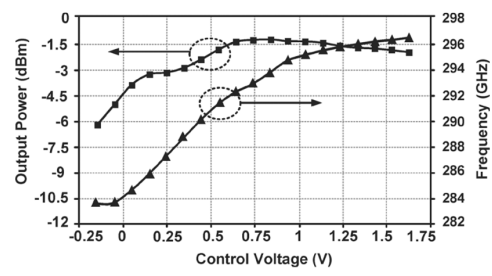
©2012, IEEE

(a)



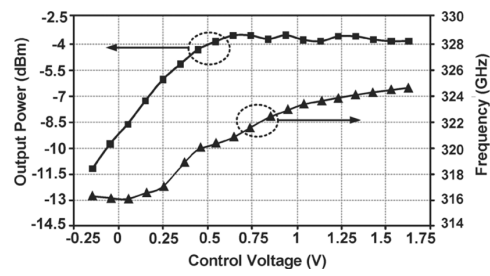
©2012, IEEE

(b)



©2012, IEEE

(c)



©2012, IEEE

(d)

Figure 4.6: (a) Chip micrograph (b) Coupling block (c-d) Measured output power and frequencies for 0.29 THz and 0.32 THz sources. Adopted with permission from [4]

CHAPTER 5  
ARBITRARY PHASE OSCILLATOR: A GENERALIZATION OF  
QUADRATURE OSCILLATORS

## 5.1 Introduction

In this chapter, we present a novel generalization of quadrature oscillators (QVCO) which we call “Arbitrary Phase Oscillator” or APO for short. In contrast to a QVCO which generates only quadrature phases, the APO is capable of continuously generating any desired phase at its output. The proposed structure employs a novel coupling mechanism to generate arbitrary phase shifts between two coupled oscillators without the need for an explicit phase shifter. Building upon the general theory we presented in Chapter 3, we provide a rigorous nonlinear dynamic analysis of our system to give a closed form formula for the generated phase shifts. The theoretical analysis is verified by numerical simulation as well as measurement results of a prototype chip fabricated in 130nm CMOS technology. The prototype APO has a frequency tuning range of 4.90 GHz to 5.65 GHz and is continuously phase tunable from  $0^\circ$  to  $360^\circ$  across the entire frequency range. The APO structure is suitable for designing scalable coupled oscillator phased arrays which offer a few advantages over conventional phased array architectures in terms of scalability, cost and complexity [6, 36, 11].

In a traditional phased array architecture, high frequency signal coming from a single source is distributed via a complex routing structure and is then phase shifted before being fed to the antenna elements for beam steering. [37, 38]. Realizing symmetric feed structures is quite challenging for large arrays and results in considerable insertion loss as well as unwanted couplings between different signal paths which may become hard to correct and compensate for, especially at mm-wave frequencies and beyond [6, 36].

In contrast, in a coupled oscillator phased array, each antenna is fed by a designated, nearby VCO and hence the long interconnects and the complex feed

structures are eliminated. The local couplings between adjacent oscillators can be used to maintain frequency coherence as well as the necessary phase shifts between the signals to steer the beam in desired directions and would obviate the need for explicit phase shifter blocks that are indispensable elements of the conventional phased arrays. This would significantly reduce cost, power consumption and complexity of such phased array systems as compared to the more conventional structures [11].

## 5.2 Overview of the APO Structure

### 5.2.1 System Level Description of the APO

The simplified schematic of our proposed APO structure is shown in Figure 5.1. It consists of two identical, three stage LC oscillators that are connected through a “multi-channel” coupling network. Different “coupling channels” connect different sets of nodes in the two oscillators as will be explained below. In order to vary the phase shift between the two oscillators, the resistive coupling devices in Figure 5.1 should be tunable. In practice, this is achieved by controlling gate voltages of coupling transistors that are biased in the deep triode region. In order to make the coupling scheme more clear, we first adopt a suitable notation for referring to the different signals in our system. We distinguish the two oscillators by numbers “1” and “2” and the three stages in each oscillator by letters “A”, “B”, and “C” so that different nodes of the oscillators are labeled as shown in Fig. 5.1. Let us also label the coupling channels by their conductance variable names,  $G_a$ ,  $G_b$ , and  $G_c$ . By convention, the subscript in the name of each coupling channel, that is  $x$  in

$G_x$ , is chosen to indicate that nodes 1A and 2X are connected in the  $G_x$  channel. We can symbolically describe the different coupling channels in Fig. 5.1, by listing the connections that each one of them provide between the two oscillators:

$$\begin{aligned}
 &1A \xleftrightarrow{G_a} 2A & 1B \xleftrightarrow{G_a} 2B & 1C \xleftrightarrow{G_a} 2C \\
 &1A \xleftrightarrow{G_b} 2B & 1B \xleftrightarrow{G_b} 2C & 1C \xleftrightarrow{G_b} 2A \\
 &1A \xleftrightarrow{G_c} 2C & 1B \xleftrightarrow{G_c} 2A & 1C \xleftrightarrow{G_c} 2B
 \end{aligned} \tag{5.1}$$

### 5.2.2 Intuition Behind APO Operation

The principle of operation for the APO oscillator is quite simple and intuitive. First, let us define “phase” variables for our oscillators. The natural way to do this is to use the familiar phasor representation for the voltage waveforms. We

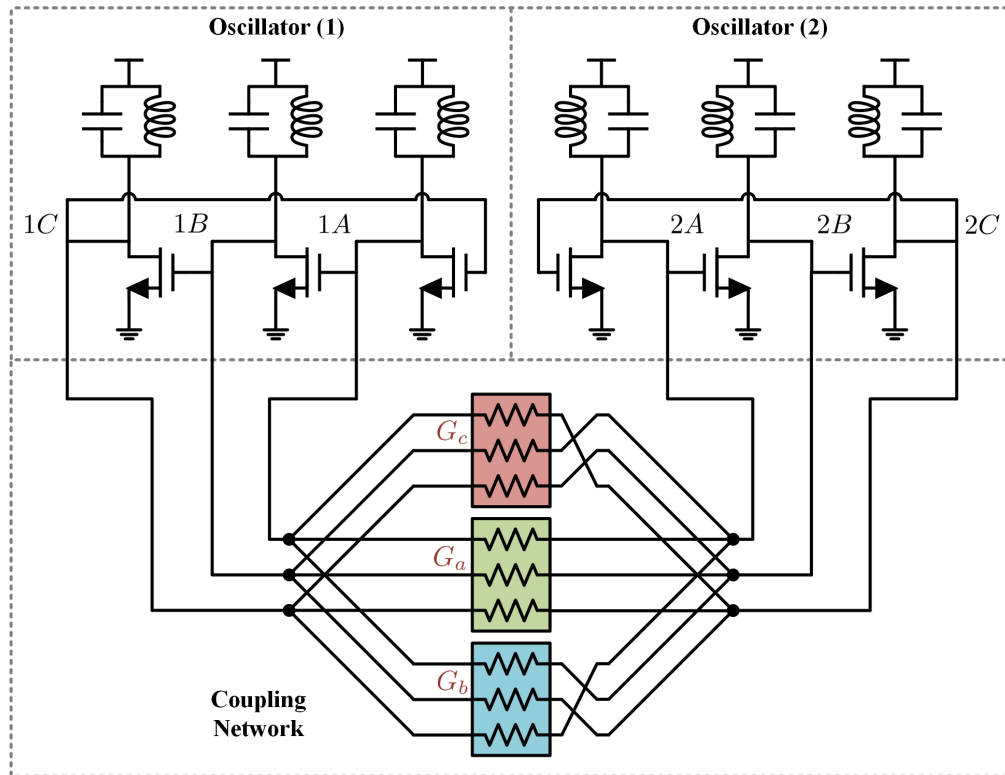


Figure 5.1: Simplified schematic of the implemented APO oscillator

choose 1A and 2A to be our reference stages in oscillator 1 and 2 respectively, and define phase variables,  $\theta_1$  and  $\theta_2$  such that:

$$v_{1A} = V_{DD} + A e^{j\theta_1} e^{j\omega t} + c.c$$

$$v_{2A} = V_{DD} + A e^{j\theta_2} e^{j\omega t} + c.c,$$

where *c.c* abbreviates complex conjugate and higher order harmonics are neglected since we assume a high quality factor for the LC resonators. Moreover, since the two oscillators are nominally identical, we have used a single variable  $A$  to show the amplitudes and another variable  $\omega$  to show the natural frequencies for both. Next, because of the intrinsic loop symmetry in the core oscillators, we have:

$$v_{1B} = V_{DD} + A e^{j\theta_1} e^{j\psi} e^{j\omega t} + c.c$$

$$v_{2B} = V_{DD} + A e^{j\theta_2} e^{j\psi} e^{j\omega t} + c.c$$

$$v_{1C} = V_{DD} + A e^{j\theta_1} e^{2j\psi} e^{j\omega t} + c.c$$

$$v_{2C} = V_{DD} + A e^{j\theta_2} e^{2j\psi} e^{j\omega t} + c.c$$

where  $\psi$  is the interstage phase shift of the oscillators. Strictly speaking there is an ambiguity in the value of  $\psi$  since both  $\psi = \pm 2\pi/3$  are consistent with having a total phase shift of  $2\pi$  around the loop. However, it is often possible to eliminate the phase ambiguity problem by careful design [39, 40]. We will refer back to this issue in section 5.3 and show that in our own implementation, the only possibility is to have  $\psi = 2\pi/3$ . Next, consider the scenario where  $G_a$  is the only active coupling channel and the other channels are turned off. It is clear that this coupler tries to completely synchronize the two oscillators and reduce the phase shift,  $\varphi := \theta_2 - \theta_1$ , to zero since otherwise, there will be unnecessary energy dissipation in the coupling resistors. Similarly the coupling channels  $G_b$  and  $G_c$  naturally induce phase shifts of  $4\pi/3$  and  $2\pi/3$  between the two oscillators, respectively. The situation gets more interesting when more than one coupling channel is active at a time. In that

case, the system is forced into making a compromise between the induced phase shifts by the active channels to minimize energy dissipation as much as possible. As shown in Figure 5.2, a rigorous dynamic analysis in section 5.4 shows that the steady state phase shift between oscillators can be found by a simple vector superposition. To be more precise, one needs to first form three vectors in the complex plane with magnitudes of  $G_a, G_b, G_c$  and polar angles of  $0, 4\pi/3, 2\pi/3$  respectively, corresponding to the three coupling channels. The steady state phase shift can then be read as the polar angle of the superposition vector. For example, if  $G_c = 2G_a$  and  $G_b = 0$  which is the case shown in Figure 5.2, then the phase shift between the oscillators becomes 90 degrees. Hence, quadrature oscillator is realized as a special case of the more general APO oscillator.

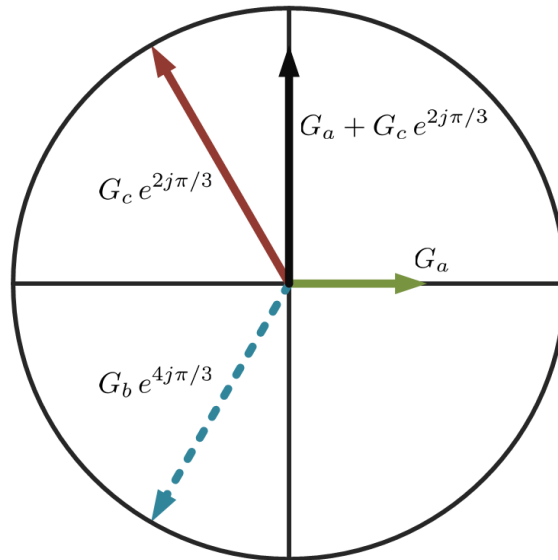


Figure 5.2: Vector superposition method for calculating steady state phase shift in APO. The case shown here is for  $G_b = 0$  and  $G_c = 2G_a$ .

## 5.3 Circuit Design Considerations

To effectively realize the proposed APO, we need to consider the practical aspects of the major circuit blocks.

### 5.3.1 Preventing Dual Mode Oscillations

In general, multiple oscillation modes are both problematic and hard to capture in numerical simulations as one needs to simulate all possible initial conditions of the oscillator to see if they happen. A careful design should provide a way of controlling the possible oscillation modes. Previous work on multiphase oscillators introduced a reliable way for switching modes in a higher order LC ring oscillator to achieve wide tuning ranges [39, 40]. However the additional active devices inevitably increase power consumption, degrade phase noise performance and make the overall design more complex. Therefore, it is worthwhile to see if a simpler

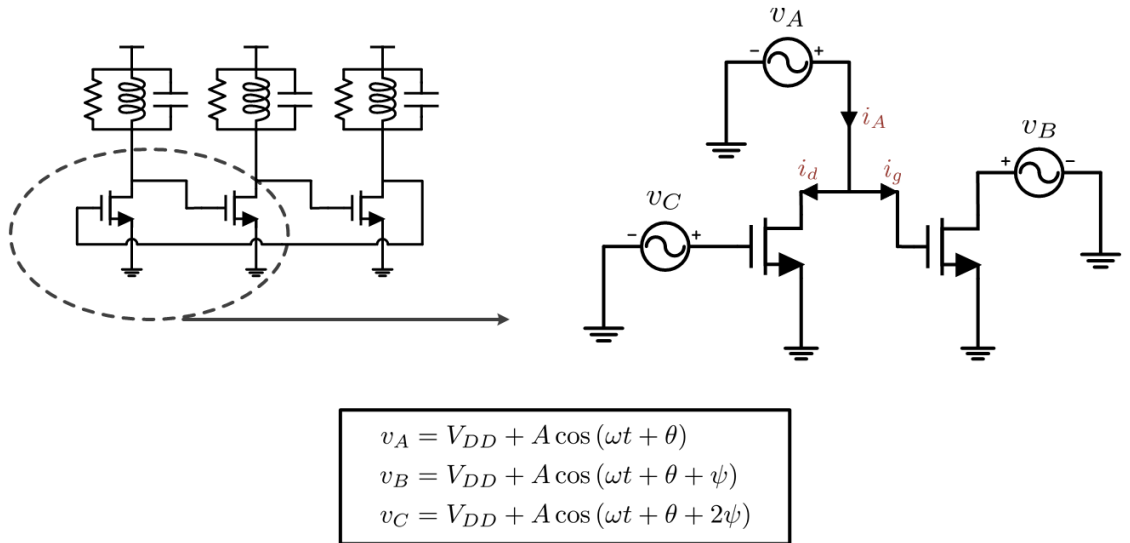


Figure 5.3: Equivalent circuit for simulating active generated power in LC ring oscillator

design would result in enough energy compensation in only one mode and hence rule out the possibility of multi mode oscillations altogether.

The schematic shown in Figure 5.3 can be efficiently used to simulate the net power generated by the active devices in all possible oscillation modes. This is so because the currents flowing into various ports of transistors, in particular  $i_d$ ,  $i_g$  and hence  $i_A$  in Figure 5.3, are uniquely determined once the voltage waveforms at all the transistor ports are specified. It does not matter how the voltage waveforms on the transistor ports are generated, whether they are enforced by ideal voltage sources or are instead the result of the actual oscillator circuitry, is irrelevant as far as the net generated power is concerned. Figure 5.4 shows such simulation results for the particular active devices used in our APO prototype. Based on these results, we see that the zeroth mode with  $\psi = 0$  never results in sustained oscillations as

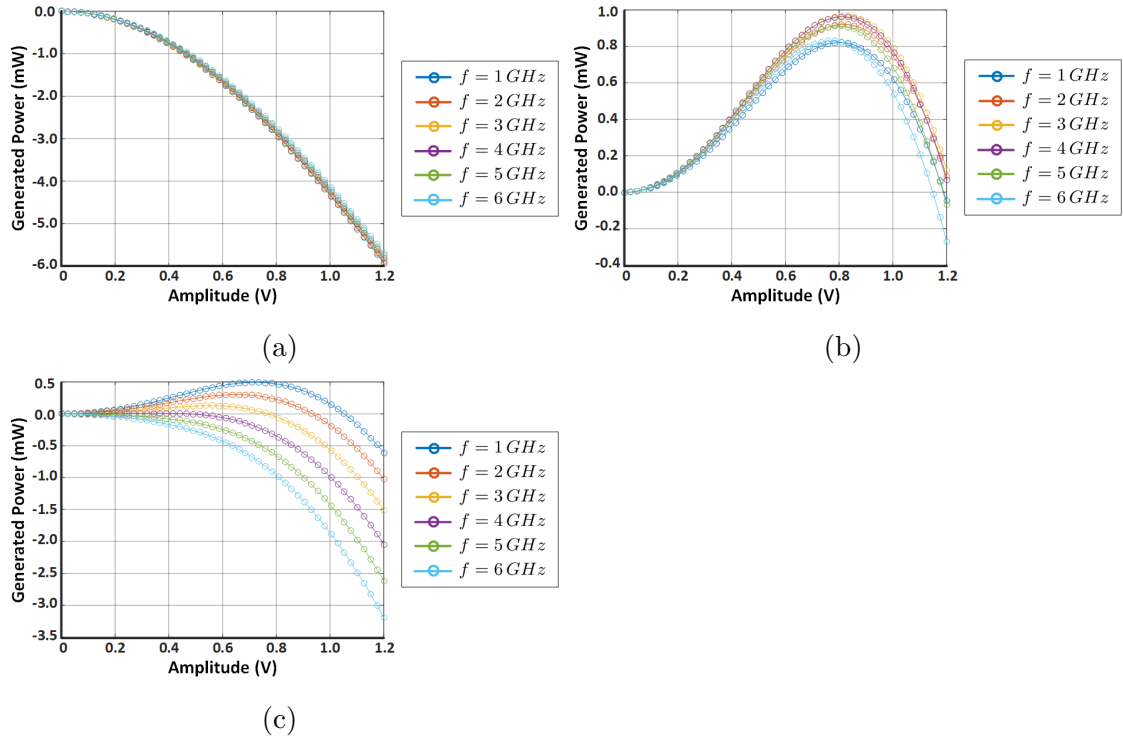


Figure 5.4: Active power generation in different modes: (a)  $\psi = 0$ , (b)  $\psi = 2\pi/3$  and (c)  $\psi = 4\pi/3$

expected. Interestingly, the second mode, corresponding to  $\psi = 4\pi/3$ , generates net power only when oscillation frequency is less than 4 GHz but fails to do so afterwards. Consequently, the only remaining possibility for frequencies greater than 5 GHz is the first mode with  $\psi = 2\pi/3$ . It is noteworthy to mention that this result is consistent with the analysis presented in [41, 42] that shows the transistor generates larger power when the phase difference between the drain and gate voltages is less than  $\pi$ .

### 5.3.2 Coupler Design

Figure 5.5 shows the schematic of the coupler cell used in our APO prototype. The most important element is the coupling transistor in the middle which is biased in the deep triode region and provides a reliable way of controlling the conductance of the coupling block. By design, the transistor's biasing is such that  $V_{DS} = 0$  and so the deep triode approximation for transistor's conductance may be used:

$$G_{ch} = \mu_n C_{ox} \frac{W}{L} (V_{GS} - V_{TH}) \quad (5.2)$$

Therefore, coupling conductance can be linearly varied by changing the control

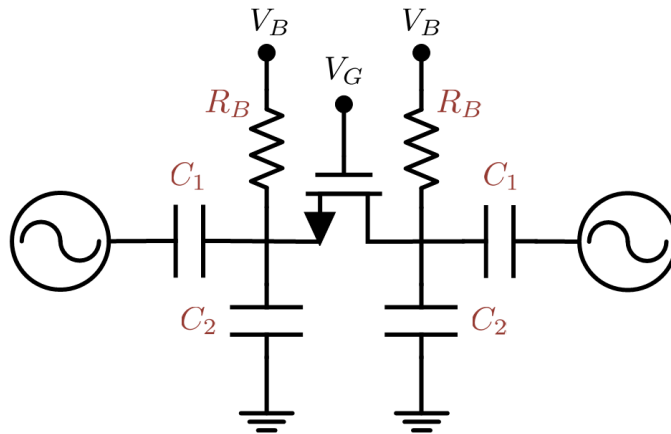


Figure 5.5: Schematic of the coupler block

voltage,  $V_G$  at the gate of the transistor. In order for the small signal model of the transistor to be valid, the RF signals at the drain/source terminals of the transistor should be sufficiently attenuated from their large signal values at the oscillator cores. The capacitive voltage divider comprised of  $\{C_1, C_2\}$  pair is employed for this purpose. Finally, resistor  $R_B$  is used for providing the DC bias of the source/drain terminals which is controlled by control voltage  $V_B$ .

The voltage division ratio due to the capacitive pair is roughly equal to  $n = C_1 / (C_1 + C_2)$  and therefore  $C_1$  should be made smaller than  $C_2$  to achieve proper signal attenuation. On the other hand, when  $C_2$  is larger than  $C_1$ , a greater portion of the coupling current (as well as the coupling noise current) flows through the  $C_2$  path to ground rather than to the oscillator cores. At the same time, the coupling current itself is proportional to the voltage signal levels at the source/drain terminals and therefore, the injected coupling current to the core of oscillators is proportional to  $n^2$ . In summary, a larger  $C_2/C_1$  ratio results in a more linear behavior of the coupling block, a better isolation of channel noise and yet a weaker effective coupling between the oscillators. In our design, we chose  $C_1 = 30 \text{ fF}$  and  $C_2 = 90 \text{ fF}$  so that  $n = 0.25$  to ensure coupling transistor's linear behavior. Notice that both  $C_1$  and  $C_2$  are chosen to be much smaller than the tank capacitance of the core oscillators,  $C \approx 500 \text{ fF}$ , so that the oscillator's frequency becomes mostly independent of the coupling channels's variable conductance and hence generated phase shifts.

Finally,  $R_B$  should be made large to both prevent leakage of the precious coupling current and also not to disturb the signal attenuation ratio. A larger resistor also injects less noise into the coupling channel and hence the oscillators. The nominal value of the biasing resistor in our design is  $R_B = 10 \text{ k}\Omega$ . The DC signal,

$V_B$  should be at least as large as the attenuated RF signal amplitudes to prevent forward biasing of source/drain and bulk PN junctions. This amounts to a biasing voltage of about  $V_B = 0.2V$  in our design.

## 5.4 Mathematical Model and Analysis

### 5.4.1 APO Dynamic Model

In Chapter 3 we developed a general framework for modelling coupled LC oscillators and used it in derivation of a generalized form of Adler's equation and analysis of quadrature oscillators. Generalizing equation (3.3) to a system of two, nominally identical, coupled oscillators is straightforward and gives:

$$\begin{aligned} J_{T,1}(t) + J_{A,1}(t) &= P_1(t) \\ J_{T,2}(t) + J_{A,2}(t) &= P_2(t) \end{aligned} \tag{5.3}$$

where similar to before, the dynamic variables in above are defined as:

$$\begin{aligned} \frac{d}{dt} i_{T,k} &= J_{T,k}(t) e^{j\omega t} + c.c + \dots \\ \frac{d}{dt} i_{A,k} &= J_{A,k}(t) e^{j\omega t} + c.c + \dots \\ P_k(t) &= \frac{1}{T} \int_t^{t+T} \frac{d i_{in,j,k}}{d\tau} e^{-j\omega\tau} d\tau \end{aligned}$$

and  $k \in \{1, 2\}$  to denote oscillators 1 and 2, respectively.

The formulae for  $J_{T,1}$  and  $J_{T,2}$  are quite similar to what was previously derived for the classic Adler's equation. We define  $V_1$  and  $V_2$  to be the (slowly time varying)

voltage envelopes for stages 1A and 2A in Figure 5.1 so that we have:

$$v_{1A} = V_{DD} + V_1 e^{j\omega t} + c.c$$

$$v_{2A} = V_{DD} + V_2 e^{j\omega t} + c.c$$

Similar to before, under the assumptions of weak coupling and high Q resonators, the expressions for  $J_{T,1}$  and  $J_{T,2}$  are simplified to:

$$J_{T,1} = 2jC\omega\dot{V}_1 + j\frac{\omega V_1}{R}$$

$$J_{T,2} = 2jC\omega\dot{V}_2 + j\frac{\omega V_2}{R}$$

Once we introduce the usual amplitude and phase variables such that  $V_1 = A_1 e^{j\theta_1}$  and  $V_2 = A_2 e^{j\theta_2}$ , we can rewrite the formulae for  $J_{T,1}$  and  $J_{T,2}$  in terms of these phase/amplitude variables as:

$$J_{T,1} = \left( 2j\omega C\dot{A}_1 - 2\omega C A_1 \dot{\theta}_1 + j\frac{A_1\omega}{R} \right) e^{j\theta_1}$$

$$J_{T,2} = \left( 2j\omega C\dot{A}_2 - 2\omega C A_2 \dot{\theta}_2 + j\frac{A_2\omega}{R} \right) e^{j\theta_2} \quad (5.4)$$

Next, we find the formulae for the  $J_{A,k}$  terms in (5.3). Let us start by writing the (time-variant) Fourier series expansion of  $i_A$ :

$$i_A = I_A^{(0)} + I_A e^{j\omega t} + \dots + c.c$$

Previously, we used the sharp current steering model of the active pair to calculate the above Fourier coefficients in terms of the oscillator's phase variable. More generally, we can use the equivalent circuit in Figure 5.3 to determine the dependence of these coefficients on the oscillator's dynamic variables. To be more specific, we know that the expression for  $i_A$  should have the form: <sup>1</sup>

$$i_A = \tilde{F}_0(A, \omega) + \tilde{F}_1(A, \omega) e^{j\theta} e^{j\omega t} + \dots + c.c \quad (5.5)$$

---

<sup>1</sup>The validity of equation (5.5), i.e., that  $\theta$  only appears as  $e^{j\theta}$  in the formula for  $i_A$ , is a direct consequence of the oscillator's loop symmetry and can be easily verified with direct simulations as well.

Moreover, the complex  $\tilde{F}_1(A, \omega)$  function can be broken down into its real and imaginary components:

$$\tilde{F}_1(A, \omega) = F(A, \omega) + j H(A, \omega)$$

and it is simple to numerically calculate these functions with standard simulation tools like Cadence Spectre. Fig. 5.6 shows such simulation results for 130nm CMOS transistors with  $W/L = 20\mu m/0.4\mu m$  that is used in our APO implementation. For our modelling purposes, we may use a narrow band approximation of (5.5) around the resonance frequency of oscillators and write:

$$i_A = \tilde{F}_0(A) + \tilde{F}_1(A) e^{j\theta} e^{j\omega t} + \dots + c.c$$

Upon differentiating the above equation, we get:

$$\frac{d}{dt} i_A = \frac{d}{dt} \left\{ \tilde{F}_0(A) \right\} + \frac{d}{dt} \left\{ \tilde{F}_1(A) e^{j\theta} \right\} e^{j\omega t} + \tilde{F}_1(A) e^{j\theta} \frac{d}{dt} \left\{ e^{j\omega t} \right\} + c.c + \dots$$

But since  $A$  and  $\theta$  are slowly varying functions of time as compared to  $e^{j\omega t}$ , we may ignore the second term in comparison to the third in above and arrive at:

$$J_A(t) \approx j\omega \tilde{F}_1(A) e^{j\theta} = j\omega F(A) e^{j\theta} - \omega H(A) e^{j\theta}$$

Therefore, in our APO system where the same active device is used for both

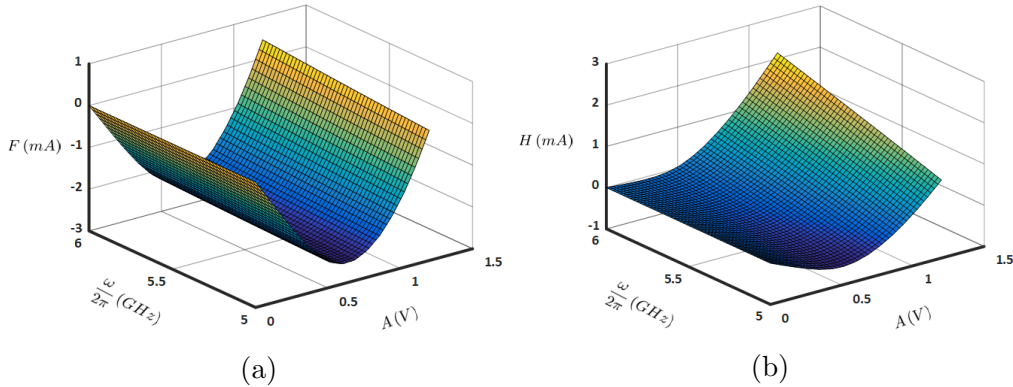


Figure 5.6: Simulated values of (a)  $F(A, \omega)$  and (b)  $H(A, \omega)$

oscillators, we simply have:

$$\begin{aligned} J_{A,1} &= j\omega F(A_1) e^{j\theta_1} - \omega H(A_1) e^{j\theta_1} \\ J_{A,2} &= j\omega F(A_2) e^{j\theta_2} - \omega H(A_2) e^{j\theta_2} \end{aligned} \quad (5.6)$$

Finally, we need to determine the  $P_k$  terms in (5.3). The total injected current into each oscillator is the summation of the injection currents due to the three coupling channels. That is, we have:

$$\begin{aligned} i_{inj,1} &= i_{inj,1}^{(a)} + i_{inj,1}^{(b)} + i_{inj,1}^{(c)} \\ i_{inj,2} &= i_{inj,2}^{(a)} + i_{inj,2}^{(b)} + i_{inj,2}^{(c)} \end{aligned}$$

where  $i_{inj,k}^{(x)}$  shows the coupling current in channel  $G_x$  that is injected into the  $k^{th}$  oscillator. Consequently, the average excitation functions for the two oscillators,  $P_1$  and  $P_2$ , follow the same superposition principle:

$$\begin{aligned} P_1 &= P_1^{(a)} + P_1^{(b)} + P_1^{(c)} \\ P_2 &= P_2^{(a)} + P_2^{(b)} + P_2^{(c)} \end{aligned}$$

We use this superposition principle along with the generic model of the coupling channels shown in Figure 5.7 to calculate  $P_1$  and  $P_2$ . In this generic model,  $v_L$  and  $v_R$  represent “left” and “right” node voltages and  $i_{L \rightarrow R}$  is the coupling current that is being injected into the right node. Of course, what “left” and “right” nodes correspond to, depends on the particular coupling channel that is being considered. Similar to before, we form a nearly periodic formulation of the problem and write:

$$\begin{aligned} v_L(t) &= V_{DD} + V_L e^{j\omega t} + c.c \\ v_R(t) &= V_{DD} + V_R e^{j\omega t} + c.c \\ i_{L \rightarrow R}(t) &= I_{L \rightarrow R}^{(0)} + I_{L \rightarrow R} e^{j\omega t} + c.c \end{aligned}$$

keeping in mind that although  $V_L$ ,  $V_R$  and  $I_{L \rightarrow R}$  are slowly varying functions of time, we might treat them as constants during one oscillation cycle.

Since the circuit is linear, superposition holds and it is readily seen that  $I_{L \rightarrow R}^{(0)} = 0$ . Furthermore, the standard common/differential mode decomposition technique can be employed for analysis at the fundamental frequency. It is clear that in the common mode, there will be no net current flow from left to right and so we only need to perform the differential mode analysis. In the differential mode, the circuit can be broken into two halves with the middle node becoming virtual ground as shown in Figure 5.8. We define  $Y_1 = jC_1\omega$  and  $Y_2 = 2G + G_B + jC_2\omega$  where  $G = 1/R$  and  $G_B = 1/R_B$  so that we can write:

$$I_{L \rightarrow R} = Y_G (V_L - V_R)$$

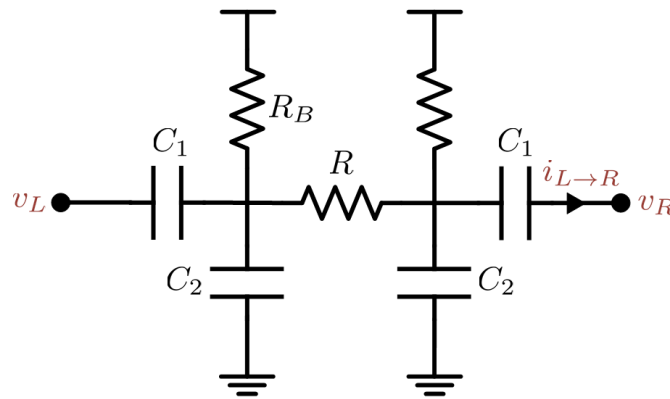


Figure 5.7: Generic model of the coupling channels

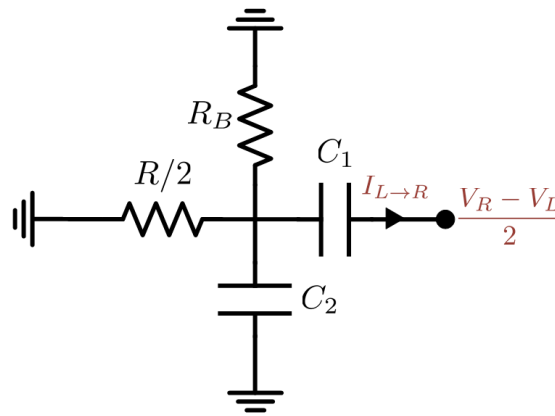


Figure 5.8: Differential mode model of the coupling channels

$$Y_G := \frac{Y_1 Y_2}{2(Y_1 + Y_2)}$$

where  $Y_G$  may be interpreted as the effective admittance of the coupling channel at the fundamental frequency. As discussed in Section 5.3, we may assume  $G_B$  is much smaller than  $G$  and  $C_2\omega$  so that  $Y_2 = 2G + jC_2\omega$  and therefore:

$$Y_G = \frac{1}{2} \frac{(jC_1\omega)(2G + jC_2\omega)}{2G + j(C_1 + C_2)\omega}$$

In order to get to a neat final result, let us introduce one additional notation: We break  $Y_G$  into two parts,  $Y_0$  and  $\tilde{Y}_G$  where  $Y_0$  is the channel's admittance when  $G = 0$  and  $\tilde{Y}_G$  is defined such that the following identity holds:

$$Y_G = Y_0 + \tilde{Y}_G$$

Simple algebraic manipulations reveal that:

$$Y_0 = \frac{j}{2} \frac{C_1 C_2}{C_1 + C_2} \omega$$

$$\tilde{Y}_G = G \cdot \frac{C_1}{C_1 + C_2} \cdot \frac{jC_1\omega}{2G + j(C_1 + C_2)\omega}$$

However, by design,  $G$  is chosen to be small compared to  $C_2\omega$  so that the capacitive divider gives a voltage division ratio of  $n = C_1 / (C_1 + C_2)$  at the fundamental frequency. Therefore, we have:

$$\tilde{Y}_G \approx \left( \frac{C_1}{C_1 + C_2} \right)^2 G = n^2 G$$

Putting everything back together, we have the following equation:

$$I_{L \rightarrow R} = j\tilde{C}\omega (V_L - V_R) + \tilde{G} (V_L - V_R)$$

where we have defined the effective capacitance and conductance parameters of the channel,  $\tilde{C}$  and  $\tilde{G}$ , to be equal to:

$$\tilde{C} = \frac{1}{2} \frac{C_1 C_2}{C_1 + C_2}$$

$$\tilde{G} = \left( \frac{C_1}{C_1 + C_2} \right)^2 G$$

Figure 5.9 shows the intuitive interpretation of the above result whereby the generic coupling channel is replaced by its equivalent model that consists of one purely capacitive and one purely conductive paths with parameters  $\tilde{C}$  and  $\tilde{G}$ , respectively.

Next, we calculate the average excitation function,  $P(t)$ , for the generic coupling channel:

$$\begin{aligned} \frac{d}{dt}i_{L \rightarrow R} &= \dot{I}_{L \rightarrow R} e^{j\omega t} + j\omega I_{L \rightarrow R} e^{j\omega t} + c.c \quad \Rightarrow \\ P(t) &= \frac{1}{T} \int_t^{t+T} \frac{d i_{L \rightarrow R}}{d\tau} e^{-j\omega\tau} d\tau \approx j\omega I_{L \rightarrow R} \quad \Rightarrow \\ P(t) &= -\tilde{C}\omega^2 (V_L - V_R) + j\omega\tilde{G} (V_L - V_R) \end{aligned}$$

Finally, we use the symbolic representation of the coupling channels (See equation (5.1)) to determine left and right nodes for different channels and write down the expressions for  $P_1$  and  $P_2$ :

$$\begin{aligned} P_1 &= (3\tilde{C}\omega^2 - j\omega\tilde{G}_T)V_1 + j\omega(\tilde{G}_a + \tilde{G}_b e^{j\frac{2\pi}{3}} + \tilde{G}_c e^{j\frac{4\pi}{3}})V_2 \\ P_2 &= (3\tilde{C}\omega^2 - j\omega\tilde{G}_T)V_2 + j\omega(\tilde{G}_a + \tilde{G}_b e^{j\frac{4\pi}{3}} + \tilde{G}_c e^{j\frac{2\pi}{3}})V_1 \end{aligned} \tag{5.7}$$

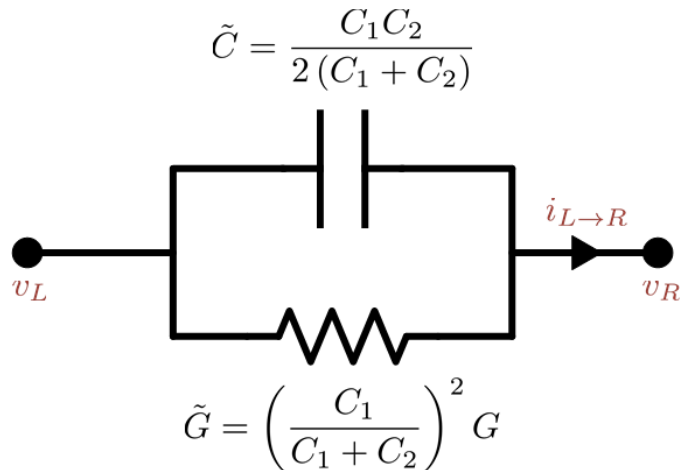


Figure 5.9: Equivalent model of the coupling channel

where we have defined  $\tilde{G}_T = \tilde{G}_a + \tilde{G}_b + \tilde{G}_c$  to simplify the final formula.

### 5.4.2 APO Dynamic Analysis

Having found simple expressions for all the relevant terms in (5.3), we are now ready to write the differential equations that capture the dynamics of the APO oscillator in terms of amplitude and phase variables. The resulting equations are:

$$\begin{aligned}
2j\omega C\dot{A}_1 - 2\omega CA_1\dot{\theta}_1 - 3\omega^2\tilde{C}A_1 + j\frac{A_1\omega}{\tilde{R}} + j\omega F(A_1) - \omega H(A_1) \\
= \\
j\omega\left(\tilde{G}_a + \tilde{G}_b e^{j2\pi/3} + \tilde{G}_c e^{j4\pi/3}\right)A_2 e^{j(\theta_2-\theta_1)} \\
\\
2j\omega C\dot{A}_2 - 2\omega CA_2\dot{\theta}_2 - 3\omega^2\tilde{C}A_2 + j\frac{A_2\omega}{\tilde{R}} + j\omega F(A_2) - \omega H(A_2) \\
= \\
j\omega\left(\tilde{G}_a + \tilde{G}_b e^{j4\pi/3} + \tilde{G}_c e^{j2\pi/3}\right)A_1 e^{j(\theta_1-\theta_2)}
\end{aligned} \tag{5.8}$$

where in above, we have defined  $\tilde{R}$ , to be:

$$1/\tilde{R} = 1/R + \tilde{G}_T \tag{5.9}$$

In principle, the above two equations form a 4 dimensional system of nonlinear differential equations whose comprehensive analysis is going to be too intensive for our current purpose. However, it is possible greatly simplify the analysis by focusing solely on dynamics of the phase variables.<sup>2</sup> In fact, one might argue that since there is no physically significant difference between the two oscillators, their

---

<sup>2</sup>This is similar in spirit to the “phase reduction” technique used in more abstract formulations of coupled oscillators, like the Kuramoto’s model. See [28] for a mathematical treatment of this subject.

amplitudes should reach a common value in steady-state. Moreover, let us assume that this final common amplitude,  $\tilde{A}$ , settles relatively soon so that from that moment till reaching the steady-state, the only time varying variables are  $\theta_1$  and  $\theta_2$ . The dynamic equations now become:

$$\begin{aligned}
& -2\omega C \tilde{A} \dot{\theta}_1 - 3\omega^2 \tilde{C} \tilde{A} + j \frac{\tilde{A}\omega}{\tilde{R}} + j\omega F(\tilde{A}) - \omega H(\tilde{A}) \\
& \quad = \\
& \quad j\omega \left( \tilde{G}_a + \tilde{G}_b e^{j2\pi/3} + \tilde{G}_c e^{j4\pi/3} \right) \tilde{A} e^{j(\theta_2 - \theta_1)} \\
& -2\omega C \tilde{A} \dot{\theta}_2 - 3\omega^2 \tilde{C} \tilde{A} + j \frac{\tilde{A}\omega}{\tilde{R}} + j\omega F(\tilde{A}) - \omega H(\tilde{A}) \\
& \quad = \\
& \quad j\omega \left( \tilde{G}_a + \tilde{G}_b e^{j4\pi/3} + \tilde{G}_c e^{j2\pi/3} \right) \tilde{A} e^{j(\theta_1 - \theta_2)}
\end{aligned} \tag{5.10}$$

Let us define the “phase shift” variable,  $\varphi = \theta_2 - \theta_1$ , between the two oscillators and also define “effective coupling strength”,  $K_c$ , and “effective coupling phase”,  $\psi_c$ , such that:

$$\tilde{G}_a + \tilde{G}_b e^{j4\pi/3} + \tilde{G}_c e^{j2\pi/3} = K_c e^{j\psi_c} \tag{5.11}$$

Subtracting the first equation from the second in (5.10), we get:

$$-2\omega \tilde{C} \tilde{A} \dot{\varphi} = j\omega \tilde{A} K_c e^{j(-\varphi + \psi_c)} - j\omega \tilde{A} K_c e^{j(\varphi - \psi_c)}$$

Finally, we let  $\rho = K_c/\tilde{C}$  and simplify the last equation to get:

$$\dot{\varphi} = -\rho \sin(\varphi - \psi_c) \tag{5.12}$$

The steady-state solutions of (5.12) are  $\varphi_0 = \psi_c$  and  $\psi_c = \pi - \psi_c$ . The standard perturbation analysis determines which one of the solutions is stable. To this end,

let  $\eta$  show the deviation of  $\varphi$  from  $\varphi_0$  so that  $\varphi = \varphi_0 + \eta$ . Linearizing (5.12) around  $\varphi_0$  gives:

$$\dot{\eta} = -\rho \cos(\varphi_0 - \psi_c) \eta$$

which clearly shows that the stable solution is  $\varphi_0 = \psi_c$ .

To summarize, the final result predicted by the dynamic analysis of the APO is that, when the coupling conductances are set to  $G_a$ ,  $G_b$  and  $G_c$ , the generated phase shift will be equal to:

$$\text{Arg} \left( G_a + G_b e^{j4\pi/3} + G_c e^{j2\pi/3} \right) \quad (5.13)$$

and this result is the rigorous basis for the intuitive vector superposition method previously introduced in Figure 5.2.

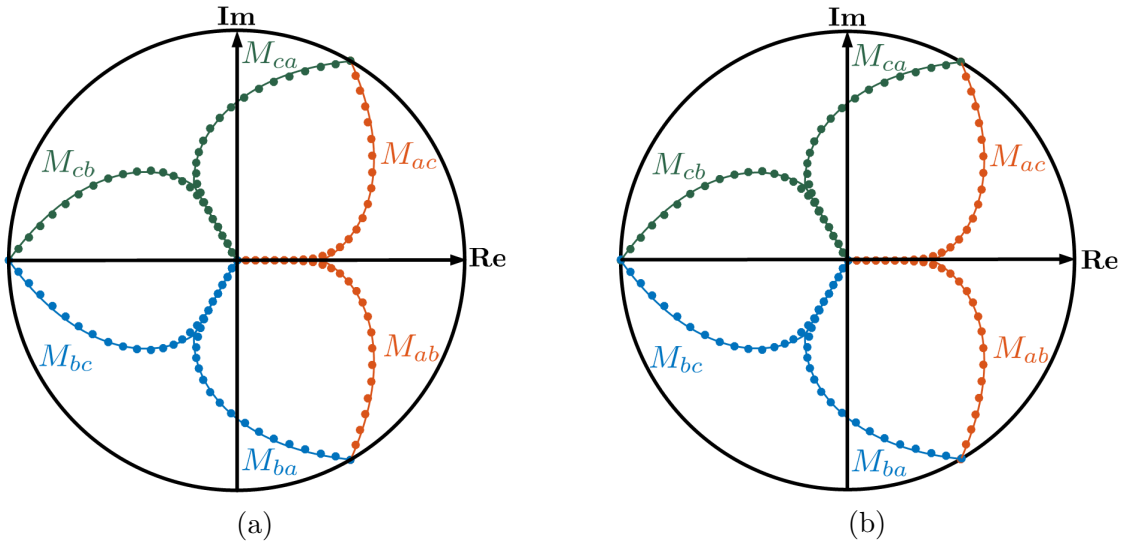


Figure 5.10: Analytical v.s numerical results for the APO phase shift pattern. (a)  $f_0 = 5.05$  GHz and (b)  $f_0 = 5.85$  GHz

### 5.4.3 APO Dynamic Analysis Verification

Figure 5.10 compares the analytical result for predicting the APO's generated phase shifts with simulation results from Cadence Spectre. The simulation results are based on the actual PDK models of the 130nm technology used for the prototype fabrication. In Figure 5.10, we have identified different operation modes of the APO by labels  $M_{xy}$ . By convention,  $M_{xy}$  is the operation mode in which the gate voltage of the  $G_x$  coupler is fixed at  $1.2V$ , while that of the  $G_y$  coupler is gradually varied from  $0V$  to  $1.2V$  and the remaining coupler gate voltage remains fixed at  $0V$ . A point  $z = re^{j\varphi}$  is placed on the  $M_{xy}$  curve to indicate that  $\varphi$  is the steady state phase shift measured when  $V_y/V_x = r$ . It is worth mentioning that  $r$  does not present the amplitude of oscillation which is almost constant for all the points in Figure 5.10 and is determined by the oscillators dynamics. The solid line represents the analytical model and the filled dots show the simulation results.

In order to produce the analytic curve, we have simply used the deep triode approximation for calculating the  $G_x$  terms in (5.13). That is, when  $V_{GS} \geq V_{TH}$  we have used (5.2) to calculate  $G_x$  and have set  $G_x = 0$  otherwise. The only fitting parameter was the threshold voltage,  $V_{TH}$ , whose optimal value is found to be  $0.2V$ .

As evident from Figure 5.10, the agreement between the theoretical model and numerical simulations is remarkable, given the various approximations made in getting to the simple analytical model. Furthermore, we can see that both methods predict the APO phase shift should be frequency independent and essentially be a function of the coupler gate voltages. In principle, this would eliminate any need for re-calibration to maintain a target phase shift when the APO frequency is changed which can be attractive for some applications. For example, in a phased

array system used for FM communications, this would minimize the “beam squint” problem in which the direction of the radiated beam would fluctuate with frequency modulations.

## 5.5 Prototype Implementation

Figure 5.11 shows the micrograph of the prototype APO chip, fabricated in a 130nm CMOS technology. The oscillator core transistors are NMOS devices with aspect ratio of  $W/L = 20\mu m/0.5\mu m$  while those in the coupling blocks have  $W/L = 4\mu m/0.4\mu m$ . In both cases, the channel lengths are maximized to lower their flicker noise. The fixed capacitors in the oscillators tanks as well as the coupler blocks, are all implemented as metal-insulator-metal (MIM) capacitors. The nominal value of the tank capacitor is  $400\text{ fF}$  and that of  $C_1$  and  $C_2$  in the coupling block (see

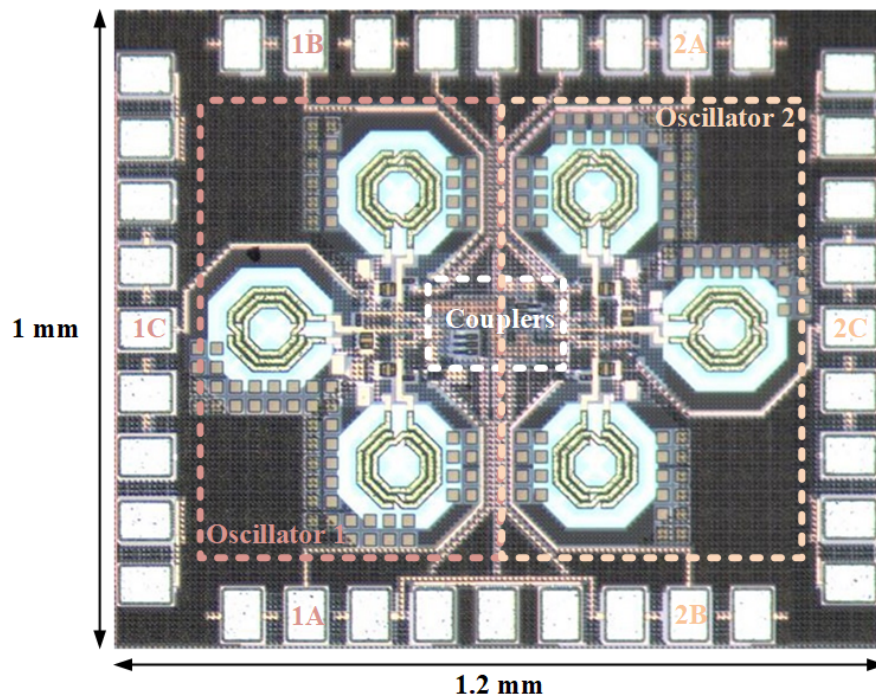


Figure 5.11: APO chip micrograph

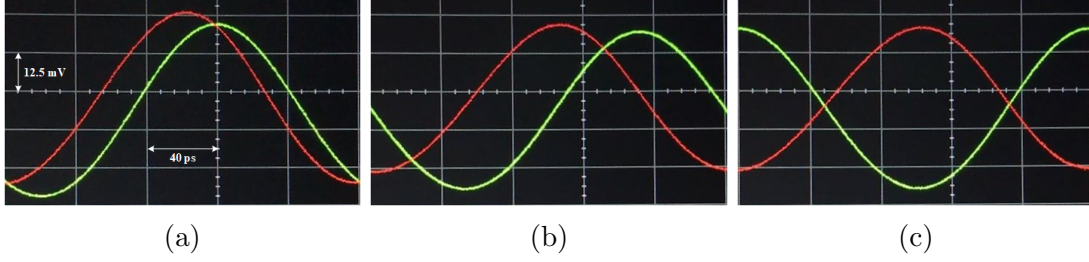


Figure 5.12: Captured APO waveforms on the oscilloscope at  $f_0 = 4.90$  GHz.  $V_a$ ,  $V_b$  and  $V_c$  are the coupler gate voltages for the  $G_a$ ,  $G_b$  and  $G_c$  channels respectively.

- (a)  $V_a = 1.2 V$     $V_b = 0.0 V$     $V_c = 0.0 V$   
(b)  $V_a = 1.2 V$     $V_b = 0.0 V$     $V_c = 1.2 V$   
(c)  $V_a = 0.0 V$     $V_b = 0.0 V$     $V_c = 1.2 V$

Figure 5.5) are set to  $30 fF$  and  $90 fF$ , respectively. The inductors are spirals with  $65 \mu m$  diameter, three turns, a nominal inductance of  $1.05 nH$  and a quality factor of 15 around the center frequency of 5.5 GHz. Finally, CMOS varactors with  $C_{max}/C_{min} = 334 fF/116 fF$  were employed within oscillator's tank to allow for frequency tuning.

For phase shift measurements, buffered signals from nodes 1C and 2C of the two oscillators (See Figure 5.11) were applied to the input terminals of Keysight's 86100D Infiniium DCA-X sampling oscilloscope. The sampling oscilloscope is capable of automatic phase shift measurements between the two signals and the relative displacement of the waveforms can also be visually seen on its screen as shown in Figure 5.12. The buffered signal from stage 2A in the second oscillator was used to provide the synchronized triggering signal that is needed for proper operation of the sampling oscilloscope. The remaining signals from the two oscillators were similarly connected to  $50 \Omega$  terminations to minimize loading mismatches between different stages of the oscillators.

An interesting prediction of the nonlinear dynamic theory presented in section

5.4 is that according to (5.11), if all the coupling channels are active at the same time and with the same strength, then the effective coupling strength becomes zero and the two oscillators get decoupled.! We were able to verify this prediction experimentally and observed that when we raised all the coupling gate voltages to  $1.2V$ , frequency locking disappeared and the sampling oscilloscope was no longer able to reconstruct and display the first oscillator's waveform. This is simply because the triggering signal (which came from stage A of the second oscillator) was no longer synchronous with the input signal (coming from stage C of the first oscillator) due to the effective lack of coupling. Alternatively, spectral peaks associated with beat frequencies were observed in the spectrum analyzer which again suggests that frequency locking had ceased to exist and all that could be observed was frequency pulling effects of two oscillators in close proximity. [13]

The frequency of APO is tunable from 4.9 GHz to 5.65 GHz and Figure 5.13 shows the measured phase shift patterns at these lower and upper frequency bounds. Compared to simulation results in Figure 5.10, the measured phase shift

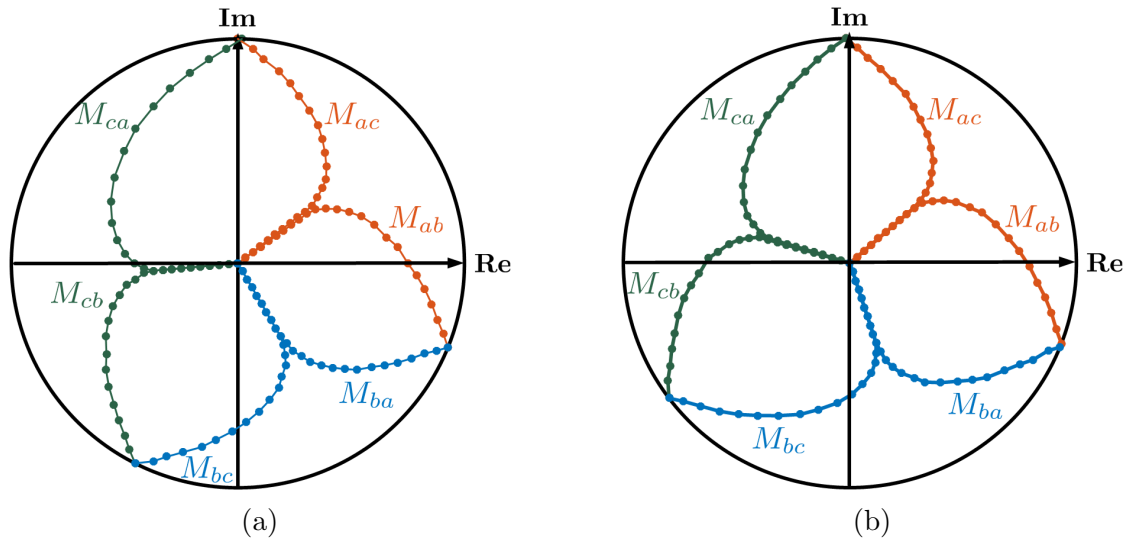
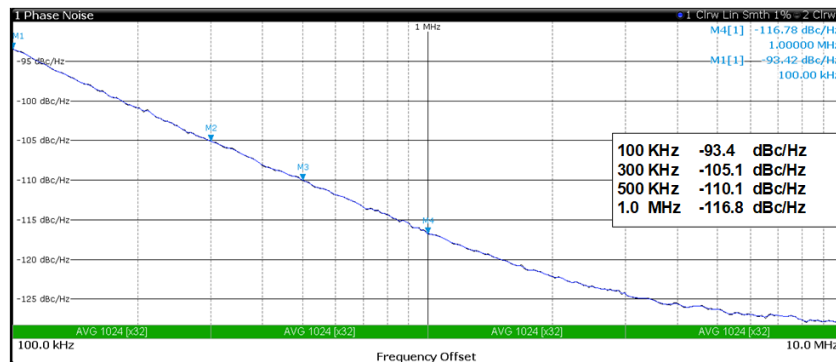


Figure 5.13: Measured phase shift patterns of the prototype APO. (a)  $f_0 = 4.90$  GHz and (b)  $f_0 = 5.65$  GHz

patterns in Figure 5.13 have about  $40^\circ$  offset rotation. This extra phase shift is partly due to slight mismatches in wirebond and cable lengths that connect the two output signal pads to the oscilloscope terminals and partly due to the inevitable mismatch in the free running frequency of the two oscillators before locking. The symmetry of “closed loops” in Figure 5.13, for example the one enclosed by the  $M_{ac}$  and  $M_{ca}$  curves, is distorted probably because of mismatch in the threshold voltage of the transistors in different coupling channels. The measurement results confirms that our APO prototype is capable of generating continuous, arbitrary phase shifts over its entire operation bandwidth. However, the generated phase shifts are not completely frequency independent as theory and simulations had predicted.



(a)



(b)

Figure 5.14: Measured phase noise of the prototype APO at (a)  $f_0 = 4.90$  GHz and (b)  $f_0 = 5.65$  GHz

The phase noise measurement of the APO oscillator is shown in Figure 5.14 and reads  $-116.8$  dBc/Hz and  $-115.6$  dBc/Hz at 1 MHz offset for the center frequencies of 4.90 and 5.65 GHz, respectively. The APO core, excluding the output buffers, draws 11 mA current from a 0.7 V power supply which corresponds to FOM of about 182 dB at 1 MHz offset frequency.

The APO phase noise is worse than that of single phase oscillators which is partly due to presence of noisy, active coupling devices between the two oscillators. However, the more important reason is that the transistors in the three stage ring oscillator topology are far away from their ideal operation conditions for maximum power efficiency. In fact it has been shown in [41, 42] that there is an optimum phase shift between gate and drain voltages of the transistor,  $\phi_{opt}$ , for maximum power efficiency which typically is around  $180^\circ$  at RF frequencies and then gradually decreases to the vicinity of  $120^\circ$  at  $f_{max}$  of the transistors. Table 5.1 shows the comparison between the implemented APO and a few state-of-the-art quadrature/multiphase oscillators. the APO is the first implementation that is capable of generating any arbitrary phase shift between the two coupled oscillators. This means the APO can be used to calibrate any systematic phase error in quadrature/multi-phase oscillators.

Table 5.1: Table of Comparison

Ref.	Frequency (GHz)	Tuning Range (%)	CMOS Technology	Inductor Q Factor	Supply Voltage (V)	DC Power (mW)	Phase Noise @ 1MHz (dBc/Hz)	Available Phases	FoM	FoM <sub>T</sub>
[40]	3.65	57	65nm	N.A	0.6	10.4	-125	Quadrature	186	201
[43]	14	26	65nm	8	0.8	15	-110	Half-Quadrature	181	189
[44]	2	13	180nm	N.A	1.8	5	-126	Quadrature	185	187
[45]	5	5	65nm	20	0.35	2.1	-125	Quadrature	196	190
[46]	7.95	7.5	65nm	20	0.8	27.2	-119	Quadrature	183	180
<b>This Work</b>	<b>5.65</b>	<b>14</b>	<b>130nm</b>	<b>15</b>	<b>0.7</b>	<b>7.7</b>	<b>-115.6</b>	<b>Continuous</b>	<b>182</b>	<b>185</b>

CHAPTER 6  
ASSOCIATIVE MEMORY AND PATTERN RECOGNITION IN  
COUPLED OSCILLATOR NETWORKS

## 6.1 Introduction

Recently there has been a rise of interest in using coupled oscillators as non-Boolean processors [47, 23, 22, 48, 49, 50]. Non-Boolean processing refers to a set of computational tasks that are usually associated with the realm of artificial intelligence and machine learning such as pattern recognition and associative memory recall. What these computational problems have in common is the inefficiency, if not impossibility, of developing algorithms based solely on combinational (Boolean) logic for their solutions.

Networks of weakly coupled oscillators are special cases of Hopfield networks and as such may be used in building physical systems capable of associative memory recall and pattern recognition. However, the existing architectures are not suitable for hardware implementation mainly due to the complexity of required couplings between the oscillators. In this chapter, we first review the associative memory properties of weakly coupled oscillators and then propose an alternative way of using coupled oscillators in what we call “discriminant circuits” in analogy to the concept of “discriminant functions” in the field of artificial intelligence and machine learning. The main advantage of our system is in the simplicity of its architecture which relies only on local couplings between adjacent oscillators. Using this architecture, we design a network of coupled CMOS oscillators as the core of a physical non-Boolean pattern recognition engine. The simplicity of the proposed circuit makes it readily implementable on any standard CMOS technology.

## 6.2 Associative memory properties of coupled oscillator networks

Nonlinear dynamic systems with *fixed-point attractors* [51] are natural candidates for realizing associative memories [52, 53, 54]. The state variable of such systems automatically converges to the fixed point attractor whose *basin of attraction* [51] includes the initial state from which the system is released at  $t = 0$ . This is an interesting feature for pattern recognition applications as it means that the system is able to reconstruct a stored image from a noisy or otherwise distorted version of the image itself and hence performs what is called an “**auto-associative**” recall [52, 53, 54]. In other words, the fixed point attractors can be viewed as stored patterns inside the system, while the initial states serve as *clues* that are used for their associative recall.

Interestingly, symmetric networks of weakly coupled oscillators are examples of

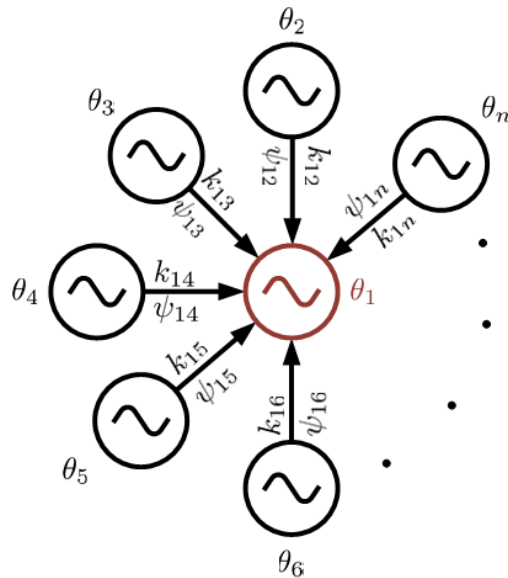


Figure 6.1: The coupling coefficients in the Kuramoto model, specifically all connections to oscillator 1.

such nonlinear systems. The dynamics of these systems are well approximated by the phase-reduced Kuramoto model [26, 29, 28] which states that the rate of change in the phase variable of the  $i^{th}$  oscillator,  $\theta_i$ , is given by:

$$\dot{\theta}_i = \sum_j k_{ij} \sin(\theta_j - \theta_i + \psi_{ij}) \quad (6.1)$$

As shown in Figure 6.1,  $k_{ij}$  shows the normalized strength of coupling from the  $j^{th}$  to the  $i^{th}$  oscillator and  $\psi_{ij}$  is the inherent phase shift of this coupling. Furthermore, if the couplings are “symmetric” [19] so that  $k_{ii} = 0$  and:

$$k_{ij} = k_{ji} \quad , \quad \psi_{ij} = -\psi_{ji} \quad (i \neq j)$$

then the dynamic system described by (6.1) has a Lyapunov [51] function given by [19]:

$$E = -\frac{1}{2} \sum_i \sum_j k_{ij} \cos(\theta_j - \theta_i + \psi_{ij})$$

The existence of Lyapunov function guarantees that the dynamic system described by (6.1) can only have fixed point attractors.

### 6.2.1 Network training and the Hebbian learning rule

The next essential step is to develop a *training* algorithm that would make arbitrary phase patterns become steady state solutions of (6.1). The steady state condition implies:

$$\begin{aligned} \sum_j k_{ij} \sin(\theta_j - \theta_i + \psi_{ij}) &= 0 \quad \Rightarrow \\ \sum_j k_{ij} [e^{i(\theta_j - \theta_i + \psi_{ij})} - e^{-i(\theta_j - \theta_i + \psi_{ij})}] &= 0 \quad \Rightarrow \\ e^{-i\theta_i} \sum_j k_{ij} e^{i\psi_{ij}} e^{i\theta_j} &= e^{i\theta_i} \sum_j k_{ij} e^{-i\psi_{ij}} e^{-i\theta_j} \end{aligned}$$

The left and right hand sides of the last equation are complex conjugates of each other and hence need to be purely real to be equal:

$$\sum_j k_{ij} e^{i\psi_{ij}} e^{i\theta_j} = \lambda_i e^{i\theta_i} \quad , \quad \lambda_i \in \mathbb{R} \quad (6.2)$$

If we let  $\lambda_1 = \lambda_2 = \dots = \lambda_n = \lambda$  and define  $\mathbf{C}_{ij} = k_{ij} e^{i\psi_{ij}}$  and  $\boldsymbol{\xi}_j = e^{i\theta_j}$  then (6.2) corresponds to an eigenvalue problem :

$$\mathbf{C}\boldsymbol{\xi} = \lambda\boldsymbol{\xi} \quad (6.3)$$

where as opposed to a standard eigenvalue problem, in (6.3) the objective is to find the right matrix  $\mathbf{C}$  such that  $\boldsymbol{\xi}$  becomes its eigenvector. The above argument can be generalized to store multiple patterns,  $\boldsymbol{\xi}^{(1)} \dots \boldsymbol{\xi}^{(m)}$ . If we store each  $\boldsymbol{\xi}^{(k)}$  by making it an eigenvector of  $\mathbf{C}$  for the same eigenvalue of  $\lambda$  then we should have:

$$\mathbf{C}\mathbf{P} = \lambda\mathbf{P} \quad (6.4)$$

where  $\mathbf{P}$  is the matrix of stored patterns whose  $k^{th}$  column is equal to  $\boldsymbol{\xi}^{(k)}$ . The general solution to (6.4) is given by: [55]

$$\mathbf{C} = \lambda\mathbf{P}\mathbf{P}^\dagger + (\mathbf{I} - \mathbf{P}^\dagger\mathbf{P})\mathbf{B} \quad (6.5)$$

where  $\mathbf{P}^\dagger$  shows the **Moore-Penrose** pseudo-inverse of  $\mathbf{P}$ ,  $\mathbf{I}$  is the unity matrix and  $\mathbf{B}$  can be any arbitrary matrix. [56] To get a simple training formula, we assume that the patterns to be stored are orthonormal so that  $\mathbf{P}^\dagger = \mathbf{P}^*$  where  $\mathbf{P}^*$  denotes the conjugate transpose of  $\mathbf{P}$ . Furthermore, we let  $\lambda = 1$  and  $\mathbf{B} = \mathbf{0}$  in (6.5) for simplicity and get :

$$\mathbf{C} = \mathbf{P}\mathbf{P}^* \Rightarrow \mathbf{C}_{ij} = \sum_{k=1}^m \boldsymbol{\xi}_i^{(k)} \overline{\boldsymbol{\xi}_j^{(k)}} \quad (6.6)$$

which is the well known **Hebbian learning rule** [19, 55]. The above derivation of Hebbian learning rule only guarantees that  $\boldsymbol{\xi}^{(1)} \dots \boldsymbol{\xi}^{(m)}$  correspond to fixed points

of the coupled oscillator network dynamics without analyzing their stability. As more fixed points are stored, an important theoretical question is whether or not these steady states lose their stability, potentially limiting the storage capacity in these networks.

### **6.3 An alternative to associative memory networks: The discriminant function approach**

In the last section, we showed that theoretically, networks of coupled oscillators can be trained to perform regenerative, associative memory recall. However, there remains a few important obstacles in going from the elegant theory to a practical realization of such associative memory networks. One of the main problems lies in providing the large number of trainable couplings required between the oscillators. In fact it is not difficult to see from the Hebbian learning rule (6.6) that in general, an associative network of  $n$  oscillators requires  $\mathcal{O}(n^2)$  programmable connections between oscillators. [18, 57] Clearly, making a fully connected network of physical oscillators become prohibitively difficult except for moderately sized networks with limited processing capabilities. Hoppensteadt and Izhikevich [18] proposed an elegant way of bypassing the connectivity problem in networks of coupled oscillators. In their approach, there are no direct connections between the oscillators and instead they are all coupled through a shared medium. The shared medium however, needs to be excited by a carefully constructed signal so that the final mathematical equations governing the dynamics of oscillators are identical to that of the fully connected network with coupling coefficients given by (6.6). This approach does not fully solve the connectivity problem and instead trades it with another, per-

haps equally hard, problem of generating the required global signal that excites the shared medium [18]. Also the network design becomes complicated for larger  $n$ , making it difficult to realize large networks of coupled oscillators [18]. In fact, a physical implementation of this idea as reported in [20] is limited to a network of 8 oscillators and also requires an off-chip signal generator for exciting the shared medium.

Furthermore, even a fully connected network of coupled oscillators suffers from an important problem of **spurious pattern storage**. In order to see this, notice from the derivation of the Hebbian learning rule that if  $\boldsymbol{\xi}^{(1)} \dots \boldsymbol{\xi}^{(m)}$  all satisfy (6.3), then any linear combination of them also corresponds to an eigenvector of  $\mathbf{C}$  with the same eigenvalue of  $\lambda$  and hence is another fixed point of the system. Therefore, the spurious pattern storage is a natural consequence of the Hebbian learning rule for training coupled oscillator networks. Clearly, the number of stored spurious patterns quickly increases with the number of desired stored patterns and make the system more likely to converge to one of the unrecognizable spurious patterns in response to an input clue which imposes additional limitations on the storage capacity of these networks. [53, 57]

Alternatively, an effective and widely adopted approach for solving a variety of pattern recognition problems is to use “discriminant functions” or more generally “artificial neural networks” (ANN) [52, 58, 59]. The basic idea of discriminant function approach is to start with a function with some free parameters and then tune these parameters so that the function’s output mainly depends on the particular *class* to which the input belongs. As an example, suppose we want to distinguish between input patterns belonging to two classes,  $\Omega_1, \Omega_2$ , using a discriminant function approach. We show the discriminant function by  $f(\mathbf{x}, \boldsymbol{\eta})$  where  $\boldsymbol{\eta}$  is a vector of the free parameters of the function and  $\mathbf{x}$  is the function’s input.

To make  $f(\mathbf{x}, \boldsymbol{\eta})$  a good discriminant function, one possibility is to look for a vector  $\boldsymbol{\eta}$  such that:

$$\begin{aligned} f(\mathbf{x}, \boldsymbol{\eta}) &> 0 & \text{if } \mathbf{x} \in \Omega_1 \\ f(\mathbf{x}, \boldsymbol{\eta}) &< 0 & \text{if } \mathbf{x} \in \Omega_2 \end{aligned}$$

The process of finding vector  $\boldsymbol{\eta}$  in above is naturally called the “training phase”. After training is complete, we can reliably use  $f(\mathbf{x}, \boldsymbol{\eta})$  as a discriminant function to classify input patterns to either class  $\Omega_1$  or  $\Omega_2$  by only looking at the sign of  $f(\mathbf{x}, \boldsymbol{\eta})$ .

Building upon the idea of discriminant functions, we propose to use the term “discriminant circuit” to describe any physical circuit with some free control parameters that can be used in pattern recognition applications. The control parameters of a discriminant circuit should similarly be tuned such that the circuit’s output depends mainly on some collective property of its input signals. The circuit’s output signal can then be used to distinguish different input patterns from each other.

While complex software algorithms, enjoying access to several layers of arbitrary discriminant functions, provide the greatest degree of flexibility, discriminant circuits would offer much faster processing speeds. Convergence to the final steady state in networks of coupled oscillators typically takes a few hundred oscillation cycles. Therefore, faster processing speeds are achieved if oscillators with higher free running frequencies are used in forming the network. It is also worth mentioning that while it is true that convergence to the steady state may take longer in longer chains of coupled oscillators, the average convergence time does not seem to get impractically long. In fact, our numerical simulations showed that in changing the length of an oscillator chain from 25 to 50 to 100, the median convergence time

increased from 93.75 to 112.3 and 128.8 (normalized time units) respectively. That is to say, the median convergence time seems to rise sub-linearly with the chain size.

We next study dynamics of *symmetrically* coupled oscillator chains and see how they could serve as discriminant circuits for pattern classification applications.

## 6.4 Dynamics of symmetrically coupled oscillators

### 6.4.1 The mathematical model

In this section, we study the nonlinear dynamics of two weakly coupled oscillators using the phase-reduced Kuramoto model. First, consider the case where a *symmetric* coupling channels exist between the oscillators as shown in Figure 6.2.

The Kuramoto model of this system gives:

$$\dot{\theta}_1 = k \sin(\theta_2 - \theta_1 - \psi) \quad (6.7)$$

$$\dot{\theta}_2 = k \sin(\theta_1 - \theta_2 + \psi) \quad (6.8)$$

where as shown in Fig. 6.2,  $\theta_1$  and  $\theta_2$  are the phase variables associated with the two oscillators and  $k$  and  $\psi$  show the strength and inherent phase shift of the

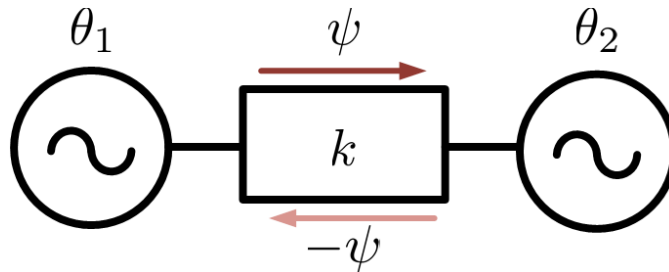


Figure 6.2: Unimodal, symmetric coupling of two oscillators

coupler, respectively. As a consequence of symmetric coupling assumption, the inherent phase shift term  $\psi$  appears in the first equation with a minus sign and in the second equation with a plus sign, consistent with the direction of coupling arrows in Figure 6.2. Next, consider the scenario shown in Figure 6.3 where we now assume that two symmetric coupling channels with strengths of  $a/2$  and  $b/2$  and inherent phase shifts of  $\psi_a$  and  $\psi_b$  respectively, exist between two oscillators. The Kuramoto model of this slightly more complicated system is:

$$\begin{aligned}\dot{\theta}_1 &= \frac{a}{2} \sin(\theta_2 - \theta_1 - \psi_a) + \frac{b}{2} \sin(\theta_2 - \theta_1 - \psi_b) \\ \dot{\theta}_2 &= \frac{a}{2} \sin(\theta_1 - \theta_2 + \psi_a) + \frac{b}{2} \sin(\theta_1 - \theta_2 + \psi_b)\end{aligned}$$

Consequently, the dynamics of the relative phase shift between the oscillators,  $\varphi = \theta_2 - \theta_1$ , is governed by:

$$\dot{\varphi} = a \sin(-\varphi + \psi_a) + b \sin(-\varphi + \psi_b) \quad (6.9)$$

We now proceed with the analysis of the dynamic system described by (6.9). First, notice that a Lyapunov function exists for this system which guarantees

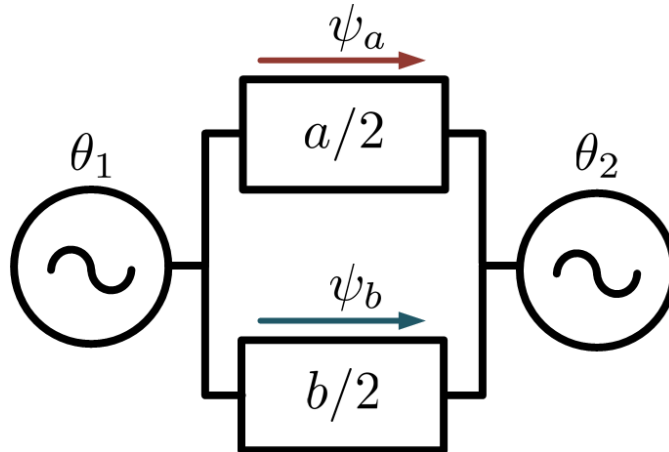


Figure 6.3: Bimodal, symmetric coupling of two oscillators

convergence to steady state :

$$E(\varphi) = -a \cos(-\varphi + \psi_a) - b \cos(-\varphi + \psi_b)$$

$$\Rightarrow$$

$$\dot{E} = -(\dot{\varphi})^2 \leq 0$$

A stable steady state solution of (6.9) necessarily corresponds to a local minima of  $E(\varphi)$ :

$$\frac{dE}{d\varphi} = 0 \quad \Rightarrow \quad \frac{d}{d\varphi} \{a \cos(-\varphi + \psi_a) + b \cos(-\varphi + \psi_b)\} = 0$$

$$\frac{d^2E}{d\varphi^2} > 0 \quad \Rightarrow \quad \frac{d^2}{d\varphi^2} \{a \cos(-\varphi + \psi_a) + b \cos(-\varphi + \psi_b)\} < 0$$

In order to get a final closed formula for  $\varphi$ , it is better to rewrite  $E(\varphi)$  using Euler's formula:

$$E(\varphi) = -\frac{a}{2} [e^{i(-\varphi+\psi_a)} + e^{i(\varphi-\psi_a)}] - \frac{b}{2} [e^{i(-\varphi+\psi_b)} + e^{i(\varphi-\psi_b)}]$$

Simple algebraic manipulation reveal that steady state condition,  $\frac{dE}{d\varphi} = 0$  , gives:

$$e^{i\varphi}(ae^{-i\psi_a} + be^{-i\psi_b}) = e^{-i\varphi}(ae^{i\psi_a} + be^{i\psi_b})$$

Since the left and right hand sides of the above equation are complex conjugates

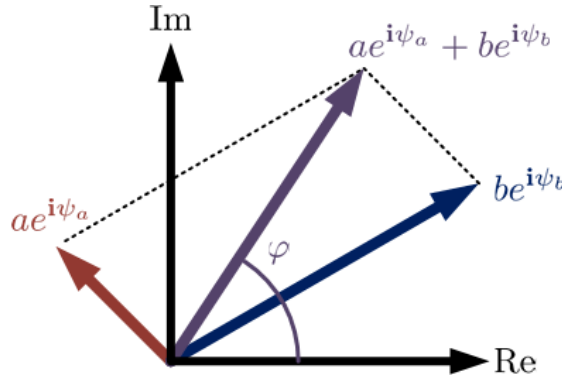


Figure 6.4: The vector superposition method for finding the steady state phase shift in the bimodal symmetric coupled oscillator system

of each other, they should be purely real to be equal, i.e,

$$e^{-i\varphi}(ae^{i\psi_a} + be^{i\psi_b}) \in \mathbb{R}.$$

There are only two possibilities for  $\varphi$  to satisfy this requirement:

$$\varphi = \begin{cases} \text{Arg}(ae^{i\psi_a} + be^{i\psi_b}) \pm 2n\pi \\ \text{Arg}(ae^{i\psi_a} + be^{i\psi_b}) \pm (2n + 1)\pi \end{cases}$$

On the other hand, the stability condition,  $\frac{d^2 E}{d\varphi^2} > 0$ , implies:

$$\frac{d^2 E}{d\varphi^2} > 0 \Rightarrow e^{i\varphi}(ae^{-i\psi_a} + be^{-i\psi_b}) > 0$$

Therefore, the stable steady state phase shift between the oscillators is :

$$\varphi = \text{Arg}(ae^{i\psi_a} + be^{i\psi_b}) \tag{6.10}$$

The above result has an interesting intuitive interpretation: if one considers the effect of each coupling channel in Figure 6.3 separately, it is easy to see that the top coupling pushes the relative phase shift between the two oscillators to  $\psi_a$  whereas the bottom coupler pulls it toward  $\psi_b$ . In the presence of both coupling channels, the final phase shift can be found from the weighted vector superposition shown in Figure 6.4.

## 6.4.2 Circuit implementation

It is not difficult to realize symmetric coupling channels between simple physical oscillators. In a three stage CMOS ring oscillator shown in Figure 6.5, adjacent inverter gate voltages naturally have a phase shift of  $2\pi/3$  with respect to each other and therefore depending on which points of two such oscillators are connected via a resistor, different coupling modes can be realized. For example, if only the middle

coupling in Figure 6.5, is active, then  $\theta_2 + 2\pi/3$  should eventually become equal to  $\theta_1$  to minimize the energy loss in the resistive connection between the two oscillators. This condition is then consistent with having  $\psi = 2\pi/3$  in (6.7). Similarly, one can argue that the leftmost and rightmost couplings shown in Figure 6.5 have inherent phase shifts of 0 and  $4\pi/3$  respectively.

The circuit level schematic of the coupled ring structure is shown in Figure 6.6. The three inverter gates in oscillators (1) and (2) are labeled as **1A** , **1B** , **1C** and **2A** , **2B** , **2C** respectively. The input terminals of the the two couplers in the middle are likewise labeled to imply connectivity to the respective oscillator terminals without drawing explicit wire connections. The couplers are CMOS transmission gates, which are essentially resistors that can be digitally switched on or off by their gate control voltages,  $S_1$  and  $S_2$ . Since conductance of transistors are to the first order proportional to their aspect ratios,  $(W/L)$ , a discrete set of coupling strengths can be realized for each coupling channel by laying out a bank of differently sized transmission gates on chip. The strength of each coupling channel can then be digitally controlled by activating the transmission gate with the desired size from this available set. The functionality of the circuit in Figure 6.6 has been

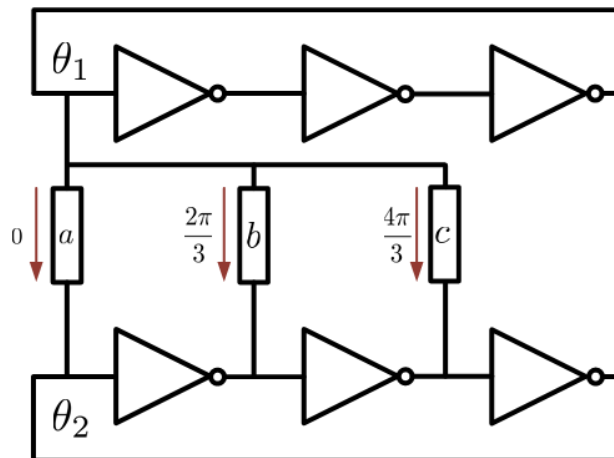


Figure 6.5: Different coupling channels of two CMOS ring oscillators

numerically verified using the accurate models of a standard 130nm CMOS process in Cadence Virtuoso. As can be seen from Figure 6.7, the simulated steady state phase shifts of oscillators agree very well with what equation (6.10) predicts.

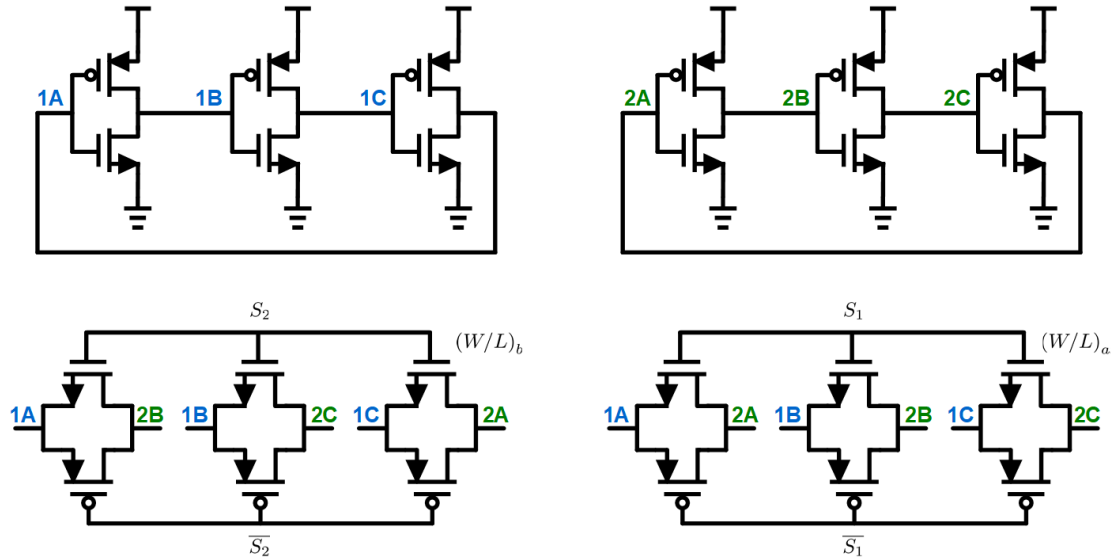


Figure 6.6: Circuit level schematic of CMOS coupled oscillators

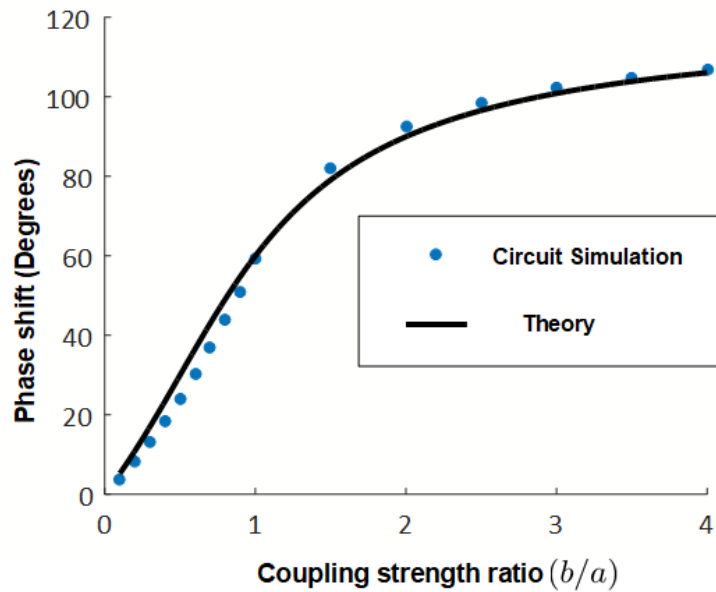


Figure 6.7: Agreement between equation (6.10) and simulation results

## 6.5 Pattern recognition with coupled oscillator chains

### 6.5.1 System Description

In this section, we generalize the case of two coupled oscillators to a chain of coupled oscillators and show how this structure can be used as a "discriminant circuit" in the sense we explained in section 6.3.

Figure 6.8 shows a folded chain of 16 ring oscillators where two types of tunable couplers, "**input**" and "**training**" couplers, are available in each link. The system response is defined as the phase shift between the oscillators at the two ends of the chain which is shown by  $\varphi$ . In a simply connected chain of  $N$  oscillators, there are exactly  $l = N - 1$  links and therefore  $l$  different instances of "input" and "training" couplers each. For a practical implementation, it is best to fold the chain into a rectangular configuration similar to what is shown in Figure 6.8 to make the actual layout as compact as possible. The input couplers have zero inherent phase shift and their strengths,  $a_k$ , are determined by a given 2D input pattern. The training couplers on the other hand, have an inherent phase shift of  $2\pi/3$  and their relative strengths,  $b_k$ , will be determined in the training phase. In other words, vectors  $\mathbf{a} = [a_1 \dots a_k]^T$  and  $\mathbf{b} = [b_1 \dots b_l]^T$  are analogous to vectors  $\mathbf{x}$  and  $\boldsymbol{\eta}$  in the discriminant function  $f(\boldsymbol{\eta}, \mathbf{x})$  formulation introduced in section 6.3. The details of determining the  $a_k$  parameters from the input pattern and the  $b_k$  parameters in the training phase will be provided in the appendix at the end of this section.

Intuitively, we expect that since there are no closed loops in the folded chain

structure, the phase shifts in each link can be independently set to:

$$\varphi_k = \text{Arg}(a_k + b_k e^{i2\pi/3})$$

so as to minimize the total Lyapunov energy of the chain. Consequently, a simple formula for the circuit output,  $\varphi$ , as a function of the circuit coupling parameters exists:

$$\varphi = \sum_{k=1}^l \text{Arg}(a_k + b_k e^{i2\pi/3}) \quad (6.11)$$

If we had closed-loops in the network, a constrained minimization using Lagrange multipliers would be necessary to ensure that sum of phase shifts around each loop

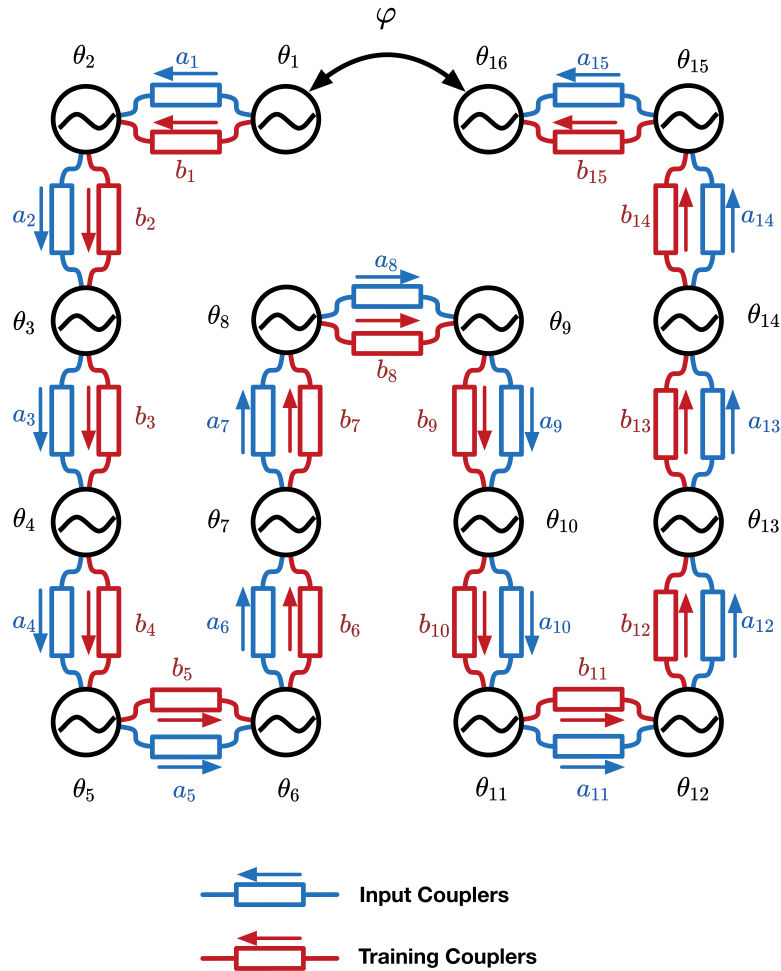


Figure 6.8: Folded chain of coupled oscillators as a discriminant circuit

would add up to some multiple of  $2\pi$  and (6.11) would not necessarily be valid. We postpone a more formal derivation of (6.11) to the appendix section.

### 6.5.2 An example: Classification of alphabet letters

It is perhaps best to explain the circuit's operation with the aid of an example: Suppose we want to train a coupled oscillator chain network to distinguish some alphabet letters irrespective of their orientation. To be more specific, imagine that we want to classify the 32, 20x20 pixel images of four alphabet letters shown in Figure 6.9. As explained before, the input coupler strengths,  $a_k$ , are dictated by the input image. That is, we assign each  $a_k$  to one pixel in the input image and set its (normalized) value to a minimum of say, 0.1, if the corresponding pixel is a logical zero or a maximum of 1 if the corresponding pixel is a logical one. Although we are assuming that the input pattern is a binary image for simplicity in this example, this is not essential to the circuit's operation and in general  $a_k$  parameters can assume gray-scale values. Our objective in the training phase is to find a good choice of training coupler strengths,  $b_k$ , that would result in a discriminatory response of the circuit. For example, a good discriminatory response is when  $\varphi$  is concentrated around  $0, 90^\circ, 180^\circ, 270^\circ$  for the given samples

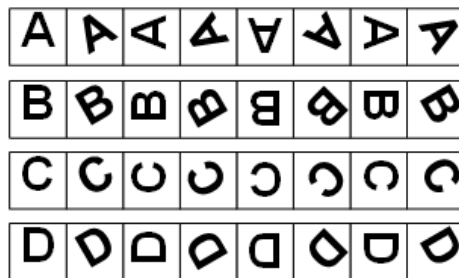


Figure 6.9: Alphabet letter images used for network training

of **A**, **B**, **C**, **D** respectively. A practical training algorithm should also be limited to a finite choice of  $b_k$  parameters from some available set of coupling strengths. we may thus define *training resolution* as the total number of bits allowed in specifying  $b_k$  parameters.

The system response to each input can be visually represented by placing a dot at an angle of  $\varphi$  on a unity circle where  $\varphi$  is calculated by (6.11). This visual representation is used in Figure 6.10 to show constant improvement in the discriminatory behavior of the circuit with finer resolutions allowed in the training. It should be noted that the above example is just meant to illustrate the operation of coupled oscillator chain as a *discriminant circuit* and should not be considered

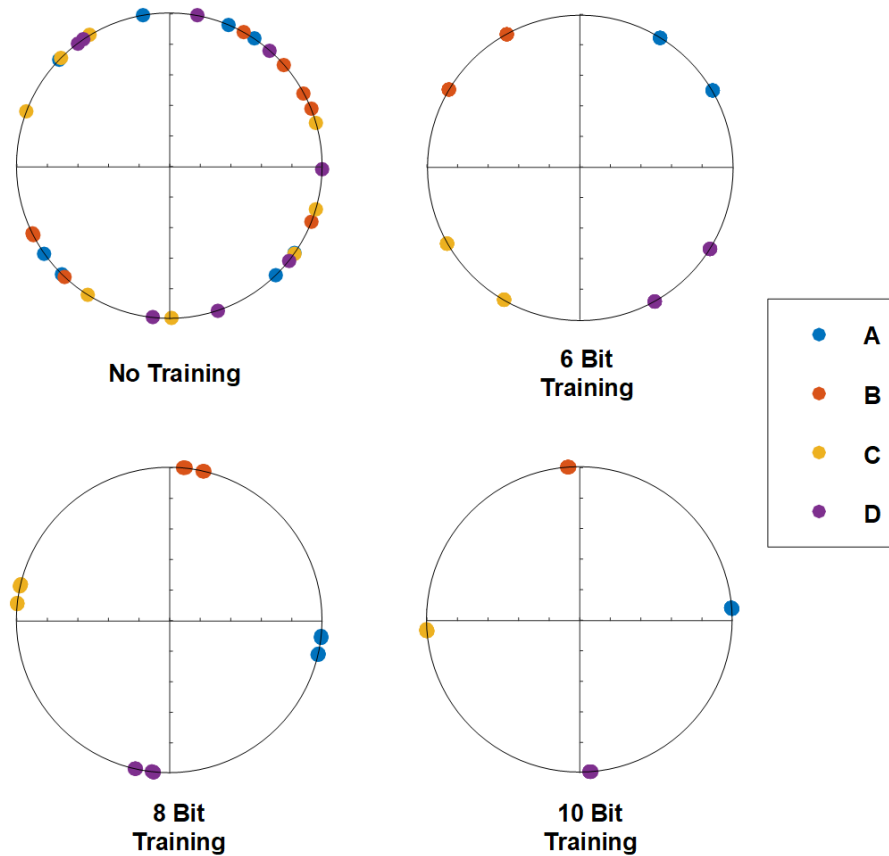


Figure 6.10: Effect of training on separation between different alphabet letter images

a complete pattern recognition system in itself. In particular, since there is no “pre-processing” or ”feature extraction” steps involved, the system is prone to the infamous **curse of dimensionality** problem [58, 59]. In other words, the network parameters may currently be over fitted to give perfect outputs for the given samples in the training set but that makes the system more vulnerable to noise and random distortions and degrades its ability to perform useful generalizations.

While it is certainly more convenient to have only one discriminant circuit that classifies several different objects, it is more practical to have a network of discriminant circuits where each circuit is specially trained in recognizing just one particular object. A collaborative network of such specialized, discriminant circuits would then become a more powerful pattern recognition engine. It should be noted however, that different discriminant circuits do not necessarily need to correspond to different physical instances on a chip. A single discriminant circuit can be sequentially loaded with the right training parameters developed for different objects to determine their presence in a given image.

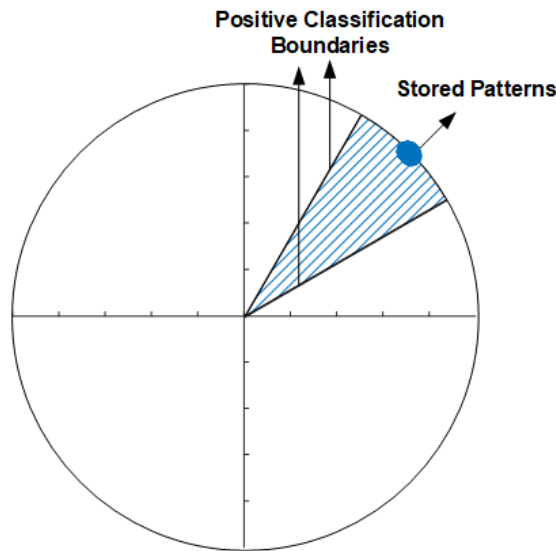


Figure 6.11: Output response of a successfully trained network

This strategy not only increases the total number of samples of each object that the system would be able to recognize after training, but also has the added benefit of simplifying design of the sub-system needed to interpret different values of  $\varphi$  for either positive or negative classifications. This is so because a simple “phase frequency detector” (PFD) which is widely used in standard “phase locked loops” (PLL) [60, 61] designs can be integrated with the circuit to determine whether  $\varphi$  is within some designated range or not. The output of the PFD block determines whether the circuit “**recognizes**” or “**rejects**” a pattern given to it for classification. As shown in Figure 6.11, a network training is considered successful if it is able to find a set of  $b_k$  parameters that results in  $\varphi$  to be within the designated range for all the samples used in the training.

### 6.5.3 Reducing chance of false/ambiguous classifications

So far, the general procedure for using chains of coupled oscillators in pattern classification can be summarized as follows:

Let us show the object <sup>1</sup> we want the circuit to recognize by  $\xi$  and assume that several labeled examples of  $\xi$ , which we show by  $\xi^{(1)} \dots \xi^{(m)}$ , are given that can be used in “training”. We pick a target value for the circuit’s output signal,  $\varphi = \varphi_0$ , load the network’s  $a_k$  parameters with each of the patterns  $\xi^{(1)} \dots \xi^{(m)}$  and try to find a single set of  $b_k$  parameters that would result in the circuit producing an output in the vicinity of  $\varphi_0$  for every  $\xi^{(1)} \dots \xi^{(m)}$ . We store the above set of  $b_k$  parameters in some library as the “training template” for  $\xi$  and call it  $b^\xi$  for future reference. Later when an unidentified image,  $\chi$ , is presented to the system by

---

<sup>1</sup>By “object”, we mean some abstract concept, like “letter A” or “Cat”, that carries some meaning. By “example / sample”, we mean actual images associated with such concepts, like the image of a letter “A” or a picture of a cat

loading the corresponding values of  $a_k$  parameters, we use the set  $b^\xi$  from before and see if  $\varphi$  happens to fall into the vicinity of  $\varphi_0$ . That is, we now have a testing method which we may call the “**recognize/reject**” test for pattern  $\xi$ . If the result of the “recognize/reject” test is positive, then  $\chi$  is identified as another instance of  $\xi$ . Otherwise  $\chi$  is considered to be an object different than  $\xi$  and consequently the next training template in the library is used to seek a match.

There still remains a couple of issues with our structure that need to be addressed at this point. These are what we may call the problems of “**false**” and “**ambiguous**” classifications and are analogous to the problem of spurious storage in Hopfield networks. False classification happens when a pattern not similar to  $\xi^{(1)} \dots \xi^{(m)}$  is labeled as another example of  $\xi$ . This is possible to happen because  $b^\xi$  was developed during the training phase to make sure that when input image happens to be any one of  $\xi^{(1)} \dots \xi^{(m)}$ , then  $\varphi \approx \varphi_0$  without necessarily preventing other, perhaps unrelated, images to result in producing the same values of  $\varphi$ .

Ambiguous classification is a consequence of false classification problem and happens when an input image,  $\chi$ , can be classified as an instance of more than on

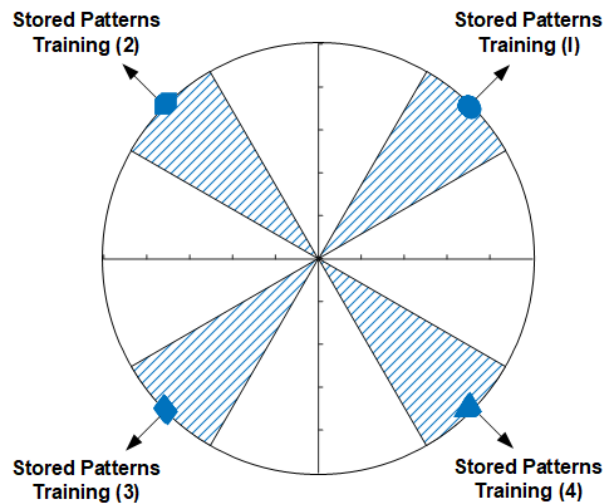


Figure 6.12: Developing several training templates using different target angles

object, say both  $\xi$  and  $\lambda$ , because with both  $b^\xi$  and  $b^\lambda$ , the circuit output,  $\varphi$ , falls into the vicinity of  $\varphi_0$ .

Fortunately, there is an easy fix to the problem of false classification in our system. As illustrated in Figure 6.12, the solution is to find multiple, independent training templates,  $b_{(1)}^\xi, b_{(2)}^\xi, \dots$ , for different target values of  $\varphi_0$ , say  $\varphi_0^{(1)}, \varphi_0^{(2)}, \dots$  and require passing several “recognize/reject” tests using these templates before an object is positively classified as  $\xi$ .

Numerical simulations confirm (See Figure 6.13) that chances of false classification decreases rapidly (the fitted curve is an exponential) as more training templates are developed and consequently more recognize/reject tests are used for any positive classification.

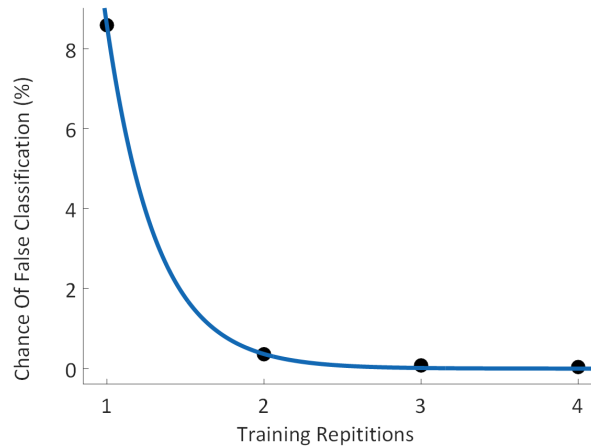


Figure 6.13: Chance of false classification v.s number of recognize/reject tests

#### 6.5.4 Storage capacity

As a final note, we investigate the storage capacity of a discriminant circuit which can be defined as the maximum number of samples of a single object for which the

network can be successfully trained. (See Figure 6.11) In a realistic application, different sample images used in training the network for identification of a particular object may be highly correlated with each other which should make it easier to find a single training template that gives the desired circuit output for all of them. In quantifying the storage capacity of our network however, we assume a more pessimistic situation where sample images used for training are totally uncorrelated to see if the network can still be successfully trained. While leaving the details of our training algorithm and the implemented MATLAB codes for the appendix section, the results of our numerical experiments is presented in Figure 6.14 and can be summarized as follows:

For a fixed size of the network ( $N$ ), an increasing number of  $m$  uncorrelated patterns are allowed in training. The x-axis shows the ratio  $x = m/N$ . The y-axis is the “success” rate in training the network for different values of  $N$  and  $m$ . The target value of  $\varphi_0$  is arbitrarily set to  $\pi/4$  in these experiments and an experiment is called successful if for all the  $\xi^{(1)} \dots \xi^{(m)}$  patterns we have  $|\varphi - \varphi_0| \leq \pi/8$ . A total of 1000 numerical experiments were carried on for each pair of  $m$  and  $N$ . Interestingly, our MATLAB simulation results indicate that the reliable storage capacity of network, which can be defined as the maximum value of  $x$  for which the training success rate is close to 1, increases with the network size and is more than 0.25 for  $N = 64$ .

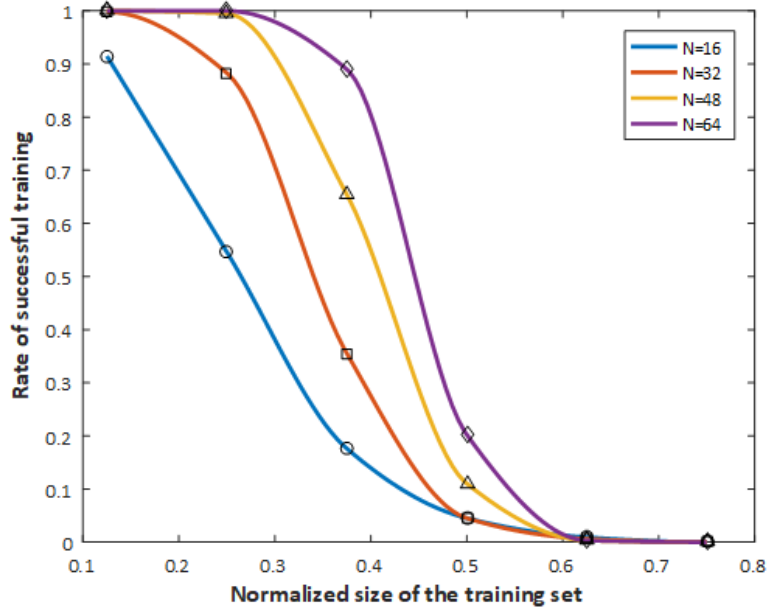


Figure 6.14: Rate of successful training v.s relative size of training set

## 6.6 Appendix

### 6.6.1 Analysis of the Kuramoto model for coupled oscillator chains

In this section, we generalize the dynamic analysis of two coupled oscillators to a chain of coupled oscillators in order to validate equation (6.11). Figure 6.8 shows a typical chain of coupled oscillators where in each link there are two types of couplers. Notice that the direction of arrow on the couplers dictates how the inherent phase shift terms should be inserted into the Kuramoto equation for each oscillator. For example, the reference direction in the first link is from oscillator (1) to (2) which means that this link results in the following terms to appear in

the Kuramoto equations of the the first and second oscillators:

$$\dot{\theta}_1 = a_1 \sin(\theta_2 - \theta_1 - \psi_1^a) + b_1 \sin(\theta_2 - \theta_1 - \psi_1^b) + \dots$$

$$\dot{\theta}_2 = a_1 \sin(\theta_1 - \theta_2 + \psi_1^a) + b_1 \sin(\theta_1 - \theta_2 + \psi_1^b) + \dots$$

Also the relative phase shift between the oscillators of the first link,  $\varphi_1$ , is defined as:

$$\varphi_1 := \theta_2 - \theta_1$$

It should also be obvious that in an  $n \times n$  folded chain of coupled oscillators, there are exactly  $l = n^2 - 1$  coupler links. The Kuramoto equation for each oscillator can be written in a general form of:

$$\dot{\theta}_i = \sum_{j=1}^{n^2} a_{ij} \sin(\theta_j - \theta_i + \psi_{ij}^a) + \sum_{j=1}^{n^2} b_{ij} \sin(\theta_j - \theta_i + \psi_{ij}^b)$$

where  $a_{ij}$  and  $b_{ij}$  terms are zeros unless  $\theta_i$  and  $\theta_j$  are across some link, say link  $k$ , in the chain in which case we have:

$$a_{ij} = a_{ji} \triangleq a_k \quad (i = j + 1)$$

$$b_{ij} = b_{ji} \triangleq b_k \quad (i = j + 1)$$

$$\psi_{ij}^a = -\psi_{ji}^a \triangleq \psi_k^a \quad (i = j + 1)$$

$$\psi_{ij}^b = -\psi_{ji}^b \triangleq \psi_k^b \quad (i = j + 1)$$

$$\varphi_k \triangleq \theta_i - \theta_j \quad (i = j + 1)$$

It is not difficult to see that this system has a Lyapunov function in the form of:

$$E = -\frac{1}{2} \sum_i \sum_j a_{ij} \cos(\theta_j - \theta_i + \psi_{ij}^a) - \frac{1}{2} \sum_i \sum_j b_{ij} \cos(\theta_j - \theta_i + \psi_{ij}^b)$$

The above equation can be rewritten in terms of the relative phase shifts in each link,  $\varphi_1 \cdots \varphi_l$ , instead of oscillator absolute phase variables,  $\theta_1 \cdots \theta_n$ , as:

$$E = -\sum_{k=1}^l a_k \cos(-\varphi_k + \psi_k^a) - \sum_{k=1}^l b_k \cos(-\varphi_k + \psi_k^b)$$

where  $l$  shows the total number of links in the chain. Since there are no closed loops in the chain, variables  $\varphi_1 \dots \varphi_l$  are independent of each other and thus the minimum of the energy function happens when  $\frac{\partial E}{\partial \varphi_m} = 0$  and  $\frac{\partial^2 E}{\partial \varphi_m^2} > 0$  for  $m = 1 \dots l$  so that the Hessian matrix becomes positive definite. The two sets of equations resulting from these conditions are:

$$\begin{aligned} \frac{d}{d\varphi_m} \{a_m \cos(-\varphi_m + \psi_m^a) + b_m \cos(-\varphi_m + \psi_m^b)\} &= 0 \\ \frac{d^2}{d\varphi_m^2} \{a_m \cos(-\varphi_m + \psi_m^a) + b_m \cos(-\varphi_m + \psi_m^b)\} &< 0 \end{aligned}$$

However, these equations have exactly the same form as what was previously analyzed for the case of two coupled oscillators. Hence, the relative phase shifts in each link of the chain are given by:

$$\varphi_m = \text{Arg}(a_m e^{i\psi_m^a} + b_m e^{i\psi_m^b}) \quad (6.12)$$

In our proposed chain of coupled oscillators we have  $\psi_m^a = 0$  and  $\psi_m^b = 2\pi/3$  and as such:

$$\varphi = \sum_{k=1}^l \text{Arg}(a_k + b_k e^{i2\pi/3}) \quad (6.13)$$

The above derivation made crucial use of there being no loops present in the structure. Otherwise, a constrained minimization using Lagrange multipliers would be necessary to find the relative phase shifts and ensure they add to  $2\pi$  around each closed loop and (6.12) would not be valid in general.

## 6.6.2 Determining input coupler Strengths from 2D input images

In this section, we briefly explain the process of determining "input coupler" strength parameters from 2D input images. Here we explain the mapping process

for binary, black and white images for simplicity. It is however easy to generalize the procedure to allow 2D gray-scale images as well.

Let us assume that we have a set of two dimensional, binary,  $n \times m$ , images that we want to classify with our coupled oscillator chain. In order to do so, we first build a chain of coupled oscillator (possibly one with a folded structure as explained before) with  $l$  links such that  $l + 1 = nm$ . Each 2D input image is essentially an  $n \times m$  matrix,  $\mathbf{X}$ , which can easily be reshaped into a unique, binary  $l \times 1$  vector,  $\mathbf{x}$ , as follows:

Starting from  $\mathbf{x}_1$ , we define it to be equal to 1 if  $\mathbf{X}_{21} = \mathbf{X}_{11}$  and 0 otherwise. We similarly compare  $\mathbf{X}_{31}$  with  $\mathbf{X}_{11}$  to define  $\mathbf{x}_2$  and continue this procedure to the end of the first column where comparing  $\mathbf{X}_{n1}$  with  $\mathbf{X}_{11}$  determines the value of  $\mathbf{x}_{n-1}$ . Next, we go to the beginning of the second column and determine  $\mathbf{x}_n$  by comparing  $\mathbf{X}_{12}$  with  $\mathbf{X}_{11}$  after which we continue the process for the entire second column. Since there are  $m$  column in  $\mathbf{X}$ , this procedure needs to be repeated  $m$  times in order to fully construct vector  $\mathbf{x}$  whose length would exactly be equal to  $l = mn - 1$ . The elements of  $\mathbf{x}$  are then used to set the corresponding "input coupler" strength parameters of the circuit.

It is worth mentioning that the above process maps every  $n \times m$  binary image into a unique vector of length  $nm - 1$  and further guarantees two input patterns which are exactly the "negative images" of each other are mapped to the same vector  $\mathbf{x}$  :

$$\mathbf{X} \rightarrow \mathbf{x} \iff \tilde{\mathbf{X}} \rightarrow \mathbf{x}$$

which is a desirable trait in most pattern recognition applications.

### 6.6.3 Details of the training algorithm

A more detailed discussion of the training algorithm for the proposed chain of coupled oscillator structure is presented in this section.

Let us recall that we are assuming  $m$  patterns,  $\xi^{(1)} \dots \xi^{(m)}$ , are given and we want to tune the circuit parameters such that a specific target value of  $\varphi = \varphi_0$  is measured at the circuit's output whenever one of  $\xi^{(1)} \dots \xi^{(m)}$  are given as inputs to the system. Each pattern  $\xi^i$  corresponds to an “input coupler” strength set which we show by  $\mathbf{a}^{(i)} \triangleq [a_1^{(i)} \dots a_l^{(i)}]^T$  where  $l$  shows the total number of links in the chain. The training algorithm's final product is a single set of “training coupler” strengths,  $\mathbf{b} \triangleq [b_1 \dots b_l]^T$ , that will be stored in a library and later used in performing “accept/reject” tests as discussed before.

Let us start by defining a function:

$$\varphi = F(\mathbf{a}, \mathbf{b})$$

where  $\varphi$  is the output phase shift of the network when the “input” and “training” coupling strengths are set by vectors  $\mathbf{a}$  and  $\mathbf{b}$  respectively. In fact, we previously showed that this function is given by:

$$F(\mathbf{a}, \mathbf{b}) = \sum_{k=1}^l \text{Arg}(a_k + b_k e^{i2\pi/3})$$

If we fix  $\mathbf{b}$ , then the system's output for each pattern,  $\xi^{(i)}$ , is given by:

$$\varphi_i = F(\mathbf{a}^{(i)}, \mathbf{b})$$

We can thus define a cost function for the above particular choice of  $\mathbf{b}$  as:

$$C(\mathbf{b}) = \frac{1}{m} \sqrt{\sum_{i=1}^m (\Delta\varphi_i)^2}$$

where the  $i^{th}$  error term is defined as:

$$\Delta\varphi_i \triangleq \varphi_i - \varphi_0$$

What our training algorithm does is to simply calculate this cost function and minimize it to find an optimal choice of  $\mathbf{b}$ . The syntax for the MATLAB function that finds the training template is:

$$\mathbf{b} = \text{Train}(\mathbf{A}, \varphi_0)$$

where  $\mathbf{A}$  is the matrix of to-be-stored patterns whose  $i^{th}$  column is the  $i^{th}$  pattern we want the network to recognize, i.e,  $\mathbf{A}(:, \mathbf{i}) \triangleq \mathbf{a}^{(i)}$  and  $\varphi_0$  is the target angle for training.

The success of the “training phase” in finding a suitable  $\mathbf{b}$ , can be evaluated by calculating  $\varphi_1 \dots \varphi_m$  to see if they all fall into some desired neighborhood of  $\varphi_0$ , that is whether or not:

$$|\varphi_i - \varphi_0| \leq \delta\varphi \quad \forall i \in \{1 \dots m\}$$

Finally, the syntax for the MATLAB code for quantifying the storage capacity limits of the proposed circuit is:

$$S = \text{Capacity}(\mathbf{x}, N)$$

where  $N$  shows the total number of links in the coupled oscillator chain,  $S$  is a MATLAB data structure that stores the experiments results and  $\mathbf{x}$  is a vector whose elements specify the normalized number of patterns used in various storage capacity tests. In other words, for the  $i^{th}$  storage capacity experiment,  $m = \mathbf{x}(i) \cdot N$ , where  $m$  is the total number of random binary patterns,  $\xi^{(1)} \dots \xi^{(m)}$ , for which the network is trained.

## 6.6.4 The MATLAB codes

```
1 function S=Capacity(x,n)
2 % gives the chance of successful training for different
   training sample
3 % sizes specified in x
4 % n is the size of the network
5 % S is a MATLAB data structure with two fields
6 % S.x is a vector whose elements show the ratio of number
   of patterns in
7 % the training set to the network size ,i.e, S.x(i)=m(i)/n.
   where m(i) is the
8 % number of patterns in the training set. Therefore larger
   values of S.x
9 % correspond to higher storage capacities.
10 % S.y is a vector the same size as S.x which gives the
   chance of successful
11 % training for each network capacity specified by
12 global N Theta DelTheta Nb lb ub
13 % N is the total number of experiments
14 % Theta is the target angle
15 % IMPORTANT! Theta range is from -pi to 0 and 0 to pi ! The
   values of 0 and
16 % +/- pi should be avoided !
17 % DelTheta is the maximum error tolerance from Theta that
   is allowed in a
18 % successful training
```

```
19 % Nb is the resolution of the training (Bits
20 % lb is the lower bound for the b parameters
21 % ub is the upper bound for the b parameters
22 %
```

---

```
23 % Default values of the global variables :
24 N=1000;
25 Theta=pi/4;
26 DelTheta=pi/8;
27 Nb=10;
28 lb=0.1;
29 ub=1;
30 %
```

---

```
31 Nx=length(x);
32 y=zeros(Nx,1);
33 for i=1:Nx
34     y(i)=Test(x(i),n);
35 end
36 S.x=x/n;
37 S.y=y;
38 end
39 %% Test Function
40 function y=Test(m,n)
```

```

41 % Gives the chance of the network of size n being
    successfully trained for m random patterns.
42 global N Theta
43 % N is the total number of experiments performed
44 % y is the ratio of succesfull trainings
45 % Theta is the target angle fot the training
46 S=zeros(N,1);
47 for i=1:N
48 A=rand(n,m);
49 A=round(A);
50 b=Train(A,Theta);
51 S(i)=Evaluate(b,A);
52 end
53 y=sum(S)/N;
54 end
55 %% Train Function
56 function b=Train(A,Theta)
57 % Finds the best training template b for the patterns in A
58 % Theta is the target angle
59 global Nb lb ub
60 % Nb is the number of bits allowed for the training
    resolution
61 % lb is the lower bound for the b parameters
62 % ub is the upper bound for the b parameters
63 [n,~]=size(A);
64 x0=0.5*ones(n,1);

```

```

65 LB=lb*ones(n,1);
66 UB=ub*ones(n,1);
67 options=optimoptions('fmincon','MaxFunEvals',4e4,'Display',
    'iter');
68 x=fmincon(@(x) TargetFun(x,A,Theta),x0,[],[],[],[],LB,UB
   ,[],[],options);
69 xr=linspace(lb,ub,2^(Nb));
70 b=interp1(xr,xr,x,'Nearest');
71 end
72 %% Target Function
73 function y=TargetFun(x,A,Theta)
74 [n,m]=size(A);
75 z=exp(1i*Theta);
76 V=zeros(m,2);
77 V(:,1)=real(z);
78 V(:,2)=imag(z);
79 clear z
80 y=zeros(m,1);
81 for i=1:m
82     y(i)=PhaseShift(x,A(:,i));
83 end
84 y=exp(1i.*y);
85 U=[real(y) imag(y)];
86 z=dot(U,V,2);
87 z=acos(z);
88 y=norm(z)/(m);

```

```

89 end
90 %% PhaseShift Function
91 function y=PhaseShift(x,a)
92 % calculates the phase shift as given by the formula in the
    paper .
93 % Here x is the same as b if we want to use the paper's
    notation!
94 % The function determines the output phase shift when the "
    b" parameters
95 % are given by x and the "a" parameters are given by a
96 [n,~]=size(x);
97 t=zeros(n,1);
98 for i=1:n
99     z=a(i)+x(i)*exp(1i*2*pi/3);
100    t(i)=angle(z);
101 end
102 y=sum(t);
103 y=exp(1i*y);
104 y=angle(y);
105 end
106 %% Evaluate Function
107 function y=Evaluate(b,A)
108 % Determines if the training template b is succesful for
    all the patterns
109 % in A
110 % The training is succesful only if the output phase shift

```

```

    for all the
111 % patterns in A, falls into DelTheta proximity of the
        traget angle Theta
112 global Theta DelTheta
113 y=0;
114 [~,m]=size(A);
115 S=zeros(m,1);
116 for i=1:m
117     a=A(:,i);
118     Phi=PhaseShift(b,a);
119     if abs(Phi-Theta)<= DelTheta
120         S(i)=1;
121     end
122 end
123 if sum(S)==m
124     y=1;
125 end
126 end

```

## BIBLIOGRAPHY

- [1] A. Rofougaran, J. Rael, M. Rofougaran, and A. Abidi. A 900 MHz CMOS LC oscillator with quadrature outputs. In *1996 IEEE International Solid-State Circuits Conference. Digest of Technical Papers, ISSCC*, pages 392–393, Feb 1996.
- [2] Heng-Chia Chang, Xudong Cao, U. K. Mishra, and R. A. York. Phase noise in coupled oscillators: theory and experiment. *IEEE Transactions on Microwave Theory and Techniques*, 45(5):604–615, May 1997.
- [3] R. A. York and R. C. Compton. Quasi-optical power combining using mutually synchronized oscillator arrays. *IEEE Transactions on Microwave Theory and Techniques*, 39(6):1000–1009, Jun 1991.
- [4] Y. M. Tousi, O. Momeni, and E. Afshari. A novel CMOS high-power terahertz VCO based on coupled oscillators: Theory and implementation. *IEEE Journal of Solid-State Circuits*, 47(12):3032–3042, Dec 2012.
- [5] Yahya M. Tousi, Vahnood Pourahmad, and Ehsan Afshari. Delay coupled oscillators for frequency tuning of solid-state terahertz sources. *Phys. Rev. Lett.*, 108:234101, Jun 2012.
- [6] Y. Tousi and E. Afshari. A high-power and scalable 2-D phased array for terahertz CMOS integrated systems. *IEEE Journal of Solid-State Circuits*, 50(2):597–609, Feb 2015.
- [7] T. S. Rappaport, S. Sun, R. Mayzus, H. Zhao, Y. Azar, K. Wang, G. N. Wong, J. K. Schulz, M. Samimi, and F. Gutierrez. Millimeter wave mobile communications for 5g cellular: It will work! *IEEE Access*, 1:335–349, 2013.
- [8] W. Roh, J. Y. Seol, J. Park, B. Lee, J. Lee, Y. Kim, J. Cho, K. Cheun, and F. Aryanfar. Millimeter-wave beamforming as an enabling technology for 5g cellular communications: theoretical feasibility and prototype results. *IEEE Communications Magazine*, 52(2):106–113, February 2014.
- [9] Shajahan Kutty and Debarati Sen. Beamforming for millimeter wave communications: An inclusive survey. *IEEE Communications Surveys & Tutorials*, 18(2):949–973, 2016.
- [10] D. Ehyaie. *Novel approaches to the design of phased array antennas*. PhD thesis, University of Michigan, 2011.

- [11] R. A. York and T. Itoh. Injection and phase-locking techniques for beam control. *IEEE Transactions on Microwave Theory and Techniques*, 46(11):1920–1929, Nov 1998.
- [12] R. Adler. A study of locking phenomena in oscillators. *Proceedings of the IRE*, 34(6):351–357, June 1946.
- [13] B. Razavi. A study of injection locking and pulling in oscillators. *IEEE Journal of Solid-State Circuits*, 39(9):1415–1424, Sept 2004.
- [14] Charles M Gray. Synchronous oscillations in neuronal systems: mechanisms and functions. *Journal of computational neuroscience*, 1(1-2):11–38, 1994.
- [15] Alfons Schnitzler and Joachim Gross. Normal and pathological oscillatory communication in the brain. *Nature reviews neuroscience*, 6(4):285, 2005.
- [16] Pascal Fries. A mechanism for cognitive dynamics: neuronal communication through neuronal coherence. *Trends in cognitive sciences*, 9(10):474–480, 2005.
- [17] Juergen Fell and Nikolai Axmacher. The role of phase synchronization in memory processes. *Nature reviews neuroscience*, 12(2):105, 2011.
- [18] Frank Hoppensteadt and Eugene Izhikevich. Oscillatory Neurocomputers with Dynamic Connectivity. *Physical Review Letters*, 82(14):2983–2986, 1999.
- [19] Frank C Hoppensteadt and Eugene M Izhikevich. Pattern recognition via synchronization in phase-locked loop neural networks. *IEEE Transactions on Neural Networks*, 11(3):734–738, 2000.
- [20] Robert W Hölzel and Katharina Krischer. Pattern recognition with simple oscillating circuits. *New Journal of Physics*, 13(7):073031, 2011.
- [21] Thomas C Jackson, Abhishek A Sharma, James A Bain, Jeffrey A Weldon, and Lawrence Pileggi. Oscillatory neural networks based on tmo nano-oscillators and multi-level rram cells. *IEEE journal on Emerging and Selected Topics in Circuits and Systems*, 5(2):230–241, 2015.
- [22] Steven P Levitan, Yan Fang, Denver H Dash, Tadashi Shibata, Dmitri E Nikonov, and George I Bourianoff. Non-boolean associative architectures based on nano-oscillators. In *Cellular Nanoscale Networks and Their Applications (CNNA), 2012 13th International Workshop on*, pages 1–6. IEEE, 2012.

- [23] D. E. Nikonov, G. Csaba, W. Porod, T. Shibata, D. Voils, D. Hammerstrom, I. A. Young, and G. I. Bourianoff. Coupled-oscillator associative memory array operation for pattern recognition. *IEEE Journal on Exploratory Solid-State Computational Devices and Circuits*, 1:85–93, Dec 2015.
- [24] V. Pourahmad, S. Manipatruni, D. Nikonov, I. Young, and E. Afshari. Non-boolean pattern recognition using chains of coupled cmos oscillators as discriminant circuits. *IEEE Journal on Exploratory Solid-State Computational Devices and Circuits*, 3:1–9, Dec 2017.
- [25] John J Hopfield. Neural networks and physical systems with emergent collective computational abilities. *Proceedings of the national academy of sciences*, 79(8):2554–2558, 1982.
- [26] Yoshiki Kuramoto. *Chemical oscillations, waves, and turbulence*, volume 19. Springer Science & Business Media, 2012.
- [27] A. Mirzaei, M. E. Heidari, and A. A. Abidi. Analysis of oscillators locked by large injection signals: Generalized Adler’s equation and geometrical interpretation. In *IEEE Custom Integrated Circuits Conference 2006*, pages 737–740, Sept 2006.
- [28] E.M. Izhikevich. *Dynamical Systems in Neuroscience*. Computational neuroscience Dynamical systems in neuroscience.
- [29] G Bard Ermentrout and David H Terman. *Mathematical foundations of neuroscience*, volume 35. Springer Science & Business Media, 2010.
- [30] Ali Hajimiri and Thomas H Lee. A general theory of phase noise in electrical oscillators. *IEEE journal of solid-state circuits*, 33(2):179–194, 1998.
- [31] J. Guckenheimer and P. Holmes. *Nonlinear Oscillations, Dynamical Systems, and Bifurcations of Vector Fields*. Applied Mathematical Sciences. Springer New York, 2013.
- [32] F. Verhulst. *Nonlinear Differential Equations and Dynamical Systems*. Universitext. Springer Berlin Heidelberg, 2012.
- [33] A. Mirzaei, M. E. Heidari, R. Bagheri, S. Chehrazi, and A. A. Abidi. The quadrature LC oscillator: A complete portrait based on injection locking. *IEEE Journal of Solid-State Circuits*, 42(9):1916–1932, Sept 2007.

- [34] Johan Van Der Tang, Pepijn Van De Ven, Dieter Kasperkovitz, and Arthur Van Roermund. Analysis and design of an optimally coupled 5-ghz quadrature lc oscillator. *IEEE Journal of Solid-State Circuits*, 37(5):657–661, 2002.
- [35] J A Rogge and D Aeyels. Stability of phase locking in a ring of unidirectionally coupled oscillators. *Journal of Physics A: Mathematical and General*, 37(46):11135, 2004.
- [36] J. F. Buckwalter, A. Babakhani, A. Komijani, and A. Hajimiri. An integrated subharmonic coupled-oscillator scheme for a 60-GHz phased-array transmitter. *IEEE Transactions on Microwave Theory and Techniques*, 54(12):4271–4280, Dec 2006.
- [37] A. Valdes-Garcia, S. T. Nicolson, J. W. Lai, A. Natarajan, P. Y. Chen, S. K. Reynolds, J. H. C. Zhan, D. G. Kam, D. Liu, and B. Floyd. A fully integrated 16-element phased-array transmitter in sige bicmos for 60-GHz communications. *IEEE Journal of Solid-State Circuits*, 45(12):2757–2773, Dec 2010.
- [38] W. Shin, B. H. Ku, O. Inac, Y. C. Ou, and G. M. Rebeiz. A 108-114 GHz 4x4 wafer-scale phased array transmitter with high-efficiency on-chip antennas. *IEEE Journal of Solid-State Circuits*, 48(9):2041–2055, Sept 2013.
- [39] G. Li and E. Afshari. A low-phase-noise multi-phase oscillator based on left-handed lc-ring. *IEEE Journal of Solid-State Circuits*, 45(9):1822–1833, Sept 2010.
- [40] G. Li and E. Afshari. A low-phase-noise wide-tuning-range quadrature oscillator in 65nm CMOS. In *Proceedings of the IEEE 2012 Custom Integrated Circuits Conference*, pages 1–4, Sept 2012.
- [41] O. Momeni and E. Afshari. High power terahertz and millimeter-wave oscillator design: A systematic approach. *IEEE Journal of Solid-State Circuits*, 46(3):583–597, March 2011.
- [42] R. Han and E. Afshari. A CMOS high-power broadband 260-GHz radiator array for spectroscopy. *IEEE Journal of Solid-State Circuits*, 48(12):3090–3104, Dec 2013.
- [43] A. Mazzanti, E. Sacchi, P. Andreani, and F. Svelto. Analysis and design of a double-quadrature CMOS VCO for subharmonic mixing at Ka-band. *IEEE Transactions on Microwave Theory and Techniques*, 56(2):355–363, Feb 2008.

- [44] A. Nikoofard, S. Kananian, and A. Fotowat-Ahmady. Off-resonance oscillation, phase retention, and orthogonality modeling in quadrature oscillators. *IEEE Transactions on Circuits and Systems I: Regular Papers*, 63(6):883–894, June 2016.
- [45] A. Guha Roy, S. Dey, J. B. Goins, T. S. Fiez, and K. Mayaram. 350 mV, 5 GHz class-D enhanced swing differential and quadrature VCOs in 65 nm CMOS. *IEEE Journal of Solid-State Circuits*, 50(8):1833–1847, Aug 2015.
- [46] B. Jiang and H. C. Luong. A 7.9-GHz transformer-feedback quadrature oscillator with a noise-shifting coupling network. *IEEE Journal of Solid-State Circuits*, 52(10):2636–2646, Oct 2017.
- [47] P. Maffezzoni, B. Bahr, Z. Zhang, and L. Daniel. Oscillator array models for associative memory and pattern recognition. *IEEE Transactions on Circuits and Systems I: Regular Papers*, 62(6):1591–1598, June 2015.
- [48] Yan Fang, Chet N Gnegy, Tadashi Shibata, Denver Dash, Donald M Chiarulli, and Steven P Levitan. Non-boolean associative processing: Circuits, system architecture, and algorithms. *IEEE Journal on Exploratory Solid-State Computational Devices and Circuits*, 1:94–102, 2015.
- [49] Tadashi Shibata, Renyuan Zhang, Steven P Levitan, Dmitri E Nikonov, and George I Bourianoff. CMOS supporting circuitries for nano-oscillator-based associative memories. In *Cellular Nanoscale Networks and Their Applications (CNNA), 2012 13th International Workshop on*, pages 1–5. IEEE, 2012.
- [50] Matthew J Cotter, Yan Fang, Steven P Levitan, Donald M Chiarulli, and Vijaykrishnan Narayanan. Computational architectures based on coupled oscillators. In *VLSI (ISVLSI), 2014 IEEE Computer Society Annual Symposium on*, pages 130–135. IEEE, 2014.
- [51] Steven H Strogatz. *Nonlinear dynamics and chaos: with applications to physics, biology, chemistry, and engineering*. CRC Press, 2018.
- [52] Teuvo Kohonen. *Self-organization and associative memory*, volume 8. Springer Science & Business Media, 2012.
- [53] Raúl Rojas. *Neural networks: a systematic introduction*. Springer Science & Business Media, 2013.

- [54] John A Hertz. *Introduction to the theory of neural computation*. CRC Press, 2018.
- [55] Toshio Aoyagi. Network of neural oscillators for retrieving phase information. *Physical review letters*, 74(20):4075, 1995.
- [56] Jonathan S Golan. *The linear algebra a beginning graduate student ought to know*. Springer Science & Business Media, 2012.
- [57] Paolo Maffezzoni, Bichoy Bahr, Zheng Zhang, and Luca Daniel. Analysis and design of boolean associative memories made of resonant oscillator arrays. *IEEE Transactions on Circuits and Systems I: Regular Papers*, 63(11):1964–1973, 2016.
- [58] Chris Bishop, Christopher M Bishop, et al. *Neural networks for pattern recognition*. Oxford university press, 1995.
- [59] M Bishop Christopher. *Pattern recognition and machine learning*. Springer-Verlag New York, 2016.
- [60] Behzad Razavi and Razavi Behzad. *RF microelectronics*, volume 2. Prentice Hall New Jersey, 1998.
- [61] Thomas H Lee. *The design of CMOS radio-frequency integrated circuits*. Cambridge university press, 2003.